UNIVERSITY OF CALIFORNIA
SANTA CRUZ

Lessons in Earthquake Physics from the 2011 Prague, Oklahoma Earthquake Sequence

A dissertation submitted in partial satisfaction
of the requirements for the degree of

DOCTOR OF PHILOSOPHY

in

EARTH SCIENCES

by

Kristina Kame Okamoto

December 2023

The Dissertation of Kristina K. Okamoto is approved:

_____
Professor Heather M. Savage, Chair

_____
Professor Emily E. Brodsky

_____
Research Scientist Nicholas Beeler

_____
Peter Biehl
Vice Provost and Dean of Graduate Studies

Table of Contents

List of Figures

Abstract

Lessons in Earthquake Physics from the 2011 Prague, Oklahoma Earthquake Sequence

Kristina Kame Okamoto

Pore fluid pressure lowers effective normal stress and weakens granular material (Terzaghi, 1936). Because of the "effective stress law", fault failure can be induced through injection of fluids, as seen at the Rocky Mountain arsenal in the 1960s (Healy et al., 1968). A more definitive field test in Rangely, Colorado, demonstrated that when fluid pressures were raised and lowered in an oil reservoir over 4 years, seismicity rates were raised and lowered as well. Earthquakes occurred when fluid pressure in the reservoir was above ~25 MPa and the study postulated that one day, scientists might be able to control earthquakes along the San Andreas fault (Raleigh et al., 1976). During the 2010s, induced seismicity in Oklahoma rose precipitously due to massive wastewater injection activities. This wastewater is a byproduct of hydraulic fracturing of tight shale reservoirs, which is also known as super fracking (Turcotte et al., 2014). From 2014-2017, Oklahoma had more M3+ earthquakes than California, a state that is both tectonically active and is 2.3 times larger than Oklahoma. The largest mainshock events in Oklahoma history include the 2011 M5.7 Prague, the 2015 M5.1 Fairview, and the 2016 M5.8 Pawnee earthquakes. The Prague sequence also includes an M5 foreshock and M5 aftershock, which are large by induced seismicity standards.

While super fracking poses a hazard to humans by polluting drinking water and creating seismicity, it has allowed earthquake scientists to ask and answer fundamental questions about earthquakes. Instead of having to constrain the causes of natural phenomena, the cause of these events is anthropogenic. The following are a few key questions in earthquake physics that can be addressed through induced seismicity studies: 1) Is there a critical pore fluid pressure for fault failure? 2) When a fault fails, what controls the mode of failure, or in other words, why does it fail in a slow (creep) or fast (earthquakes) event? 3) Are measurements of frictional strength in small-scale laboratory experiments relevant to the seismic scale, and if so, how can we use them to understand seismicity? The 2011 Prague, Oklahoma earthquakes are an extremely well-recorded sequence within well-known stratigraphy that allows us to address these questions. Earthquakes within this sequence occur in the Arbuckle group, a permeable carbonate unit where most wastewater is injected, and within the basement granitic rock. These geological units will be important in all three chapters. In addition, this earthquake sequence involved three faults, the M_w5 foreshock fault, the $M_w5.7$ mainshock fault, and the M_w5 aftershock fault that allows me to probe the role of fault geometry on seismicity.

In Chapter 1, I use repeating earthquakes to ask what controls the mode of failure during an aftershock sequence? Repeating earthquakes, i.e. earthquakes that re-rupture the same area over and over again, are proxies for aseismic slip. A group of repeating earthquakes that ruptures the same fault is termed a family of repeating earthquakes. I find that families of repeating earthquakes occur in the Arbuckle

Group and the basement granite, and form four main clusters. Three of these clusters occur at fault intersections. Here, I explore reasons why fault intersections might preferentially host aseismic slip. The traditional model of afterslip (slow slip that occurs along a fault after an earthquake) is that it occurs in velocity-strengthening areas that cannot fail seismically due to stress from an adjacent earthquake. Using this model to explain our findings would require extreme heterogeneity of the material properties of nearby slipping patches, and it does not allow for overlapping aseismic and seismic slip patches like we see here. Alternatively, extreme stress heterogeneity at these fault intersections may allow for afterslip in typically unstable areas, which is possible in a non-steady-state rate-state framework. This stress heterogeneity could also allow for earthquakes in typically stable areas when taking into account dynamic weakening. This chapter demonstrates that areas of stress heterogeneity can promote a variety of slip behaviors and that slow slip at fault intersections can promote failure on non-critically stressed faults, such as the fault that hosted the M_w5 aftershock.

In Chapter 2, I measure the frictional properties of Oklahoma lithologies at various pore fluid pressures in order to determine lithological and pore pressure controls on Oklahoma induced seismicity. I perform slide-hold-slide tests to determine the frictional restrengthening behavior and velocity steps to determine the stability of the material at different pore fluid pressures. I find that the frictional healing rate of the Arbuckle dolomite is dependent on pore fluid pressure. At the highest pore fluid pressure measured, the Arbuckle dolomite weakens with hold time. I interpret such weakening to be the result of carbonate dissolution at grain contacts

within the gouge layer. These experiments were run with pore fluid water undersaturated with respect to carbonate ions and therefore, during a hold, the asperities have enough time at high pressure to either dissolve and shrink a contact or, even if the contacts grow during the hold, the chemistry of the interstitial fluid could weaken the bonds at the contacts increasingly over time. Why dissolution is more effective at high pore fluid pressures than at lower pore fluid pressures is not resolvable from the suite of experiments run here, but I have a few hypotheses. First, more localized shear zones that occur in the high effective stress experiment have less pore space and therefore less available unsaturated water near contacts, and so dissolution is not as ubiquitous. Second, at increased contact pressure, the thickness of the interstitial layer is smaller. Finally, the strain rate at lower effective stresses is slower during the hold and therefore allows for more weakening below a critical rate for dissolution. Further work will be needed to determine which, if any, of these conditions might be responsible for frictional weakening. I find that the healing rate of the basement granitic rock is not dependent on pore fluid pressure, however I note that at the highest pore fluid pressure analyzed, stress relaxation uniquely does not follow the same stress-displacement relationship that all other experiments exhibit. In addition, I find that pore fluid pressure in both lithologies stabilizes the gouge for sliding velocities between 1-10 μm/s. Implications of this work are that pore fluid pressure promotes stable failure, and that carbonates can frictionally weaken when injected with pore fluid that is unsaturated in carbonate ions. This may drive slow slip in carbonate regions and stress faults in regions capable of nucleating earthquakes.

This helps to illuminate why injection into carbonates in places such as Oklahoma, Canada, and Texas allows for widespread seismicity, while areas such as North Dakota, where high volume injection occurs into permeable sandstone, has far less seismicity.

In Chapter 3, I use repeating earthquakes in order to probe whether laboratory-measured frictional behavior can be scaled to the seismic cycle. Laboratory studies predict three stages of fault healing: rapid post-seismic healing, a delay in healing due to afterslip, and a gradual increase in healing. In chapter 2, I measured stage 3 healing, i.e. the gradual increase in healing with log (time). Using the repeating earthquakes from chapter 1, and focusing only on families with greater than 3 events, I analyze their moment-recurrence time behavior. Moment is dependent on both the amount of slip and the spatial area of the earthquake. Ideally, I would first analyze their stress drop, however these are small earthquakes whose waveforms are likely attenuated. I find that there are three types of moment-recurrence time behavior in the Prague sequence that correspond to the three spatially distinct regions hosting repeaters that I saw in Chapter 1. The first group shows constant moment regardless of recurrence time and occurs at the mainshock-foreshock fault intersection in the Arbuckle unit. The second group is moment-predictable with recurrence time and occurs in the basement granite off of the mainshock-foreshock fault intersection. The third group has scattered moment-recurrence time behavior and occurs at the mainshock-foreshock fault intersection in the basement granitic unit. I interpret the constant moment group in the Arbuckle unit

as evidence of a lack of healing that is caused by dissolution effects within the fault as seen in my experiments in Chapter 2. For repeating earthquakes to occur, rapid healing must have occurred following each repeating earthquake, prior to the onset of dissolution-induced weakening. I show that the moment-predictable group is consistent with laboratory rates if attenuation is assumed to be masking the event's true source duration. Finally, I interpret the scattered moment group as indicative of either chaotic loading conditions by the surrounding aseismic slip area or chaotic pore fluid pressure conditions. Unlike previous studies of repeating earthquakes, I show that healing behavior may vary depending on lithology and pressure conditions, and that lithology-dependent laboratory healing behaviors are relevant even at seismic scales.

In total, this dissertation has answered a number of questions in earthquake physics. 1) Is there a critical pore fluid pressure for fault failure? We find that fault failure thresholds can be weakened by time-dependent chemical reactions, which could allow for failure on faults at a much lower pore fluid pressure than otherwise. In other words, the effective stress law may not be the controlling factor for carbonate faults. 2) When a fault fails, what controls the mode of failure, or in other words, why does it fail in a slow (creep) or fast (earthquakes) event? We find that the dominant cause of aseismic slip during the Prague sequence is stress heterogeneity. Our laboratory analysis suggests that aseismic slip should occur at high pore fluid pressures in the Arbuckle and in the granite. 3) Are measurements of frictional strength in small-scale laboratory experiments relevant to the seismic scale, and if so,

how can we use them to understand seismicity? We find that laboratory healing rates are consistent with moment-recurrence time behavior of repeating earthquakes in Chapter 3, therefore it might be possible to directly scale slide-hold-slide tests from the laboratory to the seismic scale. However, to do so, one must also consider rapid post-seismic healing and a delay in healing during afterslip. Furthermore, I show that more work is needed to include the role of fluid chemistry in our understanding of fault healing. These are some of the findings and implications for this work and more are outlined in the following chapters.

Acknowledgements

The text of this dissertation includes a reprint of the following previously published material. The co-authors listed in this publication directed and supervised the research which forms the basis for the dissertation.

Chapter 1: Okamoto, K. K., Savage, H. M., Cochran, E. S., & Keranen, K. M. (2022). Stress heterogeneity as a driver of aseismic slip during the 2011 Prague, Oklahoma aftershock sequence. Journal of Geophysical Research: Solid Earth, 127, e2022JB024431. https://doi.org/10.1029/2022JB024431

It has been a privilege to spend five years studying earthquakes with a crew of fantastic people. I also feel incredibly privileged to have a wonderful advisor, Heather Savage. She has always believed in me and given me a balance between guidance and freedom that, in my opinion, is rarely achieved in advising. In addition, I thank Heather for all her thoughtful and thorough corrections and comments on everything I have written during this PhD. To my committee member and mentor, Emily Brodsky, thank you for inspiring me to study earthquakes, for your never-ending appetite for science, and for always taking the time to walk through my problems. To my committee member, Nick Beeler, thank you for somehow finding the kindest way to point out issues in my work and then gently pointing me in a better direction. In addition, I am endlessly grateful for the rapid deployment of seismometers by Kade Keranen to capture the Prague sequence. Without that, this thesis would not exist. I thank all my collaborators on these chapters, including Elizabeth Cochran, Rachel Abercrombie, and Brett Carpenter for their helpful conversations over the years.

I started this PhD at the Lamont-Doherty Earth Observatory and have plenty of people to thank from my year spent there. I am beyond grateful for the patient help of Ted Koczynski while I learned how to run high pressure experiments. I thank Hannah Rabinowitz and Caroline Seyler for teaching me how to prepare friction experiments. To Genevieve Coffey, thank you for your support in my first year of graduate school in navigating science and Lamont, and for your friendship ever since. Thank you to Ben Holtzman, Rob Skarbek, Christine McCarthy, and Seth Saltiel for all the help during that year and beyond. I am grateful for my time with my colleagues and cohort at Lamont, especially Theresa Sawi, Anna Barth, Lucy Tweed, Bar Oryan, Janine Burnham, and Lauren Moseley.

When Heather got a job at Santa Cruz, I was sad to move away from the great people at Lamont, but also elated to come back to the excellent department at UCSC. There are too many people to thank here. Thank you to Matthew Clapham for being my undergraduate scientific advisor and for patiently teaching me the ins and outs of coding, databasing, presenting research, and paleontological work. Thank you to Susan Schwartz and Thorne Lay for sharing their knowledge over many seismocoffees and lunches. My sincerest gratitude to my office mate, Travis Alongi, for listening to me rant about my science and for your friendship over these many years together. I thank Julia Krogh, Jackie Williams, Ross Nelson, Tessa Nefouse, and Otis Wickenhauser for your help in building a creative and fun rock mechanics lab; you have made this PhD possible. Thank you to all the members of the seismology lab for their help over the years including Stephanie Taylor, Luca

Malatesta, Grace Barchek, Shalev Siman-Tov, Heather Crume, Ricky Garza-Giron, Kelian Dascher-Cousineau, Alba Rodriguez-Padilla, Em Schnorr, Huiyun Guo, Litong Huang, Gaspard Farge, Valère Lambert, Doron Morad, Will Steinhardt, Mia Trodden, Jaiden Zak, and Chris Thom. Thank you to Dan Sampson and Brandon Cheney for technical help fixing broken parts and assistance in building the lab. A special second thank you to Brandon Cheney for help with the SEM for work in Chapter 2. Thank you to the administrative support from Jennifer Fish, Amy Kornberg, Lisa Stipanovich, and Sabrina Dalbesio that made this PhD possible.

I also thank the University of Minnesota group, especially Lars Hansen, Amy Ryan, and Amanda Dillman, for welcoming me into their lab. The lessons I learned during the two weeks I spent there in 2022 have greatly influenced this work. I am very excited to spend the next few years at UMN.

Finally, I thank my friends and family for all their support. I would like to especially thank my friends that kept me sane in the pandemic and beyond including Cleo, Ally, Aurora, Adam, and Levi. Thank you to all those that raised me, and I am forever grateful for constant support from my brother, Thomas, and my sister, Alisa.

Chapter 1 - Stress heterogeneity as a driver of aseismic slip during the 2011 Prague, Oklahoma aftershock sequence

Abstract

The interaction of aseismic and seismic slip before and after an earthquake is fundamental for both earthquake nucleation and postseismic stress relaxation. However, it can be difficult to determine where and when aseismic slip occurs within the seismogenic zone because geodetic techniques are limited to detecting moderate to large slip amplitudes or long duration small slip amplitudes. Here, we use repeating earthquakes (earthquakes that re-rupture the same fault patch) as a proxy for aseismic slip during the 2011 Prague, Oklahoma earthquake sequence. We find that aseismic slip in the Prague earthquake sequence occurs both within the granitic basement and the overlying sedimentary rocks. The repeating earthquakes show that patches of aseismic slip are mostly located at fault intersections. These fault intersections hosted possible mainshock slip, abundant aftershocks, and afterslip. We estimate that ~40% of the aftershocks are driven by afterslip. We interpret that aseismic slip occurs at fault intersections where stress heterogeneity creates patches of lower stress that are stable within a non-steady-state, rate-state framework.

Plain Language Summary

Faults can move at various speeds ranging from slower than tectonic plate rate to the speed of an earthquake. After an earthquake, parts of the fault can move slowly as a response to the earthquake slip. This slow movement is called afterslip. It is

important to know the location of afterslip in order to determine the hazard of the area as well as for understanding fault physics in general. Mapping where afterslip occurs is difficult because GPS data have limited resolution. Here, we map the afterslip from the M_w 5.7 2011 Prague, Oklahoma earthquake using repeating earthquakes as a proxy. These repeating earthquakes are thought to be driven by slow slip surrounding an area prone to small earthquake ruptures (a bump in the rock or a patch of different rock). We find that afterslip generally occurs at the intersections of three faults. These intersections host a range of slip behavior including a high number of aftershocks, possibly mainshock slip, and afterslip. The geometry of these fault intersections could cause a highly heterogeneous postseismic stress field. We find that this heterogeneous stress field can explain the range of fault slip behavior seen at these locations.

1. **Introduction**

Faults can fail over a range of velocities and durations from plate-rate creep to stick-slip events. Aseismic slip is any fault movement that does not occur at seismic slip speeds, while slow slip occurs at speeds greater than plate-rate and slower than earthquake slip. We are studying an induced sequence in an area far from tectonic boundaries, such that the resolved velocity across this fault pre-induced seismicity should be effectively zero. Therefore, we interchangeably use slow slip and aseismic slip. The importance of aseismic and slow slip is demonstrated by the variety of ways it can interact with earthquakes. Slow slip events can occur as precursory slip that accelerates into large earthquakes (Kato et al., 2016; 2012), independent events that

trigger large earthquakes (Uchida et al., 2016; Soquet et al., 2016), or transient slip events that occur unrelated to a large earthquake (Shaddox et al., 2021). Aseismic slip can also occur as afterslip and triggered transient slip following moderate and large earthquakes (Hirao et al., 2021; Schwartz & Rokosky, 2007). The occurrence of aseismic slip following an earthquake redistributes stress concentrations and changes the seismic hazard of the area. Therefore, pinpointing the location of aseismic slip is necessary for determining where this redistribution takes place to better constrain the processes that control seismic slip behavior.

Unraveling the role of aseismic slip in the accumulation and release of elastic strain can be difficult as there are limits to what slip amplitudes can be detected geodetically. Small to moderate sized slow slip events are typically spatially limited with small surface deformations, and thus must be inferred from other observations. Repeating earthquakes, also referred to as repeaters, are commonly used to infer the location of slow slip as they are thought to represent an asperity embedded in a creeping medium that fails repeatedly when driven by tectonic loading or transient stresses (Kato et al., 2012; Nadeau & Johnson, 1998). Repeating earthquakes have also been interpreted as evidence of fluid pressure changes alone or fluid flow that allows for aseismic slip (Baisch & Harjes, 2003; Shaddox & Schwartz, 2019). However, tectonic settings have complicated structure, lithology, and pore pressure that make it difficult to determine the mechanisms responsible for aseismic slip.

Here, we use repeating earthquakes during the 2011 Prague, Oklahoma earthquake sequence to determine the spatiotemporal interaction of slow slip and

seismic slip. The aftershock sequence is well documented by a catalog of 8,811 events (Cochran et al., 2020), which allows us to map where these repeating earthquakes are occurring in detail. In addition, the geology of Oklahoma in the area of interest is relatively uncomplicated compared to active plate boundaries and the depth extents of shallowly dipping sedimentary units are well constrained from oil and gas well logs (Figure 1D; Keranen et al., 2013). This presents us with a unique dataset to understand where aseismic slip occurs following a moderate size mainshock event. We find that aseismic slip in the Prague earthquake sequence occurs in two main areas: within the Arbuckle carbonate group at the shallow edge of the mainshock rupture and along intersections of the faults. We discuss various mechanisms that can explain the observations of mainshock rupture, regular aftershocks, and repeating aftershocks and inferred slow slip over small spatial scales and short time periods.

2. Background

2.1 Induced Seismicity in Oklahoma

During the 2010s, Oklahoma was the most active area of induced seismicity in the United States (Weingarten et al., 2015). Induced seismicity in Oklahoma is mostly caused by wastewater disposal, which increases pore pressure and reduces effective normal stress on faults (Ellsworth, 2013; Keranen et al., 2014; Walsh & Zoback, 2016; Weingarten et al., 2015). Induced seismicity can also be caused directly from hydraulic fracturing (Eyre et al., 2019). The 2011 Prague earthquake

sequence included a M_w 5.0, M_w 5.7, and another M_w 5.0 earthquake, respectively occurring on Nov. 5, 6, and 8 (Ekström et al., 2012). These events will hereafter be referred to as events A, B, and C as in previous papers (Keranen et al., 2013). Event B is the second largest earthquake recorded during Oklahoma's instrumented history, after the 2016 Pawnee Mw 5.8 earthquake. The three events occurred on three separate faults, referred to as faults A (M_w 5.0 foreshock fault), B (M_w 5.7 mainshock fault), and C (M_w 5.0 aftershock fault) corresponding to the event that occurred along it. Previous studies suggest that fault B was optimally orientated for failure within the pre-existing stress field, however faults A and C were not (Cochran et al., 2020) and that the Prague area was near critical failure, most likely due to high pore pressure, in the year before the earthquake sequences started (van der Elst et al., 2013). Previously, precursory aseismic slip as inferred from repeating earthquakes was detected before event C (Savage et al., 2017). Here, we expand the analysis of repeating earthquakes during the Prague sequence by searching for repeating earthquakes in Cochran et al. (2020)'s longer and more complete catalog.

2.2 Repeating Earthquakes as Aseismic Indicators

Repeating earthquakes are commonly separated into two distinct types: continual and burst type. Continual type repeaters occur where aseismic slip occurs over the recorded history of an area at an approximately constant rate, allowing elastic strain to accumulate until reaching the strength of the asperity, causing it to fail seismically. This would result in earthquakes of the same size re-rupturing the same

fault patch with similar recurrence intervals (Nadeau & Johnson, 1998; Uchida, 2019). Burst-type repeaters occur during transient episodes of aseismic slip (Igarashi et al., 2003). Because the rate of aseismic slip changes with time, the recurrence interval of these repeating earthquakes as well as their magnitudes can vary (Marone, 1998). Burst-type repeaters have been found during afterslip of moderate to large earthquakes (Chaves et al., 2020), as precursory slip leading up to earthquakes (Kato et al., 2012; Savage et al., 2017), and as evidence of fluid pressure changes (Baisch & Harjes, 2003; Cochran et al., 2018; Lengliné et al., 2014). Typical magnitudes range from 0.5-4 for burst type repeating earthquakes (Chen et al., 2008; Igarashi, 2003; Taira et al., 2014). The reliability of burst type repeating earthquakes as representing aseismic slip has been investigated by comparing geodetic measurements of slip rates to repeating earthquake timing and recurrence intervals, and have generally been found to be consistent (Beeler et al., 2001a; Shaddox et al., 2021). For afterslip, the occurrence of burst type repeaters should decay with time from the mainshock event due to the slip rate decelerating.

2.3 Rate-state friction and slip stability

Rate and state friction is an empirical model that describes the frictional response of materials to a change in velocity or stress that provides a framework for understanding where and under what conditions earthquakes, aseismic slip, and creep occur (Dieterich, 1979; Ruina, 1983). Following an increase in velocity, the rate term describes a sudden increase in friction and the state term describes the logarithmic

decay in friction to a new steady state. The state parameter within the rate-state equation is characterized by an evolution law. The two most commonly used evolution laws are the slip law, where friction evolves with slip, and the aging law, where friction evolves with time. For both the slip and the aging law, at steady-state these equations allow for the simplified description of behavior using rate-state parameters *a* and *b* as (*a*-*b*)<0 as unstable, (*a*-*b*)>0 as stable, and (*a*-*b*)~0 as conditionally stable. Within the unstable regime, fault patch stiffness (*k*) must be less than the critical stiffness ($k_c = \frac{\sigma(b-a)}{D_c}$) in order to experience instability (Ruina, 1983), where *s* is the normal stress and D_c is the critical slip distance.

Increasing pore-fluid pressure is expected to promote fault slip, but whether the slip occurs seismically or aseismically remains an issue. According to rate-state friction, increasing pore fluid pressure in conditionally stable materials decreases the effective normal stress, which decreases k_c and promotes aseismic failure (Scholz, 1998). Many studies find that induced seismicity is caused by loading of areas with subhydrostatic pressures by aseismic slip that is nucleated in areas that have higher fluid pressure (Bhattacharya & Viesca, 2019; Cappa et al., 2019; Guglielmi et al., 2015; Wei et al., 2015; Wynants-Morel et al., 2020). It is possible that seismic slip could be directly caused by the rate-state parameters (*a, b,* D_c) changing with increased fluid pressure (Scuderi & Colletini, 2016). If these changes counterbalance the change of effective normal stress, then pore fluid pressure increases could lead to seismic slip directly. The interactions between aseismic and seismic slip styles with pore fluid pressures are not unique to the process of induced seismicity. Pore fluid

pressure is commonly invoked as being a major control of natural earthquake occurrence (French & Morgan, 2020; Ross et al., 2020). Understanding the interplay of aseismic slip and seismic slip and what role fluids play will aid in understanding the mechanics of earthquakes within both induced and natural areas.

Figure 1: 1.1 Prague Seismicity and Stratigraphy

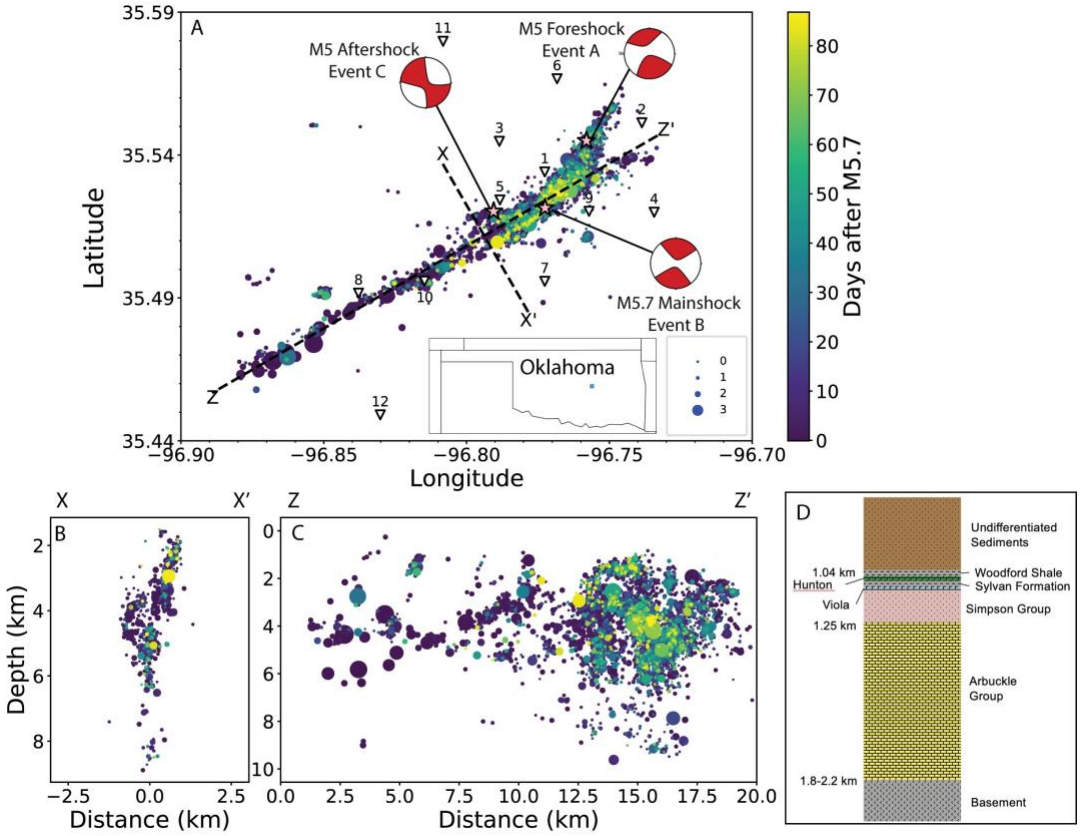

Figure 1: A-C) The full catalog of aftershock events in map, cross fault (X-X'), and along strike (Z-Z') views (Cochran et al., 2020). The focal mechanisms of events A, B, and C (the three largest events) whose respective magnitudes are 5.0, 5.7, and 5.0 are shown in map view (Ekström et al., 2012). All other events are color coded by time in days after the M5.7 earthquake and have marker sizes proportional to magnitude. Seismic stations are shown as inverted triangles and numbered according to station name. D) A stratigraphic section of the Prague area based on figure 2 in Keranen et al., 2013. The known depths to the top of the Hunton Limestone, Arbuckle

Group, and basement unit are on the left-hand side. Each layer is scaled appropriately for the given depth range.

3. Data and Methods

A temporary seismic network was deployed in the week following the Mw 5.0 earthquake on November 6, 2011 (Keranen et al., 2013). A total of 31 stations were installed, however in this study we limit our analysis to the 18 stations within ~10 km from fault A (station code: LC). Six of the 18 stations were operating by the time the Mw 5.7 event occurred and eight were operating by the second Mw 5.0 earthquake. Before the Mw 5.7 mainshock, the six stations in operation used a sample rate of 100 Hz. Following this mainshock, the stations were changed to sample at 250 Hz. All subsequent stations used a 250 Hz sampling rate. Further station information is available in Sumy et al. (2017) and the IRIS database (https://doi.org/10.7914/SN/ZQ_2011).

We analyze events from the Cochran et al. (2020) catalog, which used 900 hand-picked earthquakes from Sumy et al. (2017) as template events to find additional detections in the continuous waveform data. These events were relocated using GrowClust (Trugman & Shearer, 2017) resulting in median relative uncertainties of 112 m horizontally and 113 m vertically. The relocated catalog has a total of 8,811 events (Cochran et al., 2020). The catalog has magnitudes ranging from -1.36-3.81 when excluding the three largest events. We removed the events that are not located on the main fault strands in the following analysis.

In order to find repeating earthquakes in the sequence, we first use the cross-correlation coefficients computed during the template matching process and that were used as an input for the GrowClust algorithm. These cross-correlations were computed for filtered 2s windows around the P and S phases. The windows are typically too short to use for analyzing repeating earthquakes but are useful in order to limit the number of computationally expensive full waveform cross-correlations. We only analyzed earthquakes with a station-averaged > 0.8 cross-correlation coefficient for both P and S arrivals across all stations and where 80% of the stations had a cross correlation coefficient above 0.8. This ensured that a sufficient number of stations recorded the earthquakes. This reduced the number of events for the full waveform cross-correlations to 1,355.

We cross correlated these 1,355 waveforms in order to find repeating earthquakes. Event pairs are determined to be repeating earthquakes if they have an average cross correlation value of 0.95 on three or more stations. We used as many stations as were operable for a pair of earthquakes. These pairs are grouped into families of events using the python package networkx (Hagberg et al., 2008) (Figure 2). We applied a 1-25 Hz bandpass filter before cross correlation that eliminates longer period noise but conserves the frequencies of the seismic phases. Waveforms start 0.5 seconds before the P wave and have a duration of 2.5 times the difference between the S and P arrivals. Typical window lengths are 2-4 seconds. This window length is consistent with past studies of repeating earthquakes and includes the main phase arrivals plus early coda information (Baisch et al., 2008). The P and S arrivals

were estimated from the event origin time and a local velocity model (Keranen et al., 2013) using the taup module in obspy (Crotwell et al., 1999).

There is no universally accepted definition of repeating earthquakes, however two key parameters are often used to determine what qualifies as a repeating earthquake: the cross correlation cut off value and the applied filter (Uchida & Bürgmann, 2019; Uchida, 2019). Studies typically require waveforms to match with a cross-correlation value of 0.8-0.98 (Savage et al., 2017; Uchida & Bürgmann, 2019). While this threshold is important, it is not the only parameter affecting this definition, and cannot be used alone to determine whether a set of earthquakes are well correlated enough to be defined as repeaters. Typically, bandpass filters with a low frequency corner of 1 to 3 Hz and a high frequency corner of 4 to 30 Hz are applied to waveforms (see references in Uchida, 2019). A more limited bandpass will generally result in higher cross-correlation coefficients. Due to the small size of these events, we chose a bandpass of 1-25 Hz. A higher cutoff frequency (i.e. 25 Hz in our case) will identify fewer events as repeating earthquakes for a given cross correlation threshold, however they are more likely to be spatially correlated (Geller & Mueller, 1980). We chose a 95% cross correlation threshold as this is a typical value chosen to try to capture ruptures that occur on the same fault patch (Baisch et al., 2008); however, a lower cross-correlation threshold would give a similar set of events if a higher cutoff frequency was used to filter the data. Thus, it is necessary to consider both the cutoff frequency (the possible separation distance of the repeating earthquakes), the location uncertainty of the earthquakes, and the cross-correlation

threshold used when assessing whether two earthquakes can be considered repeaters. As in other studies, we refer to earthquakes that meet the criteria we have determined for repeating earthquakes as a “family”. We check that our repeating earthquake definition is satisfactory by analyzing whether the families of events have overlapping ruptures (Figure 2). For all of the repeating earthquakes that we delineate in this paper, only two families contain earthquakes that do not spatially overlap with their families, meaning that in the majority of cases a given family is rupturing the same fault patch (Figure S2). This shows that our criteria for repeating earthquakes is robust, however this method relies on approximations of moment and stress drop. Therefore, we did not treat this as a way to filter out earthquakes from our repeating earthquake database.

The depth to the basement is resolved from nearby well logs, and varies from 1.8-2.2 km (Keranen et al., 2013). To verify whether repeating events occurred in the sedimentary units or basement units, we analyze their waveforms for the exclusion or inclusion of an S-P conversion. An S-P conversion in these waveforms shows that the earthquake occurred below this interface i.e., in the basement rock.

Figure 2: 1.2 Repeating Earthquake Methods

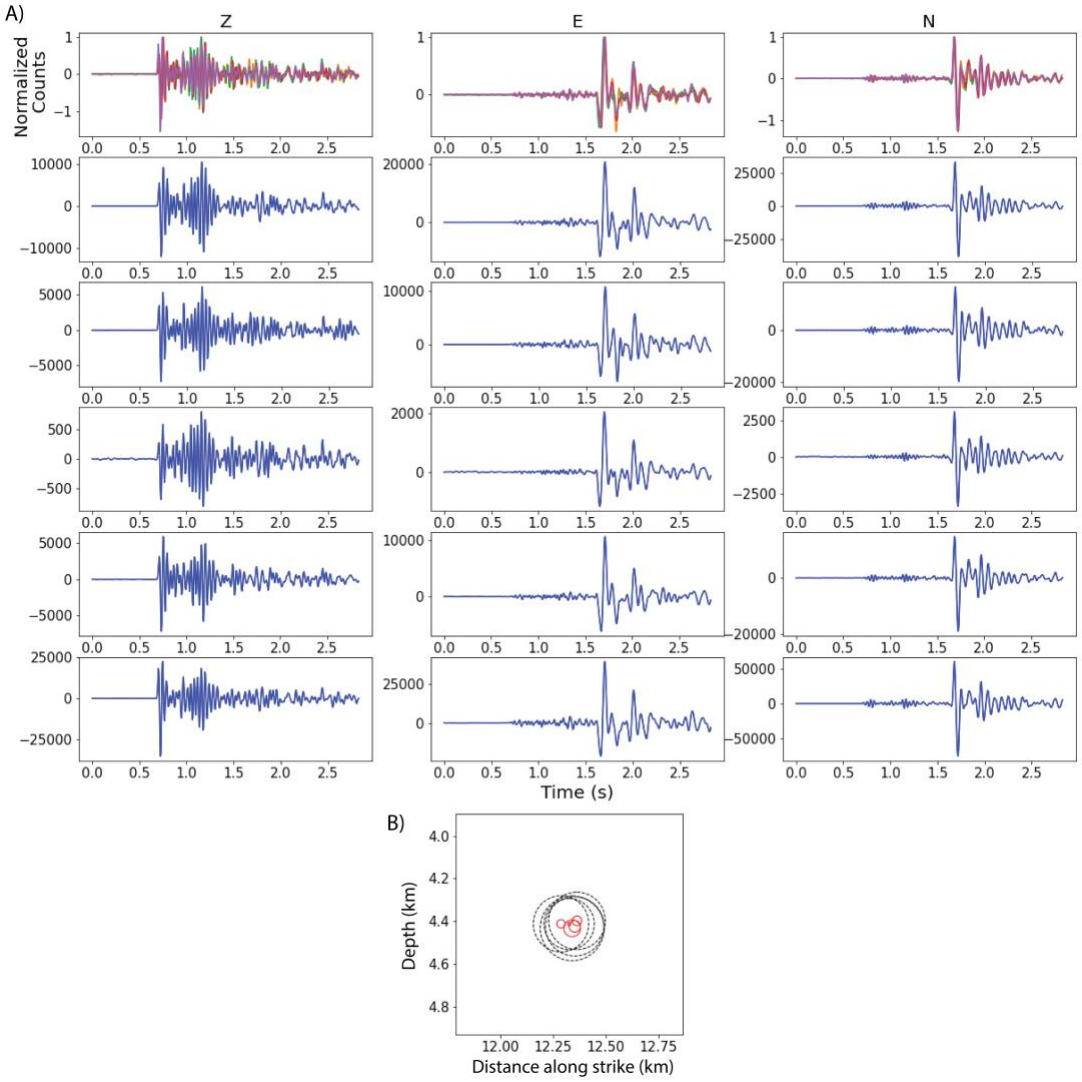

Figure 2: A) Normalized seismograms for family 1 with a 1-25 Hz band pass filter recorded at station LC01 and the non-normalized seismograms below them. The three-component records, Z, E, and N, are shown. **B)** Relative locations of the repeating earthquakes of family 1. Red circles show the radii of the ruptures assuming a 10 MPa stress drop. Dashed black circles show the radii with location error. This is shown for each family of repeating earthquakes in the supplement Figure S1.

4. Results

We find 56 families of repeating events following the Mw 5.7 earthquake (Data Set S1), consisting of 142 individual events in total. The events range in magnitude from -0.14 to 2.55 with 88% having a magnitude greater than 0.5. In map view, we find that most of the repeaters occur within the central portion of the sequence in areas of complex faulting (Figure 3A). Faults were estimated as best-fit planes to aftershock clusters using the FaultID algorithm (Cochran et al., 2020; Skoumal et al., 2019); the primary structures (Faults A, B, and C) match closely to previously mapped structures determined from seismic data and drill cores (Way, 1983). Four faults intersect the mainshock fault (Fault B). Fault C does not directly intersect with fault B based on the fitted fault planes. However, faults are zones of deformation, rather than planes, and devising fault intersections with best-fit planes has inherent uncertainty. We find that the total thickness of the aftershock zone for Fault B (perpendicular to the best-fit plane) is 300 m, which is a similar aftershock thickness established for Fault C (Savage et al., 2017) and as established for other faults in outcrop (Savage & Brodsky, 2011). Because the gap between the two fitted faults is less than 200m we assume that the fault zones intersect. In order to account for this in our cross sections, we represent the fault intersection of faults C and B as the easternmost edge of Fault C. Fault C may extend upwards farther than the fault plane fit suggests, so we also extend the easternmost edge upwards such as in Savage et al. (2017).

Most of the repeating earthquakes occur either along or at fault intersections with Fault B and therefore, we further examine the location of repeating events within the plane of the mainshock (Figure 3B). We determine the spatial variation of regular aftershock event density within 500 m x 500 m grids, similar to Cochran et al. (2020), and include the location of fault intersections as well as mainshock slip contours as calculated by Sun and Hartzell (2014) (Figure 3B). There is a zone of high aftershock density as defined by green-yellow colors and is located roughly between the intersections of the main three faults. This high-density aftershock patch roughly coincides with the area that experienced the most co-seismic slip during the mainshock (Sun and Hartzell, 2014; slip contours on Figure 3). Given the uncertainty in slip inversions of moderate sized earthquakes (Zahradník & Gallovič, 2010), we use this slip inversion as a guide and try not to overinterpret the locations of these slip patches. In addition, repeaters occur in other areas of high event density. While only 1.7% of aftershocks are repeaters, 41% of aftershocks occur in the event density bins that also contain repeating earthquakes. In summary, Figure 3 shows that most repeating earthquakes are located at the intersection of the three main faults, next to mainshock slip patches, and within areas of peak event density.

We focus on three main groups of repeating families that exist in areas of known geologic and/or structural heterogeneity, referred to as Groups 1, 2, and 3 (Figures 3 and 4). Some repeating earthquakes are located in other areas, but they mostly occur on other faults and are not involved in postseismic activity on the mainshock fault. These three groups of repeating earthquakes exist at the

basement/sedimentary rock interface and/or at the intersections of faults. The 17 families we assign to Group 1 occur in the Arbuckle unit just above the basement interface, ~1 km above the mainshock hypocenter, and at the upper edge of the aftershock activity. Furthermore, Group 1 is located at the intersection of the foreshock and mainshock fault planes (i.e., Faults A and B). Group 2 includes 3 families and is located at ~4.5 km depth at the intersection of mainshock and aftershock fault planes (Faults B and C). The deepest group, Group 3, has 19 families that occur at the intersection of the foreshock and mainshock faults (Faults A and B) near the base of the seismicity. The remaining families not within these groups are primarily located about 500-1000 m below the sediment-basement contact or on other faults.

Figure 3: 1.3 Repeating Earthquake Map

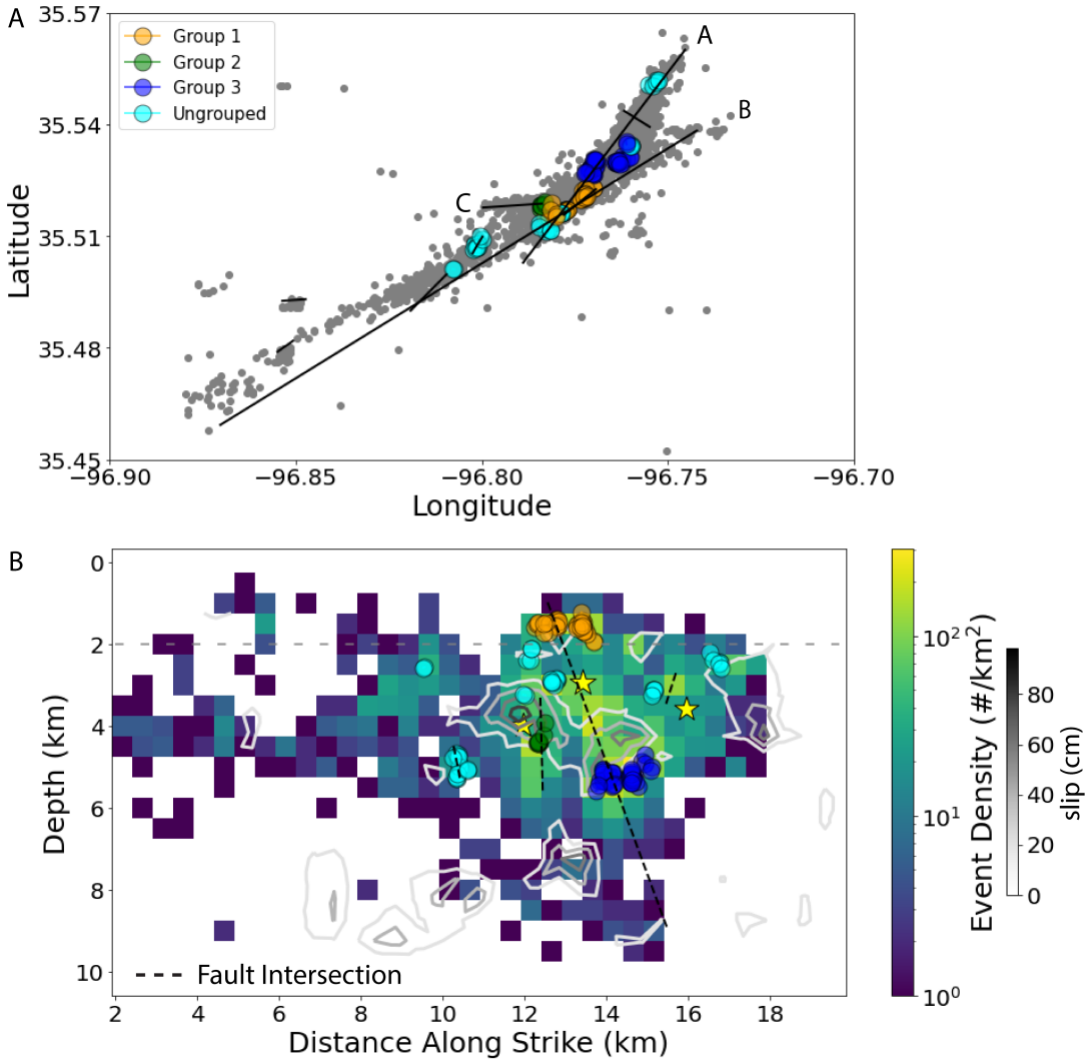

Figure 3: A) Map view of seismicity and mean location of 56 repeating families compared to the fault planes determined by Cochran et al. (2020). We highlight three groups of repeating earthquake families: Group 1 (orange circles), Group 2 (green circles), and Group 3 (blue circles). Additional ungrouped families are shown by cyan circles. The faults are mapped as black lines and the three main faults (A, B, C) are labeled. This color scheme will continue into the next figures. **B)** Fault B Along-strike profile of event density and the locations of the repeating events in circles with colors indicating groups as in A. Yellow stars are the location of earthquakes A, B, and C. The dashed black lines show where other faults intersect the mainshock fault

plane. The dashed grey line shows the approximate depth for the basement-sediment interface. The slip distribution is contoured with gray lines.

The locations of repeating earthquake families correlate well with peaks in the depth distribution of aftershocks (Figure 4). However, the repeaters are not responsible for the peaks in the depth distribution, suggesting repeaters tend to occur in regions with overall higher aftershock rates. The largest concentrations of repeating earthquakes are located near the top (~1 km depth) and bottom (~5-6 km depth) edges of aftershock seismicity (Fig. 4A). In general, repeating earthquakes decay with time from the main event, which is indicative of afterslip. In addition, their recurrence interval increases with increased time from the main event indicating that slip rate is decreasing (Figure S1). We observe that repeating earthquake families have variable durations lasting from less than 1 day to 53 days. Patches of long-lived (>30 days) repeating earthquake areas strongly correlate with peaks in the depth distribution of earthquakes. Group 1 (shallowest families located in the Arbuckle) decays more slowly in time than Group 3 (deepest families) and many of the ungrouped families. Group 2 only lasts for a month and has a limited number of events (Figure 4B). The differences in duration of the different families may reflect differences in rheological behavior and stressing conditions.

Figure 4: 1.4 Depth Distribution and Timing

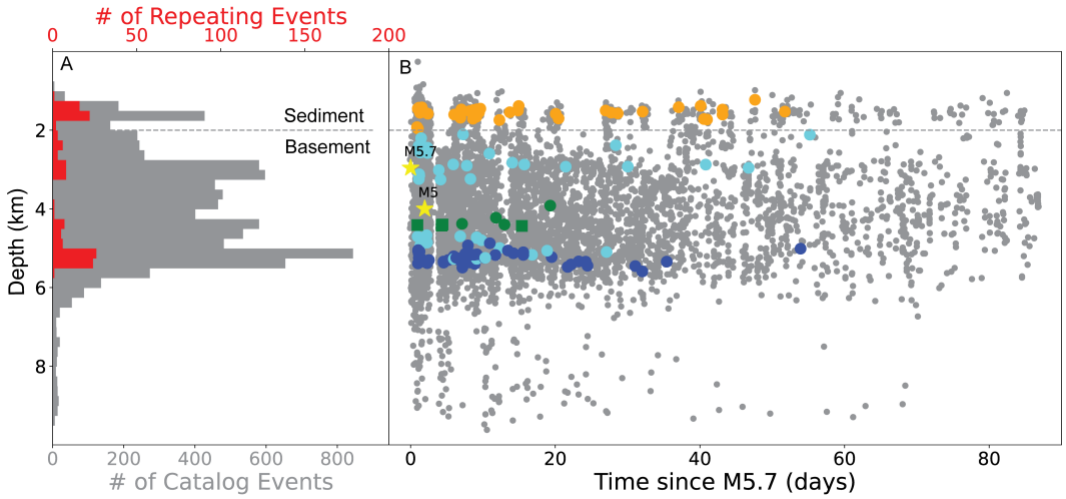

Figure 4: A) The depth distribution of the full catalog (grey) and repeating earthquakes (red) with each bin showing the number of earthquakes in a 0.25 km depth range. **B)** Full catalog (grey) and repeating earthquakes (colored dots) in time; colors are the same as figure 3 (orange is group 1, green is group 2, dark blue is group 3, and cyan is other basement families). The M5.7 mainshock and M5.0 aftershock (Events B and C) are highlighted as yellow stars. Event A is not shown because it occurs before the M5.7 (x=0 days). The dashed line shows the approximate depth for the basement-sediment interface.

5. Discussion

Identifying and mapping repeating earthquakes allows us to consider different mechanisms for aftershock production. We have shown that families of repeating earthquakes coincide with areas of high aftershock density and long aftershock durations (Figures 3, 4). This suggests that aseismic slip, as inferred from repeating earthquakes, is driving some of the seismicity in these areas. In particular, afterslip at the upper and lower limits of the main coseismic rupture extent may explain the peaks in the depth distribution of earthquakes. The co-location of repeating earthquakes and high event density suggests that ~41% of aftershocks could be caused by afterslip.

This supports the view that aftershocks along portions of a fault can be dominantly produced by afterslip (Perfettini & Avouac, 2004) as opposed to being produced directly from static or dynamic stress changes from a mainshock (Dieterich, 1994; Felzer & Brodsky, 2006). However, there are also aftershocks where repeating earthquakes do not occur, such as within the mainshock rupture zone, that are likely due to static and dynamic stress changes of the mainshock. Below we go into more detail on the relationship between afterslip and aftershocks through space and time, potential stress and frictional states that can give rise to different slip styles, implications of precursory slip, and the role that slow slip may play in induced seismicity.

5.1 Occurrence of afterslip, repeaters, and regular aftershocks

There are a number of explanations for the location of afterslip including variations in frictional parameters (Kato, 2007; Marone et al., 1991), diffusion of pore fluid pressure (Booker, 1974; Nur & Booker, 1972), and stress heterogeneity (Helmstetter & Shaw, 2009). The following 3 sections discuss the location of our repeating earthquake groups to try to distinguish between these explanations. Importantly, any plausible scenario would need to allow for slow slip, regular aftershocks, and possibly mainshock slip, to occur in the same location. In order to make our interpretations, we simplify the slip inversion of Sun and Hartzell (2014) to a cartoon version of this mainshock slip patch that occurs between groups 1 and 3. We show both the largest slip patch from the slip inversion and this cartoon version of

the slip patch in Figure 5. It should be noted that this is only the largest slip patch and there are other slip patches including a few that occurred directly next to group 1 as shown in Figure 3b.

Figure 5: 1.5 Material Property vs Stress Control

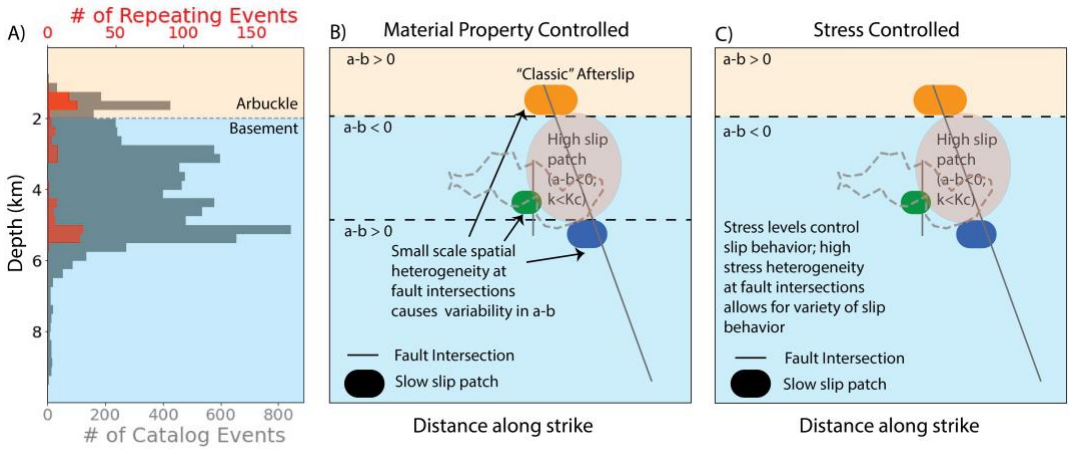

Figure 5: A) Depth distribution of repeating events and catalog events as described in Figure 4. **B)** Cartoon of Prague M5.7 mainshock fault cross-section as seen in Figure 3B, surrounding stress concentration and inferred slow slip patches. Slow slip patch colors match repeating earthquake group color. Dashed black lines represent the estimated depth transition in stability that are labeled with frictional parameter conditions for a steady-state, rate-state framework. The area in dashed gray lines shows the largest slip patch from the Sun and Hartzell (2014) slip inversion. **C)** Cartoon similar to figure B. Labeled with the frictional parameters for a non-steady-state, rate-state framework.

5.2 Variations in frictional parameters

Steady-state, rate-state friction models often invoke changing frictional parameters to produce various slip responses. Typically, models suggest that afterslip occurs primarily in the upper few km of the fault zone and at the base of the seismogenic zone in areas of velocity strengthening behavior (Marone et al., 1991;

Perfettini & Avouac, 2007). Groups 1 and 3 could be indicative of changes in frictional properties with depth. We explore that possibility here and then discuss the possibility of afterslip along-strike of the primary slip patch of the mainshock rupture.

Repeating earthquakes in the sedimentary layer (group 1) could be interpreted as shallow afterslip on a strike-slip fault, where a rupture from below creates a stress increase in an overlying velocity-strengthening layer (Marone et al., 1991). This velocity strengthening layer could be caused by changing lithology or a change from consolidated to unconsolidated sediments (Marone & Scholz, 1988). Here we can link this shallow slip to a change in lithology from primarily granitoids to sedimentary rocks. The existence of a velocity-strengthening layer must be reconciled with the fact that repeating earthquakes require some velocity-weakening asperities. This is plausible given that the Arbuckle Group is composed of heterogeneous areas of limestone and dolomite. These rocks experienced extensive hydrothermal alteration and multiple dolomitization events that could have created frictional heterogeneity (Al-Shaieb & Lynch, 1993; Faith et al., 2010). Experimental analysis of the frictional stability of heterogeneity within the Arbuckle group could shed light on the issue. The overall lack of seismicity in the Arbuckle anywhere besides the slow-slipping patch suggests that it is predominantly velocity strengthening, although this could also be caused by fluid pressure decreasing k_c, which would stabilize slip.

The lower limit of the seismogenic zone in Oklahoma is not well explained by a typical change to rate-strengthening behavior. Group 3 occurs in the basement rock at a depth of 5.5 km which is also approximately the base of seismicity, which is

similar to lower depth limits documented throughout Oklahoma and southern Kansas (Schoenball & Ellsworth, 2017). Such agreement suggests that the bottom of the seismogenic zone is around 5-6 km, which is far shallower than the 15-20 km that is expected for crustal faults at plate boundaries (Scholz, 1998). The transition for Oklahoma faults should be closer to 13 km given a 23° C thermal gradient (Harrison et al., 1982) and an onset of quartz plasticity at 300°C. Experimental results show that the basement rock of Oklahoma is velocity-weakening from 4-9 km (Kolawole et al., 2019). This suggests that a physical mechanism other than quartz plasticity is needed to explain the general paucity of earthquakes at greater depths. We suggest that the stress perturbations related to induced seismicity, either directly related to pore pressure or poro-elastic stresses, are not reaching depths below around 5-6 km (Goebel & Brodsky, 2018). Other possibilities are that the strength of the faults at greater depths may be higher than tectonic faults given extensive healing since the last significant earthquakes or that the fault does not extend past ~6 km.

Given the overall coseismic slip and aftershock patterns, both groups 2 and 3 must be explained by slow slip in a generally velocity-weakening area. This slow slip may coexist with the mainshock rupture area given that Group 2 is in the coseismic slip patch as shown in Figure 3. Asperity models that represent ruptures as highly heterogenous patches of velocity weakening and velocity strengthening zones may explain the variable slip behavior (Boatwright & Cocco, 1996; Lay & Kanamori, 1981). Fault intersections could be areas of small-scale spatial heterogeneity that could be explained by asperity models. This could be caused by varying pore

pressures in permeable fault damage zones, small scale lithological variation, or changes of gouge width (Marone & Kilgore, 1993; Scuderi & Collettini, 2016). Areas of velocity-strengthening material could result in a patch of aseismic slip with embedded small asperities on which the repeaters occur. This would explain the general occurrence of repeating earthquakes at fault intersections; however it does not explain group 2 being within the mainshock area.

5.3 Diffusion of Pore Fluid Pressure

As mentioned earlier, pore pressure can allow a fault to slide by lowering the effective normal stress. The critical stiffness (k_c) from rate-state friction is lowered when pore pressure is increased thus promoting aseismic slip. In addition, experiments have shown that high pore fluid pressure may also lead to more rate-neutral or more rate-strengthening behavior (Bedford et al., 2021; Scuderi & Collettini, 2016). There are two issues with fluid pressure causing aseismic slip in these areas, one is the timescale of aseismic slip and the other is the isolated patches where the aseismic slip occurs. In general, fault intersections should be areas of high permeability due to fault damage where fluids could readily flow, and pore pressures could diffuse away. A recent 3D seismic study suggest that the intersection of faults A and B are indeed very permeable (He et al., 2021). Therefore, we think it unlikely that the slow slip seen at fault intersections, especially over the extended time periods of some of our repeating families, is due to high fluid pressure. In addition, while small fluid perturbations can cause aseismic slip, these fluid perturbations would have to be

isolated. Given that pore fluid pressure would diffuse throughout the damage zone, we would expect a broader area of aseismic slip both along the fault intersection and along the fault trace itself if fluid pressures were the main cause of the aseismic slip seen here.

5.4 Stress Heterogeneity

The rate-state framework is commonly invoked to explain natural observations with an assumption that the system is close to steady state. This steady state assumption leads to the criteria that if a-b<0 and k<k_c then an area is unstable. However, an aftershock sequence is a transient phenomenon that occurs far from steady state. In addition, our results show that we have nearby or even overlapping areas of unstable and stable slip, which would require small scale changes in a-b or k required in this steady state framework. Here, we use a non-steady state rate-state friction framework as a way to explain nearby and overlapping areas of unstable and stable slip (Helmstetter and Shaw, 2009). This framework is built upon the nonlinear stability analysis of Ranjith & Rice (1999) and Gu et al. (1984). They showed that the stability of an area depends only on stress conditions when the load point is stationary, a-b<0, and $k < k_c$. We assume that the load point for the aseismic slip is stationary for an aftershock sequence and continue with this stability criteria.

Using this framework, there are two stability transitions that depend on stress conditions. Both transitions occur when the area is velocity weakening and when the stiffness is less than the critical stiffness. The condition for an aftershock using the

aging law is such that the initial stress must be larger than some critical stress. This critical stress can be caused by normal or shear stress changes, so it can be evaluated in terms of a critical friction coefficient:

$$\mu_l(V) = \mu_{ss} - bln(1 - k/k_c), \quad (1)$$

where $\mu_{ss}$is friction at steady state, b is the evolution parameter, k is stiffness, and k_c is the critical stiffness (Helmstetter & Shaw, 2009; Ranjith & Rice, 1999). A similar transition is found for the slip law except that aftershocks are more prevalent and are possible even when $k > k_c$ (Gu et al., 1984; Helmstetter & Shaw, 2009). The second stress condition separates slow earthquakes from slow slip that decays with time. Slow earthquakes are defined as slow slip that accelerates and then decelerates instead of continually accelerating into an earthquake. Slow earthquakes occur when the stress conditions are greater than a critical friction coefficient:

$$\mu_a(V) = \mu_{ss} - bln(1 - k/k_b), \quad (2)$$

where k_b is equal to $\frac{b\sigma}{D_c}$ (Helmstetter & Shaw, 2009). This stiffness criterion is the same as that shown in Dieterich (1992), where $k_{crit} = \frac{b\sigma}{D_c} + \frac{\dot{\tau}}{C}$, but for a negligible loading velocity. This transition marks the ability for the system to accelerate. These equations show that stress condition of an area allows for different slip styles, such

that afterslip occurs when $\mu < \mu_a$, slow earthquakes when $\mu_a < \mu < \mu_l$, and earthquakes when $\mu > \mu_l$.

Our results suggest that a variety of stress conditions exist at fault intersections. In particular, slow slip at fault intersections exists because a large portion of the intersection is under less stress than the critical stress. Interspersed areas of higher stress relative to the critical stress causes small aftershocks. High stress concentrations at fault intersections are expected and are suggested by previous modeling of this earthquake sequence (Norbeck & Horne, 2016; Sumy et al., 2014). While overall the fault intersection is a stress concentration, geometrical effects of fractures within the damage zone would cause large stress variations on smaller scales.

There is one more observation that has not been explained by the framework above. The Arbuckle Group is located at depths of 1-2 km and frictional stability analysis of carbonates suggests that this area could be velocity strengthening or velocity weakening (Carpenter et al., 2016a; Kolawole et al., 2019). Current frictional analysis suggests that the basement rock is velocity strengthening from 2-4 km where many of earthquakes occurred (Kolawole et al., 2019). While the exact conditions of pore pressure, confining pressure, and temperature may not be represented by these experiments, it seems likely that some significant number of earthquakes in the Prague sequence are located within the velocity strengthening regime as determined by laboratory sliding velocities. The question now is, why are there earthquakes in a velocity strengthening area? Equation 2 does not require that $a\text{-}b < 0$ to have a slip

acceleration, so we start with this equation. These slip accelerations will be small and decelerate with slip (Helmstetter and Shaw, 2009). However, this framework does not take into account variation in a-b with any weakening mechanism that may occur as slip patch accelerates. Therefore, we find it possible that earthquakes could occur given that $a\text{-}b > 0$, $k < k_b$, $\mu > \mu_\alpha$, and that some weakening mechanism is activated during the initial acceleration, such as thermal weakening (Di Toro et al., 2011).

Stress heterogeneity due to slip heterogeneity has been invoked to allow for aftershocks in a mainshock area (Marsan, 2006). Given enough stress heterogeneity, our group 2 results indicate afterslip may also be plausible in a high slip area of the mainshock. This level of stress heterogeneity seems to only be present at this fault intersection and not outside of it. Overall, stress heterogeneity is the only mechanism that can explain the co-occurrence of afterslip, aftershocks, and mainshock slip without invoking large changes in lithology or pore fluid over very small spatial scales.

5.5 Implications for Precursory Slip

The triggering of the Mw 5.7 mainshock by the Mw 5.0 foreshock through static stress change and poroelastic changes has been previously suggested (Norbeck & Horne, 2016; Sumy et al., 2014); however, the cause of the Mw 5.0 aftershock (Event C) is less clear. Event B imparted a negative coulomb stress change onto Fault C, and Fault C was not optimally oriented within the stress field for failure (Sumy et al., 2014; Cochran et al., 2020). Fault C could be brought to failure from high

pressure fluid migration from Fault B (Cochran et al., 2020; Norbeck & Horne, 2016) which may have begun as slow slip close at the intersection of Faults B and C (Savage et al., 2017).

The location and timing of some of the repeaters found in this study overlap with events from Savage et al. (2017). We cannot exactly match repeaters across the two studies because the events used here have less precise relocations. Even so, our data support the idea that Event B triggered precursory slip on Fault C that may have led to the nucleation of Event C. In addition, we find that aseismic slip continues near the fault intersection after Event C. This is shown by one family of repeating earthquakes (shown as the squares figure 4) occurring at the same location both pre- and post-Event C.

We suggest that the slow slip after Event B at the intersection of Faults B and C could be sufficient to bring Fault C to failure even in the absence of pore fluid changes. The Mw 5.7 mainshock may have been triggered in a similar way, but we do not have sufficient data during this period to confirm or refute this supposition. While we cannot rule out other triggering mechanisms, the observations of repeating earthquakes between Events B and C at the fault intersection suggests that aseismic slip is possible mechanism that could cause time-delayed triggering of Event C.

5.6 Implications for Induced Seismicity

Current hazard models for induced seismicity consider fault orientation in the local stress field and pore-pressure changes to be the dominant factors in determining

where moderate to large sized events occur (M > 3). The Mw 5.8 Prague mainshock was consistent with the fault susceptibility hypothesis (Walsh & Zoback, 2016). However, the largest foreshock and aftershock (Events A and C respectively) were on faults poorly-oriented to fail in the local stress field (Cochran et al., 2020). Event A can be explained by pore pressure buildup due to the spatial proximity between fault A and reservoir injection (Keranen et al., 2013). We hypothesize that aseismic slip at the intersections of faults may have led to failure of the M5.0 aftershock plane. Our results suggest that hazard models should consider fault interactions in addition to simply considering the susceptibility of faults to fail based on the local stress field and pore-pressure changes.

6. Conclusion

Using repeating earthquakes and well-constrained geology, we found evidence for afterslip in the 2011 Prague earthquake sequence and evaluated likely mechanisms. We found that repeating earthquakes are generally focused around and within the areas with significant coseismic slip during the Mw 5.7 mainshock. Specifically, we find clusters of repeating earthquakes (Groups 1-3) that occur near the intersections of the three faults that hosted the M_w5.0 foreshock, M_w5.7 mainshock, and M_w5.0 aftershock. The repeating events occur in areas of high overall event density, suggesting that afterslip may drive ~40% of seismicity in these areas. We outlined possible causes of aseismic slip at fault intersections and suggest that stress heterogeneity within a non-steady-state, rate-state framework is the simplest

explanation. Our findings of afterslip driving the occurrence of the M_w 5.0 aftershock suggests fault interactions should be considered in evaluating induced seismicity hazard analysis, especially related to aftershock forecasting. Stress heterogeneity in areas of complicated fault networks is also expected in tectonic regions, making these findings potentially broadly applicable to aftershock sequences.

Acknowledgments

We would like to thank the UC Santa Cruz seismology group, particularly Susan Schwartz, Heather Shaddox, and Emily Brodsky, for helpful feedback and comments on early drafts. We thank two anonymous reviewers, the associate editor, and Nick Beeler for helpful reviews that have greatly improved this manuscript. This material is based upon work supported by the National Science Foundation Graduate Research Fellowship Program under Grant No. 2020259243 and the National Science Foundation Grant No. 81496-443754. Any use of trade, firm, or product names is for descriptive purposes only and does not imply endorsement by the U.S. Government.

Data Availability Statement

Datasets and code used in this study are available at https://doi.org/10.5281/zenodo.6658258.

Chapter 2 - To heal or not to heal? Part I: The effect of pore fluid pressure on the frictional healing behavior of Oklahoma lithologies

Abstract

The competition between fault healing (i.e., re-strengthening) and fault loading determine the seismic cycle. Repeating earthquakes can give observational estimates of fault healing rates, however, it is difficult to link laboratory studies of frictional healing and observed healing rates from repeating earthquakes in part because of uncertainty in lithology at depth. Due to well-constrained and relatively simple geology, earthquakes in Oklahoma can be linked to the Arbuckle group (dolomite) and the basement granitic rock. Carbonates and granitic rock are known to have different frictional behavior and healing properties. Repeating earthquakes are found in both lithologies and have different moment-recurrence time behaviors that indicate different healing rates (see companion paper). Here, we conduct friction experiments to measure healing rates of the two lithologies. We perform friction experiments on the two main earthquake-bearing lithologies at confining pressures representative of earthquake depths and pore pressures ranging from 0 to 80% of the confining pressure. We measure frictional healing by executing slide-hold-slide tests with hold times ranging from 3s to 3000s. The friction experiments on the basement granite indicate that pore fluid pressure does not greatly affect healing rate. On the other hand, the Arbuckle dolomite exhibits decreased healing with increased pore fluid pressure, with a negative healing rate (weakening) at the highest pore pressure. We hypothesize that this is due to an increase in dissolution of dolomite at high pore

pressures. These healing rates are used in the companion paper to understand the moment-recurrence time behavior of repeating earthquakes in Prague, Oklahoma.

1. Introduction

The majority of induced seismicity in the United States has occurred in Oklahoma due to wastewater injection into the Arbuckle group (Keranen & Weingarten, 2018). Yet, a systematic study on the frictional properties of relevant Oklahoma rocks at elevated pore fluid pressure conditions has yet to be conducted. Frictional properties, such as the velocity dependence and healing behavior, combined with fault loading control the seismic cycle (Di Toro et al., 2012; Kanamori & Brodsky, 2004). Faults are loaded from tectonic loading or surrounding transient events, such as aseismic slip (Guglielmi et al., 2015) or far away earthquakes (van der Elst et al., 2013) (Figure 1). In Oklahoma, inactive faults that extend from the Arbuckle group into the basement granitic rock have been reactivated and must either be critically stressed for failure, allowing small changes in pore fluid pressure or small increases in stress from fair-field seismicity to induce earthquakes along them (Ellsworth, 2013; Goebel et al., 2017; Keranen & Weingarten, 2018; van der Elst et al., 2013). In addition, pore fluid perturbations can cause aseismic slip that can lead to nearby seismicity (Cappa et al., 2019; Guglielmi et al., 2015; Savage et al., 2017). Constraints on both the frictional velocity dependence and fault healing for Oklahoma rocks at appropriate conditions can help quantify the strength of these faults and how they might fail.

Frictional healing in the lab is attributed to compaction during the hold that increases contact area and post-hold dilation (Marone & Saffer, 2015), as well as chemical processes that increase contact quality (Renard et al., 2012). One unexplored parameter space for fault healing is variable pore pressure. Recent work on a range of lithologies has explored the effect of high pore pressure on the rate-state velocity dependence of friction (*a*-*b*) (Bedford et al., 2021; Belzer & French, 2022; Scuderi & Collettini, 2016; Xing et al., 2019). Several studies find an increase in *a*-*b* with pore pressure and invoke either dilatant hardening (Xing et al., 2019) or the properties of a thin, adsorbed water film that weakens the gouge to explain the decrease in the value of *b* (Bedford et al., 2021; Belzer & French, 2022). However, increased pore fluid pressure has also been shown to cause a decrease in *a*-*b* in marble and limestone experiments (Scuderi & Collettini, 2016). If the velocity dependence is affected by pore pressure, the healing rate should also change (Marone & Saffer, 2015). In addition to the expectation that pore pressure will change the rate-state parameters that correlate with healing rate, the longer time scale of a hold compared to a velocity step may cause different micromechanical mechanisms to be activated.

Here, we investigate the role of pore fluid pressure on the frictional healing behavior of the Arbuckle group and the basement granite. Injection occurs directly into the Arbuckle formation, while most of the earthquakes occur in the basement granite (Figure 1). Current work indicates that the basement earthquakes are due to fluid migration into the basement (Kolawole et al., 2019) and far-field poroelastic

loading due to increased fluid above the basement (Goebel & Brodsky, 2018; Goebel et al., 2017), typically on critically stressed faults. The effect of pore fluid pressure on both of these lithologies is crucial to understanding seismic behavior in Oklahoma and to understanding the issue of induced seismicity in general.

Figure 6: 2.1 Map of Earthquakes and Injection in Oklahoma

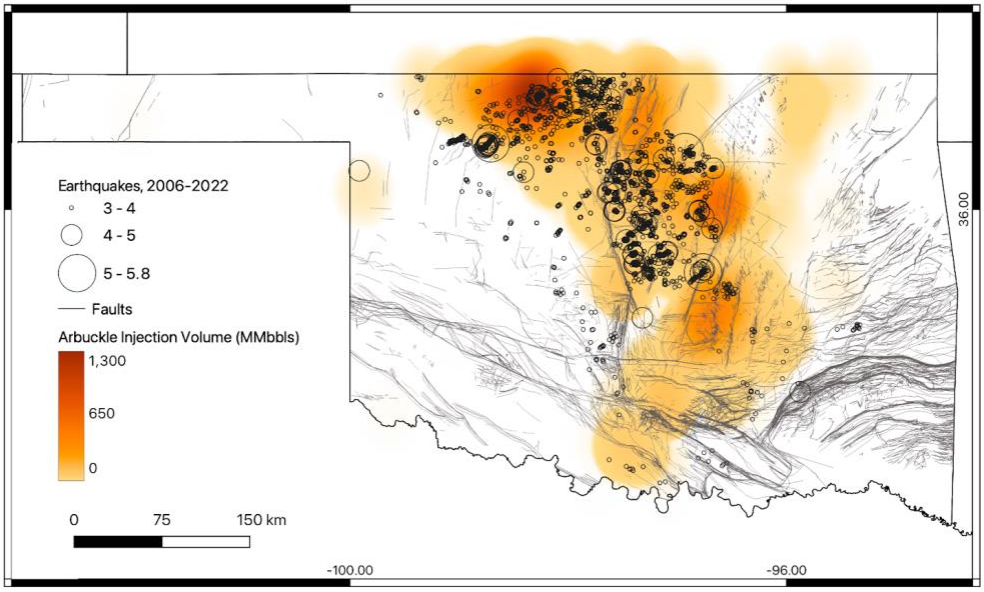

Figure 1: Earthquakes greater than M3 and wastewater injection into the Arbuckle Group from 2006-2022. Faults are shown in gray (data from https://www.ou.edu/ogs/data/fault). Injection volume is in millions of barrels (MMbbls) (data from https://oklahoma.gov/occ/divisions/oil-gas/oil-gas-data.html).

2. Background

Friction at sliding velocities relevant for nucleation processes is modeled with the rate-state equations. Following an increase in velocity, the rate term describes a sudden increase in friction, and the state term describes the logarithmic change in friction to a new steady state:

$$\mu = \mu_0 + a\ln(V/V_0) + b\ln(V\theta/D_c), \quad (1)$$

where a and b describe the magnitude of the rate and state terms, D_c is the critical slip distance, V_0 is the initial velocity before the step, V is fault velocity during the step, and θ is the state parameter (Dieterich, 1979; Ruina, 1983). The stability parameter, a-b, describes when stable behavior occurs (a-b > 0) versus when unstable behavior can occur (a-b < 0). This equation is coupled with an evolution law that describes how the state parameter, θ, evolves. Evolution laws include the aging law (Dieterich, 1979) and the slip law (Ruina, 1983):

$$d\theta/dt = (1-V\theta/D_c) \text{ (aging law)}, \quad (2)$$

$$d\theta/dt = (V\theta/D_c)\ln(V\theta/D_c) \text{ (slip law)}. \quad (3)$$

In addition, other evolution laws exist that combine time-dependent and slip-dependent changes in the state parameter (Nagata et al., 2012). In reality, sliding velocity is not a step function from one velocity to another and instead increases according to the apparatus stiffness. The relationship between load point velocity, V_{lp}, and the actual sliding velocity on the fault is described with a spring-slider with a stiffness K:

$$d\mu/dt = K/\sigma_{eff}*(V_{lp} - V). \quad (4)$$

Here, stiffness (K) is in units of MPa/μm and is divided by the effective normal stress (σ_{eff}) to achieve units of friction. Combined, these equations can model laboratory friction and describe how both the frictional parameters of the sliding material (a, b, D_c) and the experimental setup in the lab or surrounding rock in the real world affect the measured frictional response through the stiffness term (K). Materials that can become unstable have an $a\text{-}b < 0$ and a spring stiffness that is lower than the critical stiffness of the material.

Frictional healing, Δμ, is measured as the difference between peak friction on the re-slide to steady state friction (Figure 2D). The healing rate, β, is then calculated by measuring the change in Δμ over a range of hold times. The traditional equation for healing is given by $\Delta\mu = \beta\Delta\log(t_h)$, where t_h is hold time (Dieterich, 1972; Carpenter et al., 2016b). In order to be able to understand how healing evolves from a hold time of zero and to avoid log(time) units, healing can be fit with:

$$\Delta\mu = \beta\Delta\log(t_h/t_c + 1), \quad (5)$$

where t_c is the cutoff time. In this form, the cutoff time can be interpreted as the time it takes to start healing. A greater discussion of the cutoff time and how it scales from the laboratory to the seismic scale is given in our companion paper.

Frictional relaxation, $\Delta\mu_c$, is measured as the difference between friction before the re-slide (typically the lowest friction during the hold) and steady state friction (Figure 2D). Frictional relaxation has been found to inversely proportional to frictional healing for quartz gouge (Richardson & Marone, 1999; Marone & Saffer, 2015). As the relaxation depends on machine stiffness, two machines with different

stiffnesses might allow for a different amount of relaxation for the same hold time and consequently change the measurement of frictional healing (Bhattacharya et al., 2017; Marone & Saffer, 2015). In rate-state theory, decreasing stiffness causes a larger increase in the amount of relaxation for the slip-law than the aging-law (Marone & Saffer, 2015).

3. Methods

Friction experiments were conducted on the two seismically relevant lithologies in Prague, Oklahoma: the Arbuckle group and Troy granite (Keranen et al., 2013). We sampled the Arbuckle group at a depth of 1.83km from the core available at the Oklahoma Petroleum Informative Center (OPIC). Core (#4554) was selected from the OPIC database based on its proximity to Prague, as it was the closest available core with the Arbuckle group (see supplement). The Troy granite was sampled from an outcrop in the Martin Marietta Aggregates quarry of south-central Oklahoma (Kolawole et al., 2019). XRD analysis of the Arbuckle group sample indicates that it is 90% dolomite and ~10% quartz (see supplement).

Experiments were conducted at UC Santa Cruz in a triaxial deformation apparatus with a single direct-shear configuration (Figure 2). The sample holder consists of two L-shaped halves that allow for a central gouge layer to be sheared when they are moved relative to one another (Faulkner et al., 2018; Samuelson & Spiers, 2012). Two spacers are required to fill the void spaces of this configuration. Here, we use an elastic silicone spacer made of Dragon Skin(™) Very Fast 10. A

2mm x 38.1mm x 50.8 mm volume of gouge is placed in between the two L-blocks. Once assembled, the sample configuration is cylindrical. The gouge was made by crushing the intact samples with a ball mill and sieving to a grain size between 45 μm and 125 μm. We use a load cell that is internal to the confining vessel and three internal linear variable differential transformers (LVDTs). Two vertical LVDTs measure shear displacement of the fault gouge and one radial LVDT measures compaction/dilation of the sample. The radial LVDT is attached to the jacket, which can move with shear displacement. Therefore, it is only used to analyze compaction while the sample is stationary. The vertical LVDTs are particularly useful in measuring deformation of the gouge during the hold. Pore pressure is input both from each side of the sample through porous alumina frits. A removable plate with teeth is attached to both sides of the L-blocks. The teeth on these plates force slip to localize within the sample instead of along the edges of the sample. Each plate is channeled to allow for flow from the porous frits to ~130 perforations evenly distributed on the face of the teeth. This creates an even distribution of pore fluid pressure across the sample and allows the gouge to drain more efficiently (Figure 3).

Repeating earthquakes occur around 2 km depth within the Arbuckle and over depths of 2-5 km in the basement granite (Okamoto et al., 2022). To reflect pressure at hypocentral conditions (~2km for Arbuckle and average of 4 km for the basement granite), the Arbuckle group experiments were performed at 50 MPa confining pressure (P_c) and the Troy granite experiments at 100 MPa P_c. We analyzed three different pore pressure (P_p) conditions for each lithology with P_p/P_c equal to 0, 0.2

and 0.8. We also performed an experiment with $P_p/P_c = 0.6$ for the Arbuckle dolomite in order to test whether there is a balance between healing and weakening. A repeat experiment with $P_p/P_c = 0.8$ for the Arbuckle is in the supplement. In order to reach pressure conditions, confining pressure was brought up to the final desired effective stress. For tests with pore fluid pressure, the pore pressure system was vacuumed in order to ensure no air was present in the system and subsequently filled with deionized water. The confining pressure was computer controlled and raised by 2 MPa while pore pressure was manually raised by 2 MPa before switching pore pressure to computer control. Once in computer control, the confining pressure and pore pressure were raised simultaneously to the final desired pressures at a rate of 10MPa/minute. We equilibrated our sample for one hour to allow for a steady-state porosity to be reached, which was determined by the decay in sample thickness measured by the radial LVDT. The sample was sheared over a typical run-in distance of 2.3 mm at 1 μm/s, followed by a series of velocity steps and slide-hold-slides with sliding velocity equal to 3 μm/s. The slide-hold-slides had hold times ranging from 3s to 3000s with a displacement of 0.3 mm during each slide. Velocities during velocity steps were typically done from 1 μm/s to 3 μm/s to 10 μm/s and back down to 3 μm/s with a displacement of 0.3 mm at each velocity. When possible, we performed a repeat 300 second hold after the 3000 second hold and repeat velocity steps after this, where we stepped velocity down from 3 to 1 μm/s and back up to 3 μm/s before unloading at a rate 3 μm/s.

We preserved the post-experiment microstructures by using a razor blade and removing as much intact gouge material as possible from the shear interface. We then epoxied the gouge using MAS low viscosity resin and MAS slow hardener. The gouge and epoxy were subjected to a vacuum of 25 inHg for a few minutes and then a 5 inHg vacuum overnight to harden. Polished thin sections were made from the epoxied pucks by Wagner petrographic in the direction of shearing. Two experiments (UC55 and UC57) were analyzed in depth for microstructural differences. These thin sections were imaged in an Thermo Scientific Apreo scanning electron microscope. Images with a pixel size of 67.45 nm were collected and stitched together using the Thermo Scientific Maps application. A portion of this stitched image was then input into Imagej in order to calculate grain size characteristics. The images were converted to 8-bit grayscale images and the grains were segmented using the grayscale threshold method. The grains were then analyzed using Imagej's analyze particles method, which computes a number of parameters including solidity, circularity, and aspect ratio of each particle. The particle outlines were visually analyzed to ensure they were well-defined and accurate.

Figure 7: 2.2 L-block Setup and Friction Methods

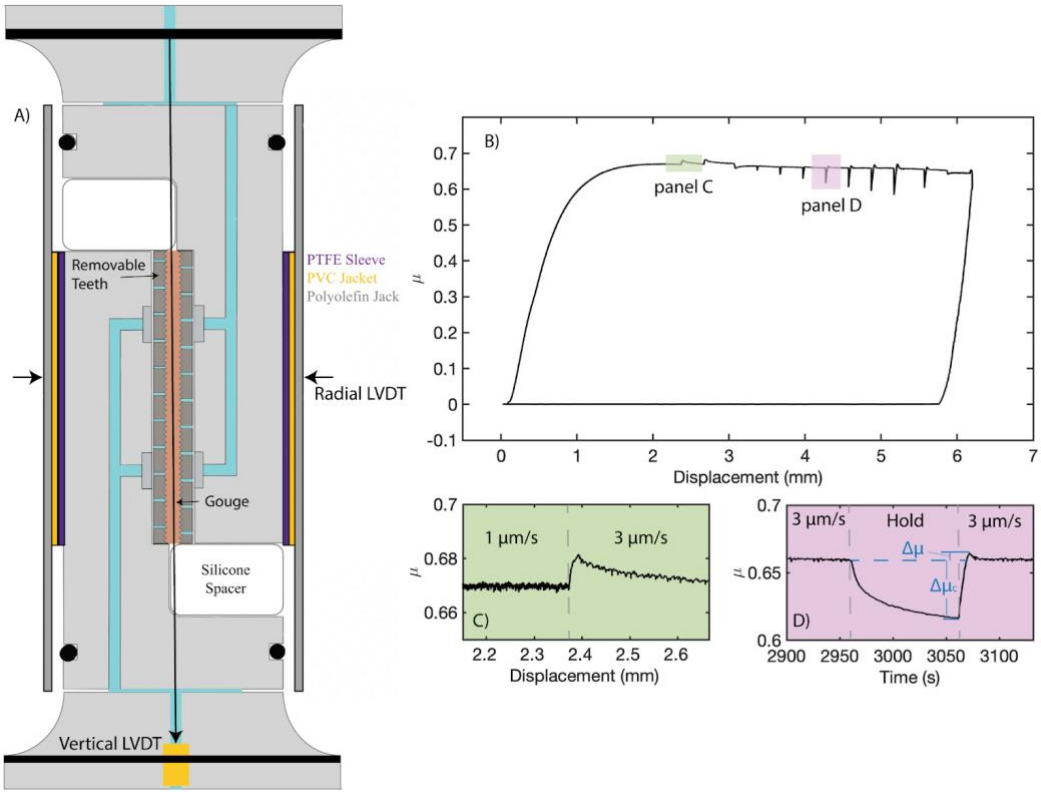

Figure 2: A) The L-block setup used in these experiments is a direct-shear design for a triaxial deformation apparatus. Two pore fluid ports allow for fluid to flow through the sample. The removable teeth detach from the L-blocks and have 130 holes that allow for distributed pore fluid pressure throughout the sample. The radial LVDT measures compaction/dilation as well as jacket movement and the vertical LVDT measures displacement at the sample instead of at the load point. The vertical LVDT is held into place on the end blocks. Another vertical LVDT of the same setup is on the other side of the sample. **B)** Friction versus displacement for Experiment 54, where the gouge is the Arbuckle dolomite, normal stress = 50 MPa, and pore pressure = 0 MPa. **C)** A velocity step from 1 μm/s to 3 μm/s. **D)** A single slide-hold-slide as a function of time, showing how $\Delta\mu$ is measured and $\Delta\mu_c$ are measured.

Exp UC#	Material	Confining Pressure (P_c) (MPa)	Pore Fluid Pressure (P_p) (MPa)	Effective Stress (MPa)	P_p/P_c
49	**Troy Granite**	**100**	**4**	**96**	**0.04**
50	**Troy Granite**	**100**	**80**	**20**	**0.2**
52	**Troy Granite**	**100**	**20**	**80**	**0.8**
54	**Arbuckle Dolomite**	**50**	**0**	**50**	**0**
55	**Arbuckle Dolomite**	**50**	**10**	**40**	**0.2**
57	**Arbuckle Dolomite**	**50**	**40**	**10**	**0.8**
58	**Arbuckle Dolomite**	**50**	**30**	**20**	**0.6**

Table 1: Pressure conditions of the experiments conducted for this study.

4. Results

The Arbuckle dolomite and the Troy granite exhibit typical steady-state behaviors for their lithologies. The Arbuckle has a higher steady-state coefficient of friction (0.7) at all effective pressures each condition than the Troy granite (~0.6) except for the highest pore pressures, which is consistent with previous results that carbonates have higher steady state-coefficients of friction than granites (e.g. Byerlee, 1978.). At the highest pore pressures, the Troy granite and the Arbuckle dolomite have steady state coefficients > 0.7. At high pore pressures (low effective stresses), grain fracture is less common, and instead grains are required to dilate during loading,

which should cause a higher steady-state coefficient. Steady-state friction evolves during shearing for the high pore pressures in a manner consistent with overcompaction in the Reynolds dilation curve (Reynolds, 1885). This dilation curve is indicated by a very high friction coefficient (> 0.9) initially (indicative of a compactive phase) that then decays to a high, but still typical steady-state coefficient for rock of 0.7-0.8 that is indicative of a dilation phase (Figure 3) (Byerlee, 1978). This curve is not shown in Figure 2 for the Arbuckle high pore pressure experiments as we unloaded the sample after the compactive phase and then reloaded the sample. Continued dilation during shearing can only occur when overcompaction has occurred. Here, slight over-compaction was likely due to the vacuuming of pore pressure lines prior to the experiment (see methods). This amount of overcompaction would not cause grain crushing or other more permanent changes in the gouge and therefore likely does not affect our healing results.

Figure 8: 2.3 Steady-State Friction

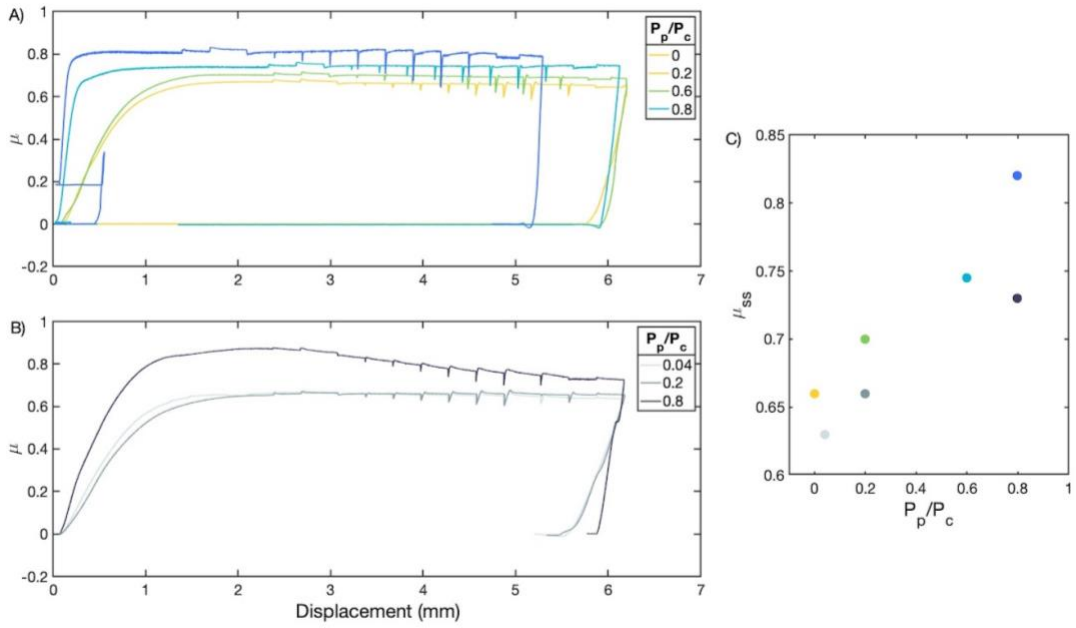

Figure 3: A/B) Steady state friction as a function of displacement for Arbuckle dolomite **(A)** and Troy granite **(B)** at a variety of pore pressures. Confining pressure was 50 MPa for the dolomite and 100 MPa for the Troy granite. **C)** Steady state friction versus pore pressure/confining pressure.

The Arbuckle dolomite has a lower healing rate and higher stress relaxation than the Troy Granite at the conditions tested. Both lithologies exhibit higher amounts of healing when stress relaxation is lower. Remarkably, the Arbuckle dolomite exhibits decreased healing and increased relaxation with increased pore pressure (Figures 4 & 5). At zero pore pressure, the Arbuckle dolomite displays typical Dieterich-type healing behavior with a healing rate of 0.005 $\Delta\mu/s^{-1}$. With increased pore pressure, the healing rate decreases. At a fluid pressure of 30 MPa, the healing rate is close to zero. At a fluid pressure of 40 MPa (effective pressure of 10 MPa), the Arbuckle weakens with time at a rate of -0.005 to -0.01 $\Delta\mu/s^{-1}$. The cutoff time increases with pore fluid

pressure in the Arbuckle experiments (Figure 5B). The Troy granite exhibits a slight decrease in healing rate with pore fluid pressure, however the change in healing rate is small from 0.01 to 0.006 $\Delta\mu/s^{-1}$. The accompanied increase in stress relaxation is also very small and there is no increase in the stress relaxation rate from a pore pressure of 20 MPa to a pore pressure of 80 MPa (Figures 4 & 5). The cutoff time is small at the highest pore fluid pressure for the Troy granite. For both lithologies, at high pore fluid pressures, slide-hold-slides do not return to the same steady state for long hold times (Figure 3A/B).

Figure 9: 2.4 Healing and Relaxation

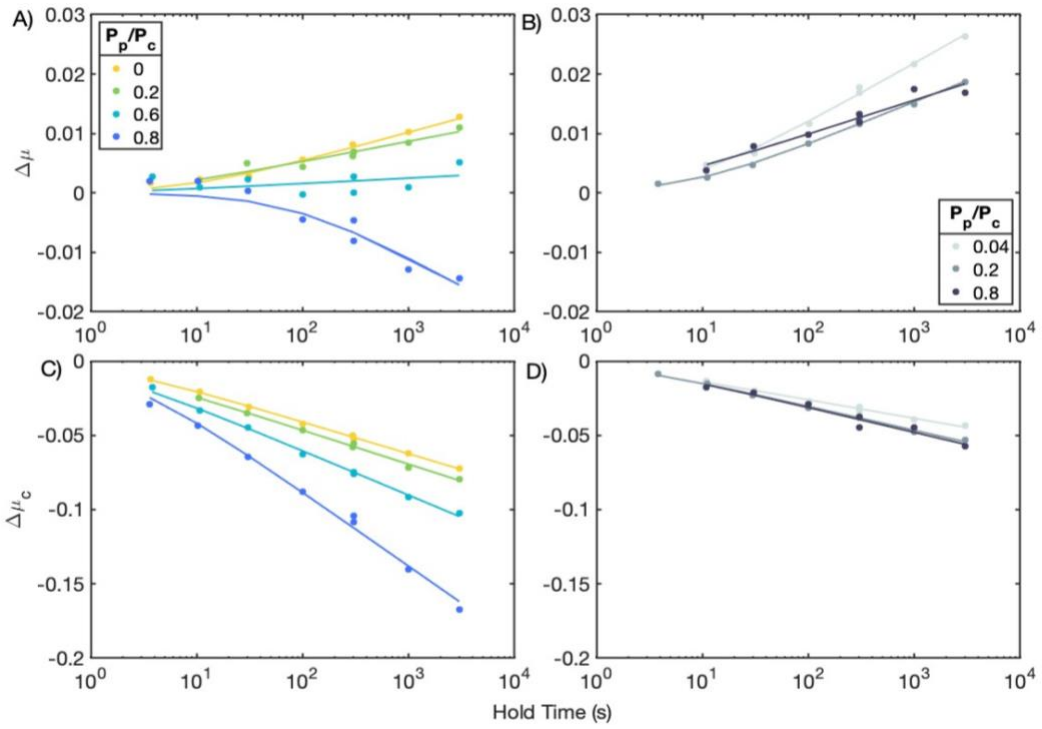

Figure 4: Healing **(A, B)** and relaxation **(C, D)** for the Arbuckle dolomite **(A/C)** and Troy granite **(B/D)**, with a suite of pore fluid pressure experiments on each lithology.

Figure 10: 2.5 Healing Rate, Cutoff Time, and Relaxation Rate

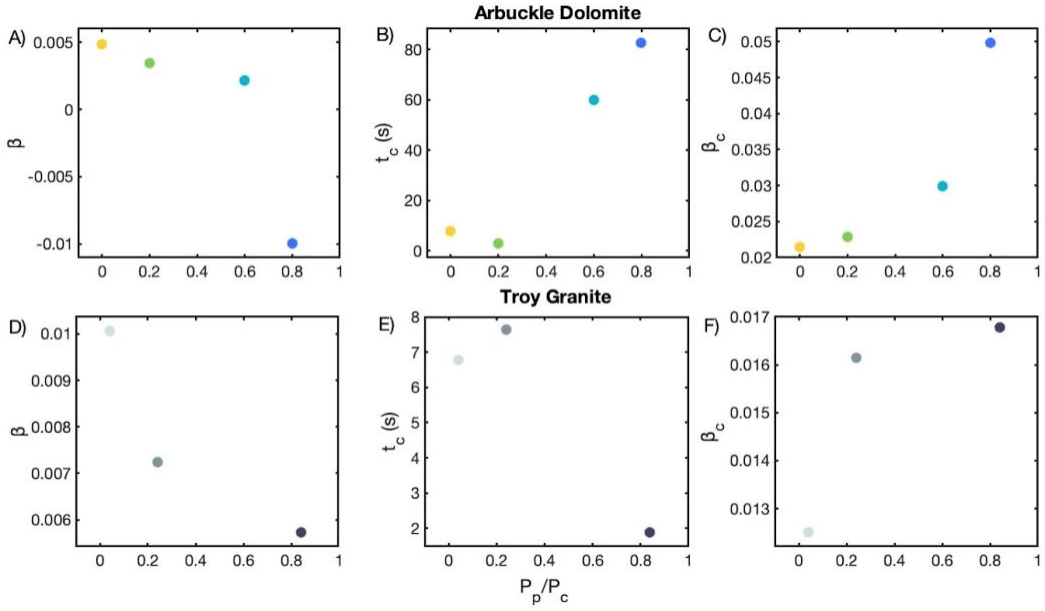

Figure 5: Healing rate **(A/D)**, cutoff time **(B/E)**, and relaxation rate **(C/F)** for the Arbuckle Dolomite **(A-C)** and the Troy granite **(D-F)** as a function of Pore Pressure/Confining Pressure.

We recorded both vertical sample displacement and sample compaction during holds using the on-board LVDTs (Figure 2). During a hold, sliding velocity decays and the total displacement is dependent on the pre-hold shear stress, where larger pre-hold shear stresses result in greater displacements (Figure 6A/B/C). Total sample displacement depends on the time of the hold as well (Figure 6B/C/D/F). For the Arbuckle dolomite, compaction occurs earliest in the hold for the high pore pressure experiment compared to the other pressure conditions (Figure 6E). This might be caused by either increased compaction from dissolution or decreased slip rate because of a smaller pre-hold shear stress. This experiment is clearly compacting at 100 seconds while the lower pore fluid pressure samples may not be, and the

velocity at this time is much slower. In a purely geometric sense, increased compaction should allow for increased healing because the more compacted the layer, the harder it is to dilate on the re-shear (Dieterich, 1972). However here we see that the most compacted sample has healed the least and this is likely because the mechanism that we hypothesize is responsible for compaction (dissolution) is causing weakening and not strengthening, unlike other studies. The time it takes to achieve measurable compaction in Figure 6E/G is longer than the time it takes to begin healing (the cutoff time) and suggests that either healing is occurring while velocity is relatively fast or that smaller than measurable compaction (~1 μm) is important. Note that for short holds, compaction data are noisy due to errors in picking the start and end of the hold.

For all of our experiments except for one, relaxation occurs elastically as evidenced by the shear stress versus displacement curves with the same slope (Figure 6A). At the highest pore fluid pressure for the Troy Granite, relaxation follows an elastic curve for the first ~1μm and then transitions to slipping more than expected at a given shear stress (Figure 6A/F). This behavior may indicate that the gouge is failing at this shear stress or switching mechanisms. For both the Arbuckle dolomite and the Troy granite, increase in relaxation with an increase in pore fluid pressure is accompanied by an increase in compaction (Figure 6C/G), although the highest pore pressure Troy granite experiment did not have recorded compaction data.

Figure 11: 2.6 Displacement and Compaction during Each Hold

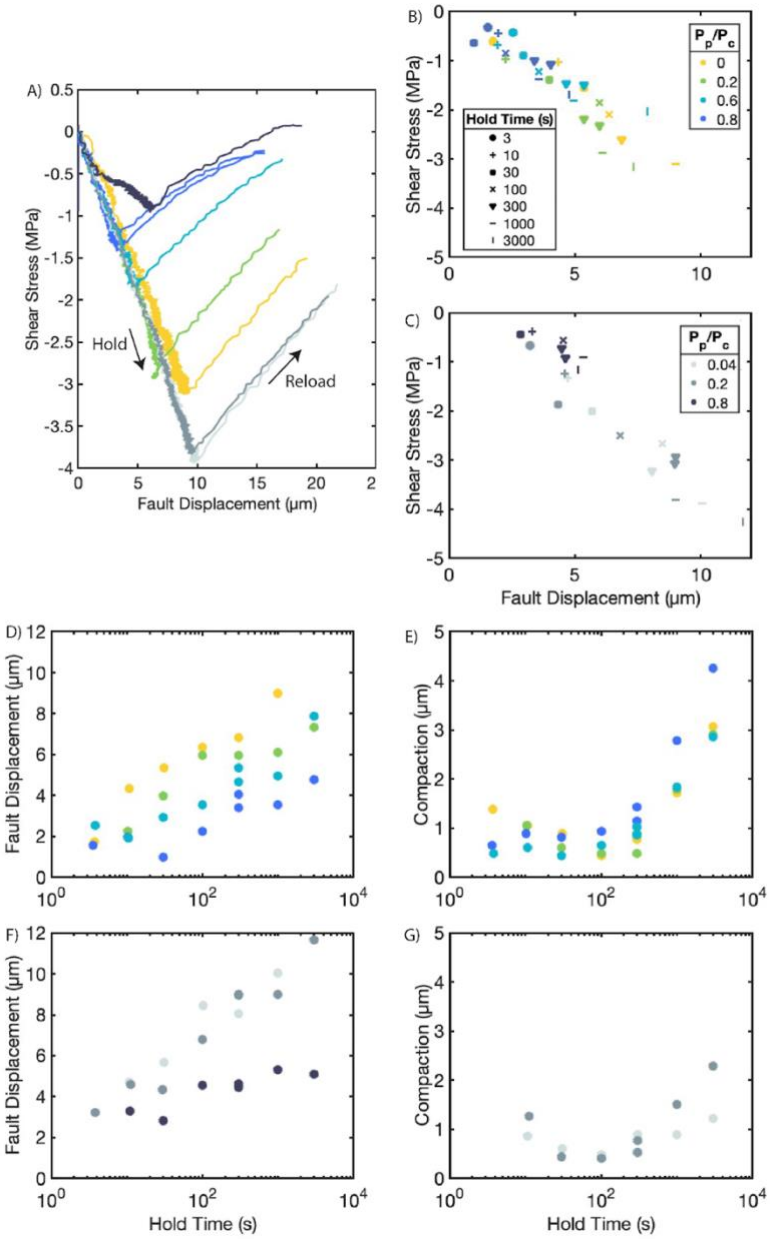

Figure 6: On-sample LVDT displacements for each experiment. Legend for the Arbuckle dolomite pressures is in B and legend for the Troy granite pressures is in C and is consistent for all plots. Legend with hold time indicates marker shapes for each hold time length for both lithologies. **A)** Shear stress versus fault displacement during a 1000s hold and the following reload period**. B)** Fault displacement versus shear stress at the end of each hold for each hold time for the Arbuckle dolomite experiments. **C)** Same as B for the Troy Granite. **D)** Fault displacement versus hold time for each experiment for the Arbuckle dolomite. Higher effective stress experiments have more displacement. **E)** Compaction versus hold time for each experiment for the Arbuckle dolomite. **F)** Same as D for the Troy granite. **G)** Same as E for the Troy Granite. High pore pressure compaction data are not present due to the radial LVDT falling out of position during the experiment.

In addition to slide-hold-slides, we performed rate-stepping tests to analyze the frictional stability of the gouge at various pore pressures. The largest difference in *a* and *b* occur from the change in pore pressure from ~0 to $P_p/P_c = 0.2$ (Figure 7A/B), where both decrease at this transition. At pore pressures near zero, both *a* and *b* are large and *a-b* is velocity neutral to possibly velocity weakening. Above pore pressures near zero, the change in *a* and *b* depends on lithology. For the Arbuckle dolomite, the rate parameter *a* increases with increasing pore fluid pressure and *b* increases slightly (Figure 7a/b). Therefore, the increase seen in *a-b* for the Arbuckle dolomite is mostly controlled by an increase in *a* for P_p/P_c =0.2 to 0.8. For the Troy Granite, *a* decreases with increasing pore fluid pressure and *b* remains relatively stable. With increasing pore fluid pressure, from $P_p/P_c = 0.2$ to 0.8, *a-b* for the Troy granite is slightly decreasing due to the decrease in a (Figure 7C)

For all experiments, normalized stiffness (K/σ_{eff}) increases with increasing pore fluid pressure, however non-normalized stiffness (Figure 7C/D) remains relatively constant except for the high pore fluid pressure Troy granite experiment. This is consistent with Figure 6A, where shear stress versus displacement (the stiffness of the hold) stays constant except for the high pore fluid pressure Troy granite experiment. The critical slip distance (D_c) increases with increasing pore fluid pressure from $P_p/P_c = 0.2$ and above, with slip law values being consistently higher than aging law values. This increase in the critical slip distance should further stabilize the fault as more energy must contribute to accelerating when D_c is larger (Ruina, 1983). The critical slip distance is dependent on the size of asperity contacts

and the localized shear zone width (Dieterich, 1979; Marone & Kilgore, 1993; Rabinowicz, 1956; Rathbun & Marone, 2013; Scholz, 1988), so this change in critical slip distance suggests that one or both of these attributes are changing with pore fluid pressure.

Figure 12: 2.7 Rate-State Parameters from Velocity Steps

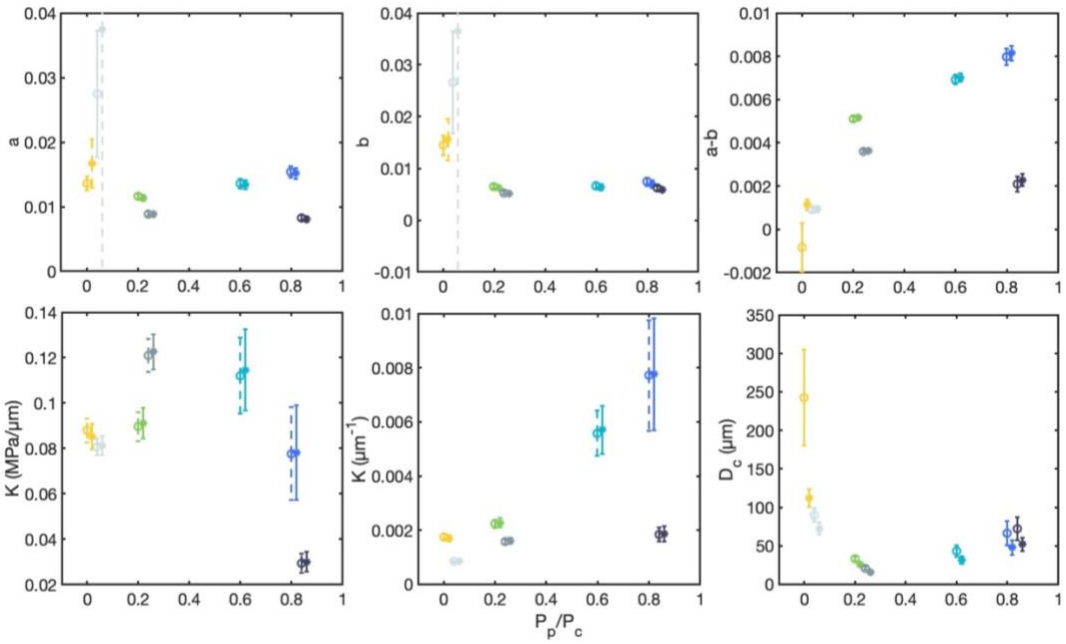

Figure 7: Rate-state parameters as well as stiffness for up-stepping rate-steps versus pore pressure. These parameters were inverted for using RSFit3000 and there errors are as reported by RSFit3000 (Skarbek & Savage, 2019). Colors are consistent with other figures, with pore pressure conditions presented on the x-axis. Circles show slip-law fits and stars indicate aging-law fits and are slightly offset for clarity.

We imaged the post-experiment microstructures of low pore pressure (10 MPa) experiment and a high pore pressure (40 MPa) experiment (Figure 8). The low pore pressure experiment has boundary shears both on the top and bottom of the sample that have grain size reduction, while the high pore pressure experiment includes riedel shears, but with no large areas of grain size reduction (Figure 8A/B).

The boundary shears of the low pore pressure experiment indicates that most of the deformation is occurring within these shear zones. The high pore pressure experiment shows that deformation is more distributed whether through the bulk of the gouge or through riedel shears. In general, the low pore pressure experiment also has narrow cracking occurring through grains (Figure 8C). The high pore pressure experiment lacks these narrow cracks, however there are areas of pervasive fracturing that look like the grain is being fractured apart into many smaller grains. Evidence of dissolution at asperity contacts might look like small indents into the edges of grains, which is subtle, but may increase the roughness of grains that exhibit increased dissolution. Grains with sharp roughness to them are noted in Figure 8C/D by light blue arrows and grains with pitting are noted by the dark blue arrows. Pitting is caused by etch-pit formation, which is expected when the fluid is far from saturation and if many crystal defects and impurities exist at a moderate saturation state (Adkins et al., 2021) (Figure 8E).

There are notable differences between the two samples in terms of the grain shape characteristics as measured by Imagej (Figure 9). We examined grain shape characteristics in order to quantify any differences in fracturing or dissolution between the two samples. For both experiments, we analyzed ~0.85mm by ~1.6mm images of the microstructures for computational efficiency. These images have a resolution of 67.45 nm/pixel, so we analyze grains with 100 pixels (6μm or larger in diameter). The grain size distributions are similar for both experiments. The lower pore pressure experiment has more large grains and more small grains, while the

higher pore pressure experiment has a subtle amount of more moderate sized grains. The number of grains in these are slightly different due to grain density as well as a small difference in image size. The solidity (area of the grain/area of the convex hull around the grain) is higher at all grain sizes for the low pore pressure experiment. The aspect ratio (major axis/minor axis) of the low pore pressure experiment is similar to the high pore pressure experiment when including small grain sizes. The low pore pressure experiment has grains with increased aspect ratio when only including large grain sizes. The circularity of the grains is larger at smaller grain sizes for both experiments, and circularity of the low pore pressure experiment is higher than the high pore pressure experiment when including grain sizes ~60 μm and below. This decrease in circularity with increasing grain size is likely caused by an increase in aspect ratio. Roundness is circularity corrected for aspect ratio and this shows that the low pore pressure case always has more round grains than the high pore pressure case except for the ~60μm and above bin.

Figure 13: 2.8 Microstructural Observations

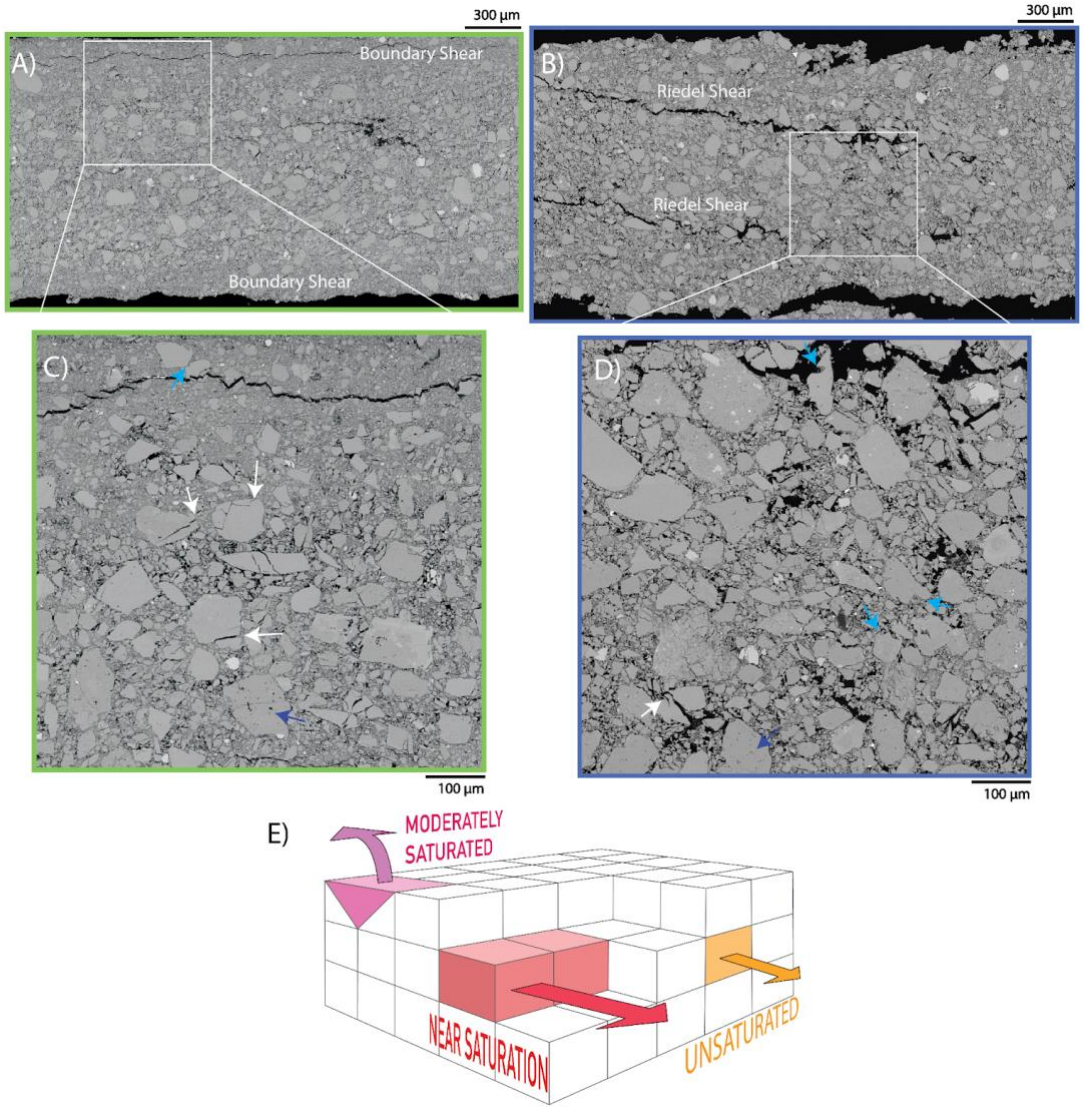

Figure 8: SEM images of post-experiment microstructures from a low pore pressure (10 MPa) experiment 55 (A/C) and a high pore pressure (40 MPa) experiment 57 (B/D). **A)** Experiment 55 has two boundary shears which exhibit grain size reduction. **B)** Experiment 57 has two possible reidel shear zones and does not have grain size reduction. **C**) A zoomed in portion of Figure A. Fracturing as noted by the white arrows is prevalent in the larger grains. Some evidence of dissolution, such as pitted grains (dark blue arrow) and indented, angular grains (light blue arrow). **D)** A zoomed in portion of Figure B. Evidence of dissolution as noted by grain angularity (light blue arrows) and pitted grains (dark blue arrow) is more ubiquitous by eye in this sample. Fracturing of larger grains is less common than in experiment 55. **E)** A

depiction of three different dissolution modes in a crystal lattice. Dissolution near saturation occurs only at pre-existing steps in the crystal lattice (red). Dissolution when the saturation state is moderate occurs via etch-pits at crystal lattice defects and impurities (pink). Dissolution far from equilibrium can occur via etch-pits anywhere along the crystal lattice (orange).

Figure 14 : 2.9 Quantitative Analysis of Microstructural Images

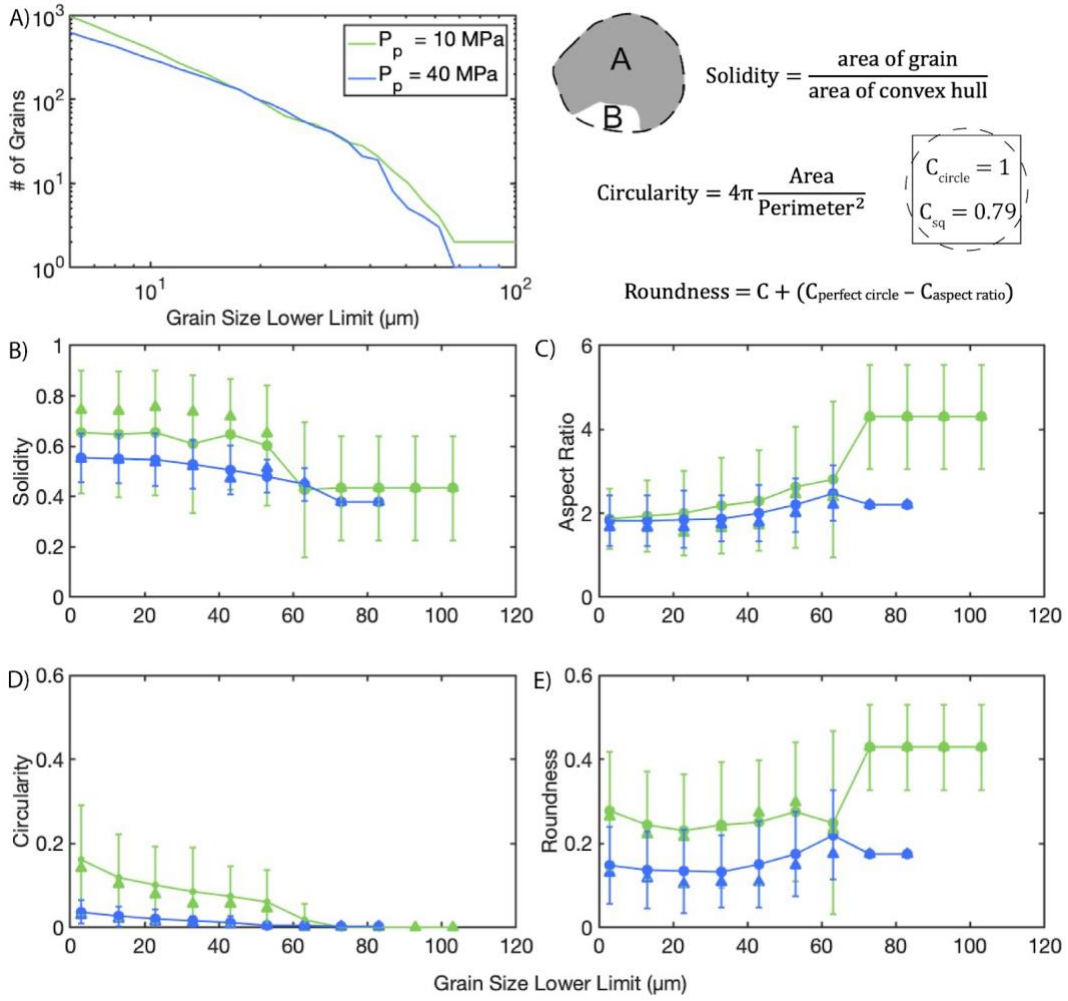

Figure 9: A comparison between grain characteristics of the low (10MPa) pore pressure sample, experiment 55 (green) and the high (40 MPa) pore pressure sample, experiment 57 (blue). For all characteristics, we analyze grains above 6 μm in order to have at least 100 pixels per grain. This ensures that pixelization does not interfere with any grain shape metric. A) The grain size distribution for each experiment. B/C/D/E) Solidity, aspect ratio, circularity, and roundness as a function of the lower limit of the grain size. Circles indicate the mean value, triangles indicate the median,

and error bars are calculated from the standard deviation of all grain sizes within the bin. Solidity is higher when grains are less angular. The aspect ratio is higher when grains are elongated. Circularity is higher when grains are closer to a perfect circle. Elongated grain as well as angular grains will decrease circularity. Roundness is calculated as the circularity of the grain corrected for the aspect ratio, such that roundness only decreases due to increasing angularity and not elongation (Takashimizu & Iiyoshi, 2016).

5. Discussion

5.1 Frictional Velocity Dependence

For all experiments with pore fluid pressure, the gouge exhibited velocity-strengthening behavior (Figure 7). For the Arbuckle dolomite, an increase in *a* is the cause of the increase in *a*-*b*. Both an increase in *a* and a decrease in *b* should affect the healing rate given the effect of *a* on relaxation during the hold and the effect of *b* on healing when velocity is close to zero for the aging law. Some studies show a relationship between *b* and healing rate (β) that we do not see here (Ikari et al., 2016), which we do not see here for the Dolomite experiments. This suggests dolomite is less well-predicted by the aging law for slide-hold-slides than other materials. The rate-state stability parameter is consistent with another study that found *a*-*b* is velocity neutral to strengthening for a calcite vein from Oklahoma from ~1 to 3 km depth and that Troy granite is velocity neutral to strengthening from ~1 to 4 km when using a hydrostatic pore pressure gradient and a geotherm appropriate for Oklahoma. Below 4 km depth, Troy granite gradually exhibits velocity-weakening behavior with increases in depth (Kolawole et al., 2019). These experiments were done at temperatures of 23°C/km, and this temperature gradient did not significantly alter their results compared to our experiments done at room temperature. The increase in

a-b with increasing pore pressure seen in our Arbuckle dolomite results is inconsistent with other studies on effective stress in carbonates (Carpenter et al., 2016a). It is also inconsistent with decreasing stability of carbonate faults with increasing pore pressure has also been documented (Scuderi & Collettini, 2016). It is possible that the microphysical deformation mechanisms in the dolomite here are different from those from the limestone and marble used in the Scuderi & Collettini (2016) and Carpenter et al. (2016a) and/or that pore fluid chemistry could be affecting the mechanical response. Pore fluid chemistry will be discussed in the following sections.

For all pore fluid pressures greater than 0, we observe an increase in the critical slip distance, D_c, with increasing pore fluid pressure (Figure 7F). This increase in D_c is larger than, but consistent with, a similar study on Nankai trough sediments (Bedford et al., 2021). An increase of D_c is consistent with an increase in the width of the localized shear zone viewed in the our microstructures (Figure 8) as well as an increase in dilation related to movement of larger grain sizes in the shear deformation zone of the high pore pressure experiments (Figure 8/9). Less localized deformation at high pore fluid pressures has been previously documented in high pore pressure experiments (Xing et al., 2019), as has increased localized deformation with smaller grain sizes and higher effective normal stress (Bedford & Faulkner, 2021).

5.2 Healing at Low Fluid Pressure

The frictional healing of Arbuckle dolomite at low pore fluid pressures shows typical Dieterich-type healing, where steady-state friction is the same before and after the hold and healing increases with log time once the cut off time has passed (equation 1). The healing rate of 0.005 s^{-1} is slightly lower than most other carbonate studies. Other studies find healing rates of 0.01-0.02 s^{-1} (Carpenter et al., 2016a; Carpenter et al., 2016b; Carpenter et al., 2014), however these studies were primarily conducted on calcite. In addition, they used a double-direct shear either in a biaxial setup or true triaxial setup, which likely changes the shear relaxation of the holds and the subsequent healing behavior, as well as water saturated with carbonate ions. A previous experiment on a sample of mostly (96%) calcite and dolomite with minor amounts of clay and quartz (listed as breccia-derived sample) at room temperature found healing of ~0.01 s^{-1} for fairly similar effective stress conditions (P_c = 60 MPa) and pore fluid pressure (P_p = 15 MPa). The experimental setup is nearly identical to ours and deionized water was used as a pore fluid (Chen et al., 2015), however our sample is almost entirely dolomite, suggesting that calcite and dolomite have different healing behavior at these conditions. The effects of pore fluid chemistry on healing will be discussed in section 5.4. The Troy granite at low pore fluid pressure exhibits a typical healing behavior for room temperature granite gouge of ~0.01 s^{-1} (Bedford et al., 2023; Beeler et al., 1994; Carpenter et al., 2016b).

5.3 Weakening at High Pore Fluid Pressure

As fluid pressures increase, the healing rate of the Arbuckle dolomite decreases. At pore fluid pressures of 30 and 40 MPa (P_p/P_c = 0.6 and 0.8), the Arbuckle dolomite exhibits a new behavior. This behavior is indicated by a small peak in friction, which is prominent during the re-slide. Friction after this small peak then drops and gradually increases back to either the previous steady state or to a weaker steady-state. An example is that during the 3000s hold, steady-state friction never fully recovers to the previous steady state and instead decreases by ~0.008 (Figure 10C). This indicates that the hold permanently altered the grains in a manner that changed the following steady-state, which is seen in other studies (Chen et al., 2015).

There is a question of whether pore fluid pressure itself could cause the weakening seen in the Arbuckle dolomite. In the same manner as dilatant hardening, the pore fluid pressure in the gouge might increase during the hold without being able to escape, such that the strength of the gouge on the re-slide is apparently lower due to an unmeasured increase in pore fluid pressure. Then on the re-slide, pore pressure within the gouge slowly equilibrates back to the system level as porous pathways re-open to the system and the gouge strengthens (e.g. Hirakawa & Ma, 2016; Sleep & Blanpied, 1992). There are multiple issues with this idea for our data. First, at high pore pressures the gouge is the most permeable with the least comminution. Second, the gouge should always return to the measured pore fluid displacement in this case if there is no change to the gouge, which it does not at long holds (Figure 10A). In

addition, weakening due to the hold is clearly not seen in the Troy granite even though the pore fluid pressure system is the same (Figure 10D). There is a clear increase in friction for the Arbuckle experiment after dilation is presumably over, which suggests this increase in friction is due to something other than pore fluid pressure. This may be caused by the dissolved grain shape allowing for weaker behavior until a considerable amount of displacement (~200 μm) past typical D_c values (<100μm). Dissolution of the Arbuckle as a mechanism of weakening is discussed in the following section 5.4.

The high pore pressure Troy granite experiment has a slightly lower healing rate, but it also clearly has some other behavior that differentiates it from our other experiments. Most notably, it does not follow the same shear stress versus fault displacement stiffness that all other experiments follow (Figure 6). This behavior could be viscoelastic and/or anelastic or be caused by a different deformation mechanism occurring in the grains after some relaxation. In addition, the cutoff time is clearly smaller for this experiment (Figure 4/5). Most of the shear stress relaxation is done in the initial few seconds and then shear stress remains the same. This causes a lot of healing to happen in the first few seconds, whereas afterwards, healing is slower than the lower pore pressure experiments. Post-hold, steady-state friction evolves over a longer displacement period than what D_c would suggest, similar to the Arbuckle experiment. Again, this is unrelated to dilation given that the pore fluid intensifier displacement shows displacement over a much shorter distance (Figure 10B/D). This may suggest that viscoelastic deformation is still recovering. This

experiment also shows an offset in pore pressure 2 displacement that suggests the gouge porosity was permanently altered due to the hold and steady-state friction is also altered following the hold (Figure 10B/D). These effects should be further investigated.

Figure 15: 2.10 Pore Fluid Volume During and Post-Hold

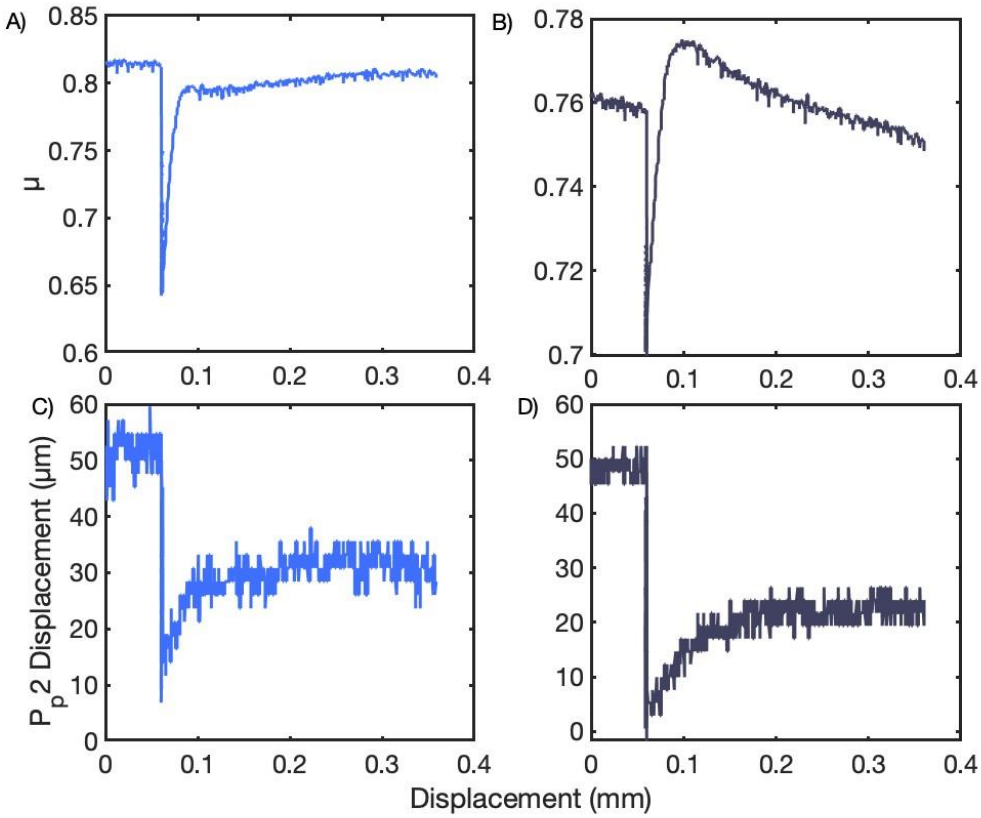

Figure 10: Friction versus loading displacement **(A/B)** and pore fluid pressure displacement in the upstream intensifier versus loading displacement for a 3000s hold **(C/D).** This is shown for both the high pore pressure (40 MPa) Arbuckle dolomite **(A/C)** and the high pore pressure (80 MPa) Troy granite **(B/D)**.

5.4 Dissolution of the Arbuckle

From both our experiment and microstructural data, dissolution of the dolomite gouge is a likely mechanism of weakening. The dissolution of carbonate during pressure solution is dependent on the amount of water, the total surface area of the particles, the dissolution rate and the solubility of the water (Raj, 1982). The solubility of carbonate is pressure and temperature dependent, where increases in pressure causes an increase in solubility and increases in temperature cause a decrease in solubility. Dissolution rate depends on the saturation state as depicted in Figure 8E (Adkins et al., 2021), on grain structure (den Ende et al., 2019; van Noort & Spiers, 2008) and the presence of air (Yokoyama & Nishiyama, 2020). Dissolution/precipitation behavior will also depend on the presence of other mineral quantities (Chen et al., 2015; Renard et al., 2012, Zhang & Spiers, 2005).

Previous work finds that healing of carbonate is typically rapid for fluid saturated conditions when pore water is equilibrated to the calcium carbonate system (Carpenter et al., 2016a; Carpenter et al., 2016b; Tesei et al., 2014). In experiments that use deionized water, healing increases and compaction during the hold decreases with increasing temperature, suggesting that dissolution is not as ubiquitous at higher temperatures (Chen et al., 2015). This is contrary to typical pressure solution flow laws, but is consistent with solubility decreasing with increasing temperature. Thus, rapid healing may actually indicate either that precipitation is promoted or that other processes, such as other plastic deformation mechanisms at contacts or granular processes, control healing. A lack of pressure solution in carbonate at saturated

conditions has been suggested as well (French et al., 2022; Lisabeth & Zhu, 2015), however other studies indicate pressure solution is more dominant at saturated conditions than non-reactive cases (Zhang & Spiers, 2005). Both of these possibilities are likely true at different conditions, given enhanced solubility of both unsaturated and saturated pore fluid with pressure, but, also, pressure solution should not occur in truly non-reactive cases.

In general, the weakening observed in our experiments suggests that dissolution is occurring and precipitation is minimized. The exact kinetics of how dissolution occurs is not well documented, so it is hard to then link this to a weakening effect. Two possible mechanisms that would allow for dissolution to contribute to weakening is 1) a decrease in contact area over time and 2) a change in the thickness or chemical components of the interstitial layer over the hold time. One study using atomic force microscopy (AFM) experiments found a measurable decrease in the frictional strength of a calcite crystal during pressure solution, which they attribute to dissolution changing the chemistry of the interstitial layer and making it a better lubricant (Fu et al., 2021). Another AFM study tested a series of dry tests vs water saturated tests and found that dissolution could explain the velocity dependence of friction for the water-saturated tests, which had the lowest frictional strength at the slowest sliding velocities and therefore exhibited velocity-strengthening at slow velocities. In contrast, in the dry case, friction was velocity weakening at slow velocities and they attribute this to the strengthening of the contact at low velocities from atomic attrition (Fu et al., 2022). In addition, without

understanding the kinetics, it is also not clear why the higher effective stresses are also not predominantly affected by dissolution. A few possibilities are: 1) dissolution is less common in more localized shear zones that occur in the high effective stress experiment than it is in the bulk of the gouge due to less available unsaturated water, 2) at increased contact pressure, the thickness of the interstitial layer is smaller, and 3) that the strain rate of the high pore fluid pressure experiment is slower and allows for more time-dependent contact for dissolution to occur. Explanation 3, which dictates that strain rate is the main control on dissolution suggests that at long timescales, dissolution could occur even in the high effective stress/ low pore pressure case.

Determining the underlying chemical reasoning for dissolution through an experimental suite is clearly necessary to understand how ubiquitous this process is during injection related activities and to properly extrapolate these results to larger spatial and temporal scales. It is particularly imperative given that the pore fluid pressures to cause weakening in this study are not typically modeled in Oklahoma (Keranen & Weingarten, 2018; Keranen et al., 2014), however dissolution could be enhanced even at lower fluid pressures if differences in slip velocity, pore fluid chemistry, wall-rock permeability, and the mineral constituents of the fault gouge, are important. It also should be noted that pore fluid pressure at short timescales is not well-known.

5.5 Implications

This study found that an increase of pore fluid pressure in the Arbuckle group can cause weakening of fault gouge. The mechanism for this weakening is likely dissolution due to unsaturated pore fluid. The implications of this are 1) that fault gouge can weaken with hold time, which has not been previously emphasized and 2) that this weakening could cause enhanced stable slip of a region. Clearly, waste-water injection into the Arbuckle group is not always saturated with respect to carbonate ions and components of injected wastewater that, such as salt and CO_2, could contribute to enhanced weakening by increasing pore fluid solubility. Therefore, fluid injection might weaken faults in the Arbuckle group both through the classic effective pressure law (Terzaghi, 1936) as well as through dissolution of contacts. Overall, pore fluid pressure promotes stable failure of the Arbuckle, which may contribute to loading the basement faults below. Our companion paper outlines an observation of repeating earthquakes that suggests the Arbuckle group has reduced strengthening likely because of this dissolution mechanism (Okamoto et al.). Overall, this suggests that slip in the Arbuckle group plays a key role in induced seismicity in Oklahoma and throughout the midcontinent of the United States. In addition, induced earthquakes nucleated at the edge of fossil carbonate reefs in Alberta, Canada even with low injection rates (Schultz et al., 2016) and induced events occurred below the Ordovician carbonate in Fort Worth Basin, Texas (Hornbach et al., 2016; Magnani et al., 2017). In North Dakota, injection occurs into the sandstones of the Dakota formation, which is very permeable, but lacks seismicity (Frohlich, 2012), possibly

due to the absence of pathways to the basement carbonate (Keranen & Weingarten, 2018) or due to the absence of carbonate sequences. Overall, this study finds that injection into carbonate sequences is ill-advised due to the possibility of enhanced weakening through dissolution.

Tectonic regions likely have pore fluid in equilibrium with the surrounding rocks, however in regions of mixed lithology, infiltration of pore fluid out of equilibrium could occur. A few studies have invoked increased dissolution due to infiltration of CO_2-rich fluids as a weakening mechanism that contributes to intraplate earthquake swarms (Heinicke et al., 2009; Vavryčuk & Hrubcová, 2017) and slip on low-angle normal faults (Collettini & Holdsworth, 2004).

6. Conclusions

We measured the frictional velocity dependence through velocity stepping tests and healing behavior through slide-hold-slide tests of relevant Oklahoma lithologies. Specifically, these lithologies are the Arbuckle formation, which is mostly composed of dolomite, and the Troy granite, a component of the basement granitic rocks. We find that pore fluid pressure promotes stable behavior of both the dolomite and granite. Significantly, the Arbuckle dolomite weakens with hold time at the highest pore fluid pressure analyzed. The Troy granite heals at all pore fluid pressure at rates ~ 0.01 s^{-1} consistent with other, relatively low pore fluid pressure, studies of granite. The Troy granite exhibits an interesting, possibly viscoelastic behavior during stress relaxation of the slide-hold-slides at the highest pore fluid pressure that should

be further investigated. Microstructural analysis suggests that high pore fluid pressures promote less localized deformation, which can promote stability, and less rounded grains, which we interpret as evidence of dissolution. These healing rates are used in our companion paper to explain the moment-recurrence time behavior of repeating earthquakes (Okamoto et al.,). Combined, these results suggest that dissolution of the Arbuckle group is occurring due to wastewater injection and this has important implications for injection into carbonate formations. Further work is needed to elucidate the kinetics of dissolution in order to scale this work to larger spatial and temporal scales.

Chapter 3 To heal or not to heal? Part II: The moment-recurrence time behavior of repeating earthquakes in the 2011 Prague, Oklahoma aftershock sequence is consistent with laboratory healing rates

Abstract

The competition between fault healing (i.e., re-strengthening) and fault loading determine the seismic cycle. Repeating earthquakes can give observational estimates of fault healing rates, however, it is difficult to link laboratory studies of frictional healing and observed healing rates from repeating earthquakes in part because of uncertainty in lithology. Here, we study the 2011 Prague earthquake sequence, which includes repeating earthquakes located in the Arbuckle group and the granitic basement. We find three spatially distinct groups of repeating earthquakes that suggest different healing behaviors. These three behaviors include 1) stagnant healing in the Arbuckle group, 2) chaotic healing/loading at the intersection of the foreshock-mainshock fault, and 3) typical log-time dependent healing behavior outside of the foreshock-mainshock fault intersection. We use the laboratory results of our companion paper (Okamoto et al, submitted) to explain the healing behavior of the repeating earthquake families.

1. Introduction

Tectonic loading and fault healing (i.e. restrengthening after earthquake slip) are the two competing components of the seismic cycle. Constraints on tectonic loading can be made through geodetic methods, however there are rarely constraints

on fault healing. Repeating earthquakes are earthquakes with such similar waveforms that they may represent the same fault patch failing multiple times, which is commonly interpreted as evidence of aseismic slip or pore fluid pressure changes. A few studies have analyzed repeating earthquakes in terms of healing, which is indicated by an increase in stress drop with recurrence time (Chaves et al., 2020; Kanamori & Allen, 1986; Marone, 1998), however only Marone (1998) has been able to tie these rates to laboratory healing behavior. Linking laboratory rates of healing to seismic estimates is difficult due to uncertainty in stress drops for small repeating events and uncertainty in lithology at depth for tectonic regions. Lithology in particular is a key control on fault healing in laboratory studies (Carpenter, Ikari, et al., 2016; Shreedharan et al., 2022).

Laboratory healing has been predominantly studied through slide-hold-slide tests at μm/s shearing velocities. Laboratory healing depends on lithology, pressure, temperature, and sliding velocity (Carpenter et al., 2016b; Chen et al., 2015; Jeppson et al., 2023; Marone & Saffer, 2015; Ryan et al., 2018). An increase in loading rate is thought to decrease the time it takes to start healing (the cutoff time) regardless of lithology. This cutoff time was used to explain a 100-day delay in healing by Marone (1998), who modeled this delay in healing using a slide-hold-slide 1D slider-block model through a combination of afterslip in the repeating area due to the previous event and a slow reloading rate. This slow reloading rate is the initial slip velocity of the repeating earthquake and is therefore the slip rate at the beginning of nucleation. In addition to these observations from μm/s sliding velocities, rapid fault healing is

expected to occur after an earthquake due to temperature rise during earthquake slip velocities (Savage et al., 2019) and this has been recently measured in the lab through m/s sliding velocity experiments (Bedford et al., 2023). In the lab experiments, rapid healing occurred for ~10 seconds, however with realistic pressures and wall-rock diffusivities, this healing could last for seconds to minutes and more constraints on this are needed for different lithologies (Savage et al., 2019). This high temperature phenomena should be captured by measurements of fault healing from repeating earthquakes as well. Combined, these laboratory measurements present three stages of fault healing following an earthquake: 1) rapid healing due to temperature rise over seconds to minutes, 2) a delay in healing due to afterslip over seconds to months, and 3) typical laboratory healing rates where friction increases over log time, which is also referred to as Dieterich-type healing (Figure 1).

Figure 16: 3.1 Expectations of Fault Healing from Laboratory Experiments

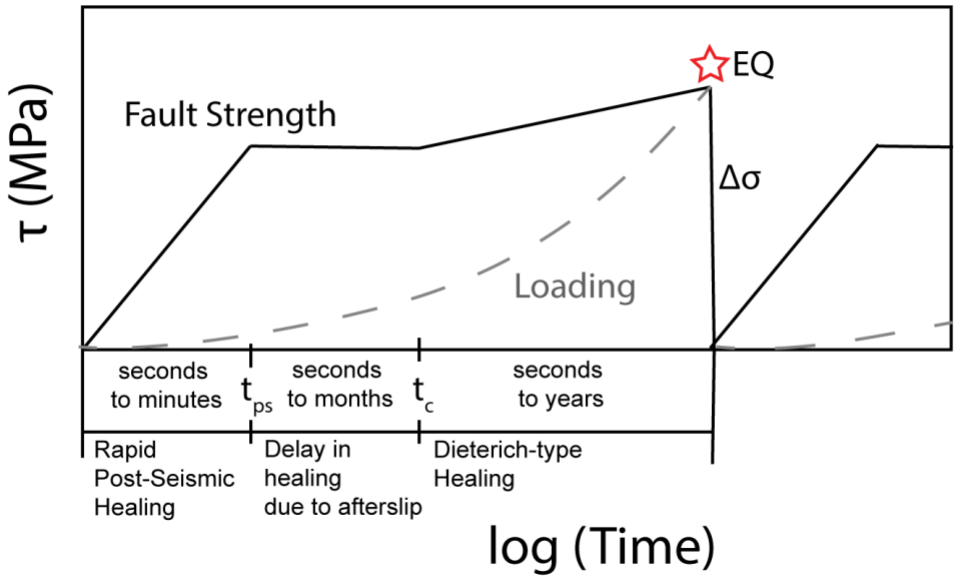

Figure 1: Expectations from laboratory experiments on fault healing. Fault strength increases due to a period of rapid healing that lasts until t_{ps}, then plateaus due to afterslip until the cutoff time (t_c), and then proceeds to heal via typical slow laboratory healing. An earthquake occurs when fault loading equals fault strength and stress drop is shown to be a complete stress drop. Note that loading is linear in time, but nonlinear in log(time).

In contrast to active tectonic regions, lithology at depth is well known in Oklahoma due to extensive well logs (Keranen et al., 2013). Here, we analyze the moment-recurrence time behavior of repeating earthquakes during the 2011 Prague, Oklahoma aftershock sequence, which included a M_w 5 foreshock, a M_w 5.7 mainshock, and a M_w 5 aftershock. Each of these events occurred on separate, intersecting fault planes. These earthquakes were caused by wastewater injection at the northern edge of the foreshock fault, which filled the porous reservoir below (Keranen et al., 2013; Figure 1). Repeating earthquakes within the aftershock

sequence occur both in the Arbuckle group and the granitic basement (Okamoto et al., 2022; Savage et al., 2017) (Figure 2). The Arbuckle group is composed of carbonate, which is largely dolomite or dolomitized limestone (Derby et al., 1991). In our companion paper, we measured laboratory healing rates at slow (μm/s) sliding velocities for both the Arbuckle group and the Troy granite (a component of the basement granitic rock) and found remarkably different healing behavior at elevated pore fluid pressure. The occurrence of repeating earthquakes in these different lithologies allows us to test whether there are seismologically measurable differences in fault healing based on lithology and whether these differences are reflected in our laboratory results.

2. Background

In laboratory studies, the cutoff time depends on α, a constant that depends on the stiffness of the machine stiffness, the rate-state parameter D_c and the steady state sliding velocity V_{ss}:

$$t_c = \alpha(D_c/V_{ss}) \quad (6)$$

Here, faster velocity equates to shorter contact times and therefore a more rapid onset of healing (Im et al., 2017). The loading dependence can be thought of as how the state parameter is shorter at faster velocities and therefore will evolve quicker during the hold when the pre-hold sliding velocity is faster (Nakatani & Scholz, 2006). The cutoff time is typically less than ten seconds as measured by typical ~μm/s laboratory velocities, but can be as long as 1000 seconds in hydrothermal experiments, and

decreases with increasing slip velocity as stated above (Marone, 1998; Nakatani & Scholz, 2004; Im et al., 2017; Jeppson et al., 2023). We note that for laboratory studies, sliding velocity before the hold and after the hold are always the same and therefore differences in changing just the pre-hold or just the post-hold sliding velocity have not been analyzed.

How the cutoff time scales from the laboratory to the seismic scale is an open question. By modeling a series of slide-hold-slides, the cutoff time was invoked as an explanation of the 100-day delay in fault healing found in the Calaveras repeating earthquakes (Marone, 1998). The model assumed a 1m/s rupture velocity, a 1 nm/s reload velocity, and a D_c from the width of the principal slip zone in field scale observations (5 mm). The fault was modeled with a slider-block system with rate-state frictional properties and a stiffness equal to the shear modulus over the rupture length (Marone, 1998). A different extrapolation, but with the same form as equation 5, was argued to explain repeating earthquakes on the San Andreas, Sargent, and Calaveras faults where D_c is estimated by the seismological critical slip distance (m scale), V_{ss} is assumed to be the plate-rate velocity, and the α term was not considered, so no stiffness effects were taken into account (Ikari et al., 2020). In either case, the velocity required for a long-time scale cutoff time is the reload velocity because within the rate-state framework, a very large delay in healing only occurs if the reload velocity is sufficiently slow compared to the initial velocity. The exact timing also depends on the evolution law chosen and the stiffness of the system. All of these

factors could be incorporated into the α term in order to bridge between the laboratory and earthquake scale, however this requires further work.

Figure 17: 3.2 Prague, Oklahoma Earthquake Sequence

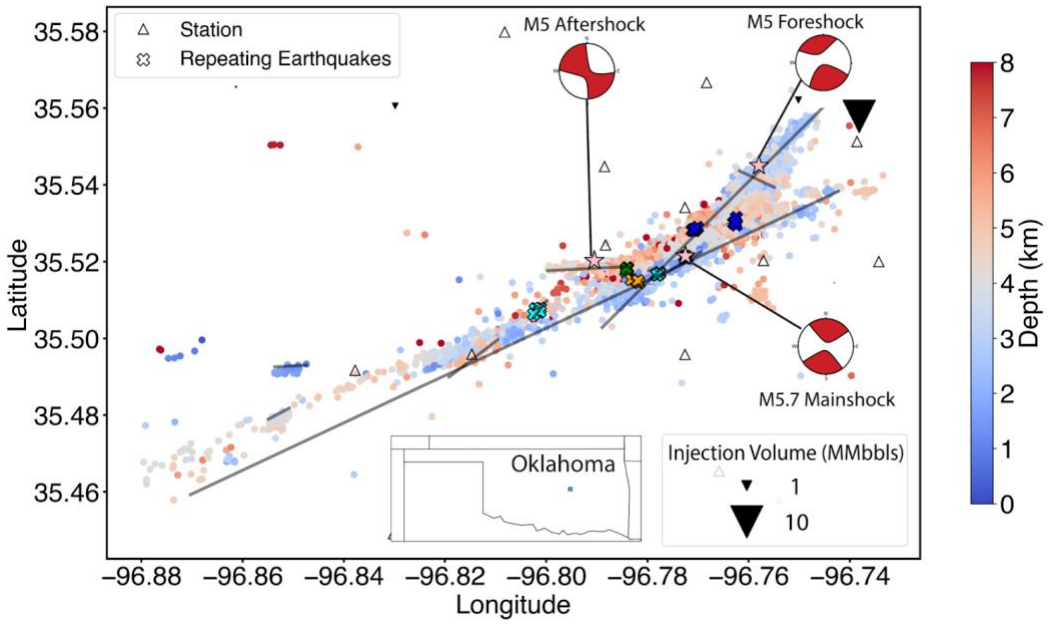

Figure 2: Map of the 2011 Prague, Oklahoma aftershock sequence with earthquakes colored by depth (catalog from Cochran et al. (2020)). The focal mechanisms of the three largest events are included (Ekström et al., 2012). Fault traces from (Skoumal et al., 2019) are in grey lines, repeating earthquakes are shown as x's and colored by group according to Okamoto et al. (2022), seismic stations are indicated by triangles, wastewater injection sites are upside down triangles that scale by the cumulative injection volume from 2006-October 2011 (data from https://oklahoma.gov/occ/divisions/oil-gas/oil-gas-data.html), and the largest three earthquakes are indicated by stars with their focal mechanisms (Ekström et al., 2012). Injection volume is reported in millions of barrels (MMbbls).

3. Methods

We analyze the healing behavior of repeating earthquakes in Prague, Oklahoma found by Okamoto et al. (2022). The repeating earthquakes were defined

as those that had a 0.95 cross correlation value on all 3 components for waveforms band-passed between 1-25 Hz. Here, we constrain our analysis to the seven repeating earthquake families that consist of three or more events. We calculate moment and stress drop in the time domain by manually measuring the source duration from the p-pulse width (Figure 2) (Frankel & Kanamori, 1983). The instrument response is deconvolved from each seismogram and velocity is converted to displacement using the remove_response function from the obspy python module (Beyreuther et al., 2010). A pre-filter at four frequencies: 0.7, 0.9, 100, and 120 Hz, is applied prior to deconvolving. Moment is calculated from the integral of the p-wave displacement pulse:

$$M_0 = 4\pi\rho c^3 R\Omega_o / U_{\Phi\theta} \quad (1)$$

where ρ is the density of the elastic medium, c is the wave speed, R is the distance from source to receiver, Ω_o is equal to the definite integral of the displacement pulse from the start of the p-wave to the end of the p-wave, and $U_{\Phi\theta}$ is a radiation pattern term (Kanamori & Brodsky, 2004). Moment without a radiation term correction is first calculated and averaged over all stations and then a radiation correction term of 0.52 is used (Shearer, 2009). Stress drop depends on the moment and the source radius. Here, we calculate stress drop assuming a circular rupture with a source radius, r (Eshelby, 1957),

$$\Delta\sigma = \frac{7}{16r^3} M_0 \quad (2)$$

The maximum possible source radius is calculated from the p-pulse width, which we call t_{dmax} because it is the maximum possible source duration. The maximum possible source radius, r_{max}, is:

$$r_{max} = 0.32 t_{dmax} c_s \quad (3)$$

where c_s is the shear wave speed (Brune, 1970). Here, we use a constant shear wave speed of 3 km/s. Although rupture velocity likely increases with depth due to the shear wave velocity increasing (Marty et al., 2019; Shearer et al., 2006), here we are looking at trends within each repeating earthquake family such that varying rupture velocity would only scale the rupture radius, and therefore depth dependence of rupture velocity can be ignored. We calculate stress drop from this maximum source radius as well as an a range of lower radius values down to a radius of 5 meters.

Source duration is typically measured in the frequency domain, either from the corner frequency or spectral ratio, due to computational automation and efficiency, and the ability to correct for attenuation. This allows for the computation of stress drop for a majority of earthquakes within a catalog and the exploration of spatial or temporal trends (Abercrombie et al., 2021; Pennington et al., 2021; Trugman, 2020). However, there are inherent disadvantages to using corner frequency that include having to choose a time window over which to compute the spectra and the inherent tradeoff between corner frequency and attenuation of the fit (Abercrombie, 2021). There are also inherent biases between different methods in computing stress drop from spectral estimates (Pennington et al. ,2021). In addition, spectral ratio estimates for a small number of stations do not perform better than

single spectra when <20 stations are used, likely due to differences in the path between the earthquake and the empirical green's function event (Kemna et al., 2020). For the Prague waveforms, the p-wave train is commonly disturbed by an s-p transition caused by the basement-sediment interface, which limits the time window over which to compute the spectra. Due to the small number of earthquakes we are analyzing here, the pulse width is a robust measurement of the maximum possible source duration (Frankel & Kanamori, 1983; Harrington & Brodsky, 2009).

Figure 18: 3.3 P-wave Pulses of Repeating Families at Station LC01

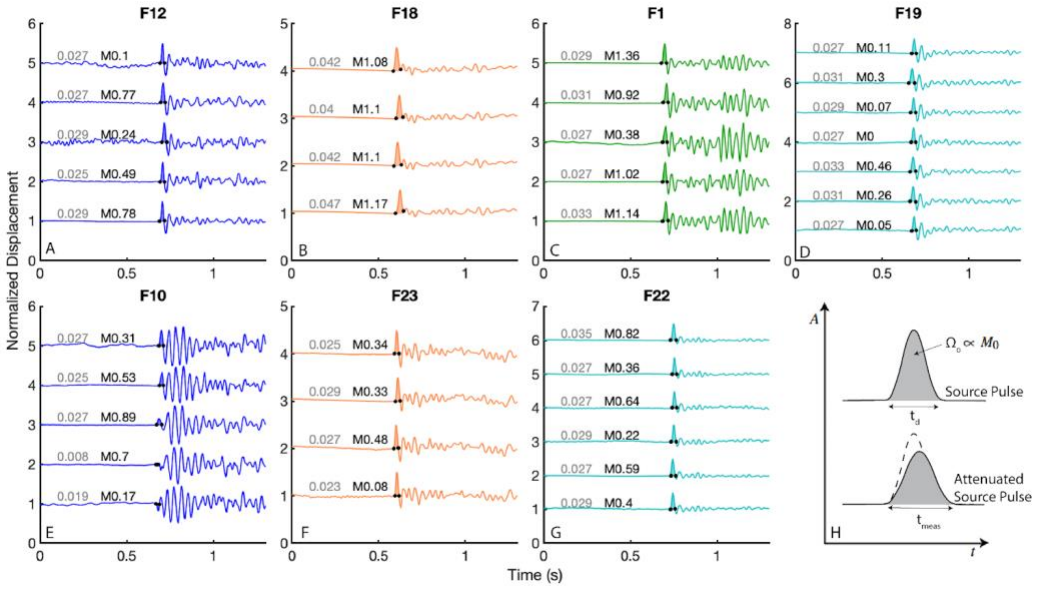

Figure 3: A-G) Seismograms with normalized displacement for all families at station LC01. The family numbers are listed as titles for each subfigure (F#). Black dots indicate picks for the start and end of the p-pulse, the p-pulse width is shown in grey on the left, and the magnitude is listed in black directly prior to the p-pulse. The area under the p-pulse is shaded to show how moment was calculated. Note that an additional 5 stations were used when possible to calculate the average p-pulse width and moment corrected for the radiation pattern. H) An idealized displacement p-wave pulse showing the area under the curve (Ω_o) and source duration (t_d) as well as an attenuated p-wave pulse. The attenuated pulse has the same area, but the measured

source duration is longer (t_{meas}). These measurements are then input into equations (1) and (3) to measure moment and source radius.

4. Results

4.1 Moment-recurrence time behavior

As we discussed in the methods, for our dataset, the source duration may be altered by attenuation of the p-pulse that is constant for all events. In other words, the pulse width or corner frequency could be a product of the path instead of the source, as long as the path effects remain unchanged between each event. Therefore, we first investigate how moment varies with recurrence time because moment is a robust observation of the source, whereas stress drop depends on measuring source duration accurately. This will give some insight into healing behavior through the seismic cycle before interpreting stress drop.

We find that the three spatially distinct groups of repeaters identified in Okamoto et al. (2022) have different moment-recurrence behaviors. The families hosted in sedimentary rocks (families 18 and 23) have moments that do not vary with recurrence interval. The consistency between the two families suggests that this is a robust observation (Figure 3B). Two families within the granitic basement along the foreshock-mainshock intersection both exhibit a scattered moment-recurrence behavior. This is confirmed by negligible r^2 values compared to the other two groups (Figure 3C). Outside of the mainshock-foreshock intersection exists three families that display moment-predictable behavior (Figure 3D).

By comparing recurrence time to moment, we are inherently looking for behavior that suggests the time since the previous event dictates the next event's moment. However, another possibility is that earthquakes are time-predictable, in that their moment should correlate with the time until the next event. We generally find lower r^2 values when analyzing moment versus the time until the last event compared to r^2 values seen in Figure 3, and in addition, we find no spatial grouping of any behavior (text S1/Figure S2). These repeating earthquake families could also simply be small aftershocks of a larger member of their family. We test this case in the supplement and find that large events are not the first event in their family and small events are spread out (text S2/ Figure S3).

Figure 19: 3.4 Moment-Recurrence Time Behavior of Repeating Earthquakes

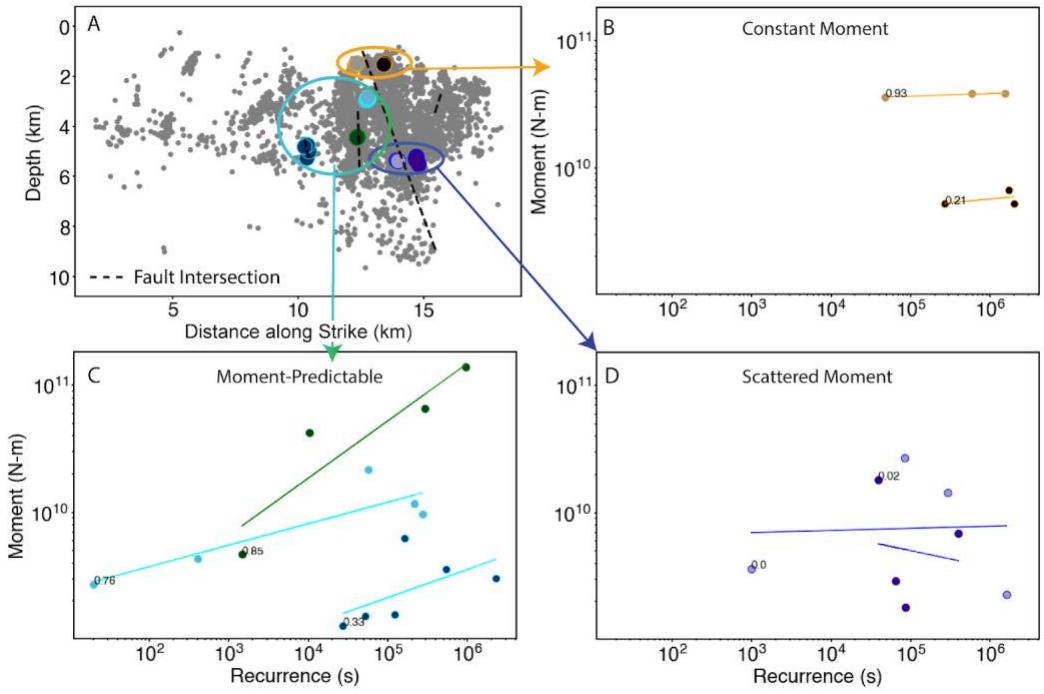

Figure 4: A) The seven families of repeating earthquakes that have more than 3 events from the repeating earthquake catalog of Okamoto et al. (2022). Fault intersections are mapped as dashed lines. **B)** Group 1, which is located in the shallower sedimentary rocks, has two families that both show that moment is consistent across recurrence intervals. **C)** Group 3 is located away from the foreshock-mainshock intersection. It includes one family that is along the mainshock-aftershock fault intersection (in green) and two families off of the main fault intersections (in cyan). All three families show moment-predictable behavior. **D)** Group 2 is interpreted to be located at the base of the mainshock rupture and at the foreshock-mainshock fault intersection. It shows scattered moment versus recurrence interval behavior.

4.2 Estimated Healing Rates of Moment-Predictable Families

The moment-predictable behavior of group 3 (families outside of the foreshock-mainshock intersection) suggests that healing might be important and measurable for these events. Assuming a circular rupture, there are two additional variables that need to be accounted for in order to calculate healing and compare it to

laboratory values: the source radius and the effective normal stress. The source radius is constrained by the source duration; however this could be a product of attenuation (Frankel & Kanamori, 1983) and therefore should be treated as a maximum source duration, i.e. maximum source radius. The maximum source radius for the three families is between 30 and 50m, so we explore all possible values below those values to calculate healing rate. Here, we are assuming that the source radius for events within one family is constant, which is unconstrained with our seismic measurements. We also analyze different effective normal stresses with the maximum possible normal stress being lithostatic pressure assuming a lithostatic gradient of 25 MPa/km. We present an example calculation that goes from seismic moment (Figure 4A) to stress drop (Figure 4B) to frictional healing (Figure 4C). This culminates in Figure 4D, where healing rate is compared to source radius at two different pore pressures ($\lambda = 0$, $\lambda = 0.9$). For the cyan familes (19 and 22), assuming a source radius of ~10 meters allows for healing rates consistent with our laboratory healing rates for Troy granite at different pore pressures (see companion paper). For family 1 (green), the measured source duration is consistent with laboratory healing rates. Adjusting pore pressure to λ=0.9, and thus lowering effective normal stress, also brings the seismic stress drop measurements closer to laboratory healing rates.

Figure 20: 3.5 Healing Rate vs. Source Radius for Moment-Predictable Repeaters

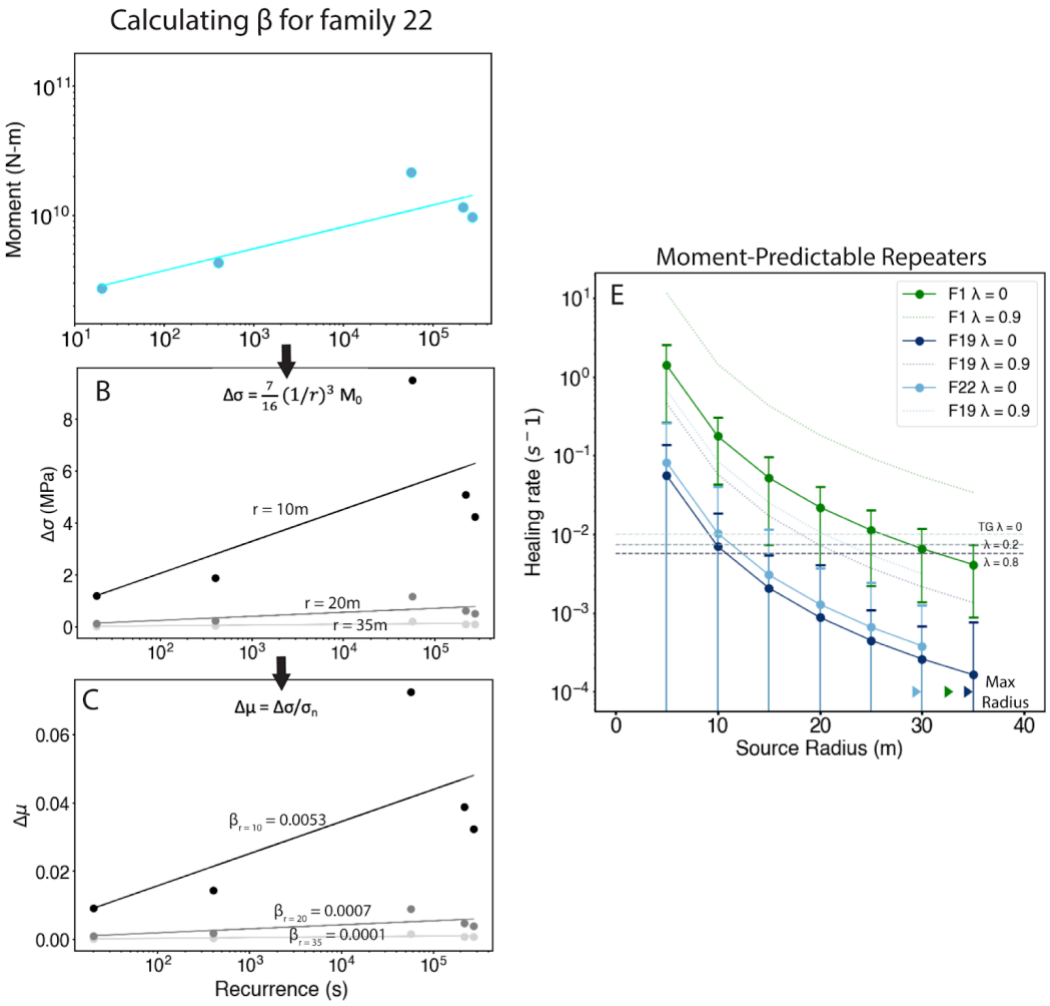

Figure 5: A-C shows an example calculation for healing rate versus source radius. **A)** Moment versus recurrence time for family 22. Other families are transparent for reference. **B)** Stress drop versus recurrence time for family 22 calculated from a circular rupture model (Brune, 1970) using a range of radii. **C)** Frictional healing, Δμ, versus recurrence time for family 22 calculated from stress drop values of B and a lithostatic normal stress. Trendlines are labeled with healing rate (β). A radius of 10 meters allows for a re asonable healing rate for family 22, while larger radii leads to values that are too small for laboratory data. **D)** Frictional healing rate versus source radius for all families (1, 19, 22) that show increasing moment with recurrence interval (group 3 families). Error bars are from bootstrapping the least squares fit with 100 iterations. Laboratory rates for the Troy Granite experiments are marked by the dashed lines colored according to their pore pressure condition as shown in Figure 3.

Max radius of each family is denoted by a sideways triangle in the color corresponding to the family color.

4.3 Estimated Stress Drop of Constant Moment Families

The two constant moment families are both located in the Arbuckle group. Any healing rate measured from these events would be extremely low. So, a comparison of healing rates for different source radii as we did in section 3.2 would not be fruitful. However, one question that we can answer with these data is an estimated amount of stress drop for each family. This is useful for understanding whether our pulse widths are likely attenuated, as well as understanding any rapid healing that occurred early on in the seismic cycle. Family 18 has a p-pulse width that equates to a source radius of ~50m and family 23 has a pulse width that equates to a source radius of ~40m. Again, this is assuming a circular rupture with a shear wave velocity of 3 km/s and, so this could vary depending on shear wave speed and assumed rupture geometry. Given these radii, mean stress drops equal to 130 and 40 kPa for families 18 and 23 respectively. These ruptures likely are also affected by attenuation, so we assume that source radii could be smaller and again assume that the source radius is the same for each event in a family. Stress drops increase when assuming a smaller radius and are in the 1-10 MPa range when assuming a rupture radius of 5-20 meters depending on the family (Figure 6A/B). We can also analyze this stress drop in terms of a change in friction, which laboratory studies typically analyze. In order to do this, we need to assume a normal stress, so we analyze normal stresses ranging from lithostatic ($\lambda = 0$) to $\lambda = 0.8$. Assuming a hydrostatic pore fluid

pressure gradient (λ = 0.4) and a radius of 10-20 meters, Δμ ranges from 0.1 to 0.7 for family 18 and 0.01 to 0.1 for family 23. A radius of 20m for family 18 and 10 meters for family 23 shows a change in friction of 0.1 and a stress drop of 2-3 MPa.

Figure 21: 3.6 Stress Drops of Constant Moment Repeaters

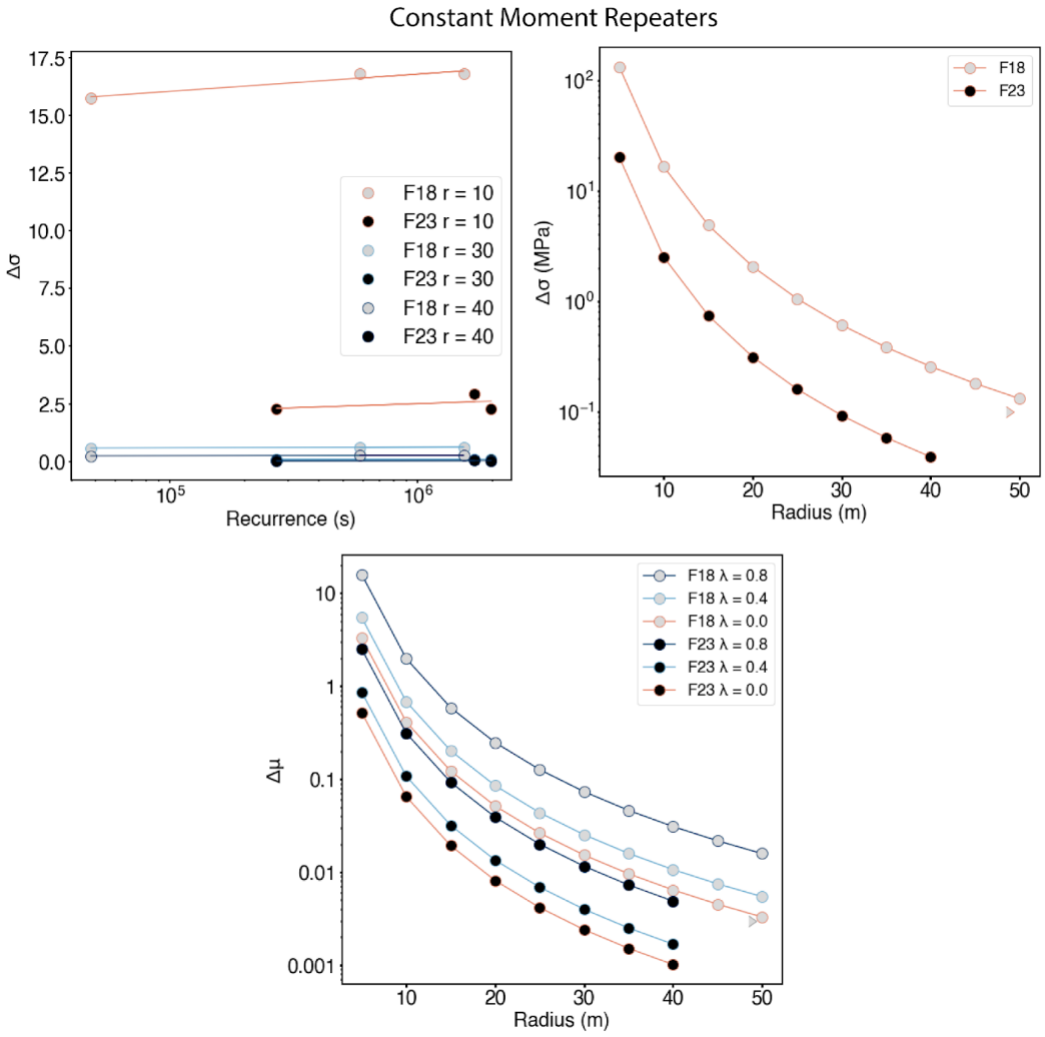

Figure 6: Analysis of constant moment repeating earthquake families 18 and 23. Family 18 is marked in a light infill and family 23 is marked in a black infill. A) Stress drop versus recurrence time with various radii = 10m, 30m, and 40m. B) Mean stress drop for each family for a given source radius versus source radius. Grey and black triangles note the mean source radius as derived from the p-pulse width for family 18 and 23 respectively. C) Change in friction versus source radius for a range of different normal stresses. Triangles are the same as in B.

5. Discussion

5.1 Assumptions to Calculate Stress Drop

There are two key assumptions that we used here to calculate stress drop: 1) a circular rupture and 2) a constant source radius for each event within a family. A physical explanation for this model is that a circular asperity is surrounded by a velocity-strengthening barrier that each earthquake cannot nucleate into, so slip increases with magnitude, but rupture size does not. Small earthquakes with magnitudes between M0-M2 are typically modeled with a circular rupture because their smaller size suggests a smaller amount of heterogeneity and resolution does not allow for the ability to measure the complexity of smaller earthquakes. However, it is possible that smaller earthquakes also exhibit complex ruptures and that this can explain different moment behaviors of repeating earthquakes (Lin & Lapusta, 2018). However, there is no seismological constraint on this complexity, so we assume a circular rupture. In general, the Prague repeater stress drop is more consistent with typical seismic stress drops (1-10 MPa) and healing rate is consistent with laboratory healing rates (~0.01 s^{-1}) if the p-pulse is attenuated (Figure 5, 6). Given that the p-pulses are all similar, attenuation and source duration should be similar for all events within the circular rupture model. However, it is possible that source duration differences equivalent to a change in source radius of a few meters could be masked by attenuation. This small change in source radius could change the healing rate measured, however we do not have a good constraint on which earthquakes might be

smaller or larger. Instead, we assume a constant source radius, which within the circular rupture assumption and within the measurements we have, is a good assumption. Another possible assumption is that stress drop is constant, but this should result in a recurrence time scales with $M_0^{1/3}$. Another assumption is that an increasing proportion of the source radius slips aseismically for smaller ruptures. This has been shown to occur in a creep-slip model and via a rate-state like nucleation phase (Beeler et al., 2001b; Chen et al., 2007; Cattania & Segall, 2009). These models do not include any measurement of frictional healing that could be compared to laboratory work. In addition, we have varied moment-recurrence time relations, which is possible with our slip-predictable model and is suggested by the similarity in p-pulse measurements within each family.

5.2 The Cutoff Time and Reloading Velocity

The only other analysis of healing during repeating earthquakes measured a 100-day delay in healing (Marone, 1998). That delay in healing was interpreted as being caused by afterslip of the previous event and a slow reloading velocity during the nucleation of the event within the rate-state framework (Marone, 1998). A delay in healing could be causing the low apparent (derived from the measured p-pulse width) healing rates in the moment-predictable group and no healing rate measured by the constant moment group. Marone (1998) assumed a plate-rate reload velocity, however these earthquakes are occuring in a aftershock sequence, so here we analyze a variety of reload velocities that might represent the velocity of the aseismic slip

region driving the repeating earthquakes (Figure 7). We show that with a sufficiently high aseismic slip velocity (μm/s), the delay in healing is short and thus healing rates similar to laboratory values may be measured here. The critical slip distance, the choice of evolution law, stiffness (K, which depends on the rupture radius and shear modulus of the surrounding rock), and normal stress affect the cutoff time, so it is not easy to scale the time it takes to start healing from the lab to the earthquake scale (Im et al., 2017). Regardless of these smaller effects, slow-slip velocities can shorten the cutoff time and allow for healing within repeating earthquake timescales analyzed here. In addition, it would be surprising that the differences in moment-recurrence time behavior between the earthquakes in the Arbuckle group and in the basement granite were caused by the same mechanism. At lower normal stresses, the frictional stiffness (K/σ) is larger than in areas with higher normal stress. Therefore, the cutoff time in the basement is longer than the cutoff time in the Arbuckle if all other parameters remain the same, suggesting that the constant moment cannot be explained by the cutoff time if the basement repeaters are not also explained by it. So, we assume for the rest of the paper that the cutoff time is not the cause of the low apparent healing rates.

Figure 22: 3.7 A Model of the Cutoff Time

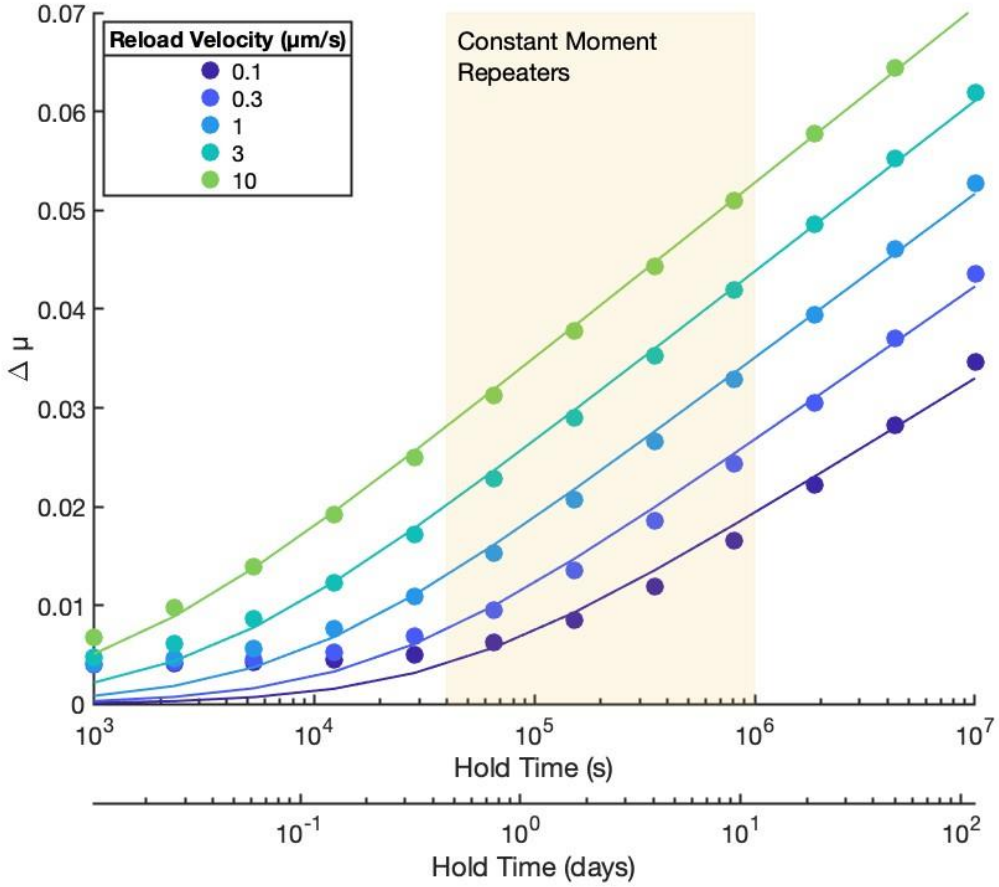

Figure 7: Frictional healing versus hold time (s) using the slip law for simulated slide-hold-slides to highlight changes in the cutoff time with reload velocity. The initial sliding velocity is 1 m/s. We use a stiffness for a 20 m rupture and a 30 GPa shear modulus ($K = G/L$), $a = 0.008$, $b = 0.008$, $D_c = 5$ mm, and normal stress = 30 MPa (hydrostatic for the Arbuckle). Loading here is caused by afterslip, so we analyze a reload velocity of 0.1 μm/s to ~10 μm/s. Constant moment repeaters occur at longer timescales than the cutoff time for all reload velocities analyzed. Hold time is converted to days on the second x-axis.

5.3 The Timing of Repeating Earthquakes

If constant loading is assumed, constant healing behavior is the same for each event, and a stress drop to a constant background strength is assumed for each event, then repeating earthquakes should have constant recurrence intervals with constant stress drop, as in the characteristic earthquake model. One study found that this model fits just as well as slip or time predictability for repeating events (Rubinstein, Ellsworth, Chen, et al., 2012). Here, we see different recurrence times with either constant moment or varying moment. Variations in recurrence time could exist within this framework if dynamic triggering is occurring. For this, the loading rate allows for the system to get close to failure and then a dynamic event increases shear stress in order to have failure occur earlier than it would have if loading rate were to continue until it reached the failure strength of the fault (Figure 8B/C/D). This has also been shown to occur in laboratory studies (Savage & Marone, 2008).

5.4 Constant Moment Repeaters

We interpret Group 1's constant moment as evidence of a lack of healing and no large variability in loading conditions over these time scales. Our preferred explanation for this behavior is that the Arbuckle has no measurable healing between repeating earthquakes due to pore fluid that allows for dissolution at the asperity contacts except for healing at the start of the interseismic period, which will be discussed in the next paragraph. Weakening at high pore fluid pressures ($\lambda = 0.8$) is measured in our companion paper and a lack of healing is seen at pore fluid pressures

of $\lambda = 0.6$.. As we outline in our companion paper, dissolution of carbonate is the likely mechanism of weakening either through creating smaller asperity contacts or weaker asperity contacts. How this applies to the natural system depends on the kinetics of dissolution. Directly applying our laboratory result of $\lambda = 0.6$ to our repeating earthquakes, which are at depths ~1.5km, suggests that pore pressure equals equal to ~22.5 MPa and this value is 7.5 MPa over hydrostatic values. However, dissolution could be controlled by the chemical composition of the pore fluid, so translating the exact pore pressure at which dissolution occurred in the lab to the seismic scale is not appropriate. Therefore, a variety of factors might influence the exact pore fluid pressure where a lack of healing is seen. These factors might include the chemistry of the water, the components of the gouge (percentage calcite, dolomite), and the amount of localization occurring within the gouge.

Regardless of the weakening mechanism in our experimental results, explaining the constant moment repeating earthquakes still requires some initial healing for there to be a stress drop. It is possible that rapid healing immediately following each earthquake could be caused by high temperatures created during seismic slip (Bedford et al., 2023; Savage et al., 2019). It could also be possible that pore fluid is not present following an event, which allows for healing. Pore fluid may then move into the fault during the post-seismic phase and begin dissolving contacts again. However, this would require that healing occurs after the cutoff time, but before the start of stagnant healing due to dissolution, and so we find that rapid healing due to temperature rise following an earthquake is more likely (Figure 8B).

Further analysis on rapid healing from temperature rise could help interpret the values of Figure 6. No high-velocity slide-hold-slides have been conducted on carbonates. However, high temperature low velocity healing experiments show rapid healing of carbonate (Chen et al., 2015), which indicates that rapid healing would also occur in carbonate post-seismically. While a stress drop of ~100 kPa might be occurring for these small events, source radii of 10-20 meters for a hydrostatic pressure gradient allows for a 2-3 MPa stress drop and a change in friction ~0.1, which is consistent with an ~8 MPa average stress drop for this sequence (Pennington et al., 2021) and experimental results of rapid healing (Bedford et al., 2023).

5.5 Scattered Moment Repeaters

The scattered moment behavior of repeating earthquakes at the intersection of the foreshock and mainshock fault plane within the basement could be caused by many different mechanisms. Two possible mechanisms include: 1) erratic loading conditions or 2) erratic pore fluid pressure conditions (Figure 8D). Erratic loading conditions could be caused by changes in the velocity of the surrounding aseismic slip. Given that this area has the highest density of aftershocks, interactions between different stressors could cause changes in this velocity (Okamoto et al., 2022). This changes the moment behavior because healing depends on reload velocity (Figure 7/8D). Erratic pore fluid pressures could also cause this behavior if an abrupt, large change in pore fluid pressure were to bring the fault to failure for some cases, but not in other cases (Figure 8D). The foreshock-mainshock fault intersection host the

closest repeating earthquakes to the main injection site, and so likely have high pore fluid pressure (Figure 2). Even so, we do not have a favored mechanism for erratic healing between pore fluid or loading rate variabilities.

5.6 Moment-Predictable Repeaters

The moment-predictable behavior of repeating earthquakes outside of the mainshock-foreshock fault intersection indicate that fault healing might be measurable in the Prague sequence. To measure healing, we assume a slip-predictable behavior, where slip is changing between events and not the source area as we discussed in section 5.1. For families 18 and 22, we find that the source radius has to be smaller than measured in order to calculate a healing rate that is consistent with our laboratory healing rates. For family 1, we find that the healing rate measured using the measured pulse duration is consistent with laboratory healing rates of granite, however an assumed radius as small as 20 m is still consistent. We tested whether high pore fluid pressure could allow for consistent healing rates even with no attenuation and found that even with $\lambda = 0.9$, the source radii still need to be smaller than the measured healing rate for families 18 and 22 assuming no attenuation (i.e. maximum radius) (Figure 5). This suggests that source duration measurements, such as p-pulse width, is attenuated for families 18 and 22, and might be attenuated for family 1.

Figure 23: 3.8 Explanation of Moment-Recurrence Behaviors

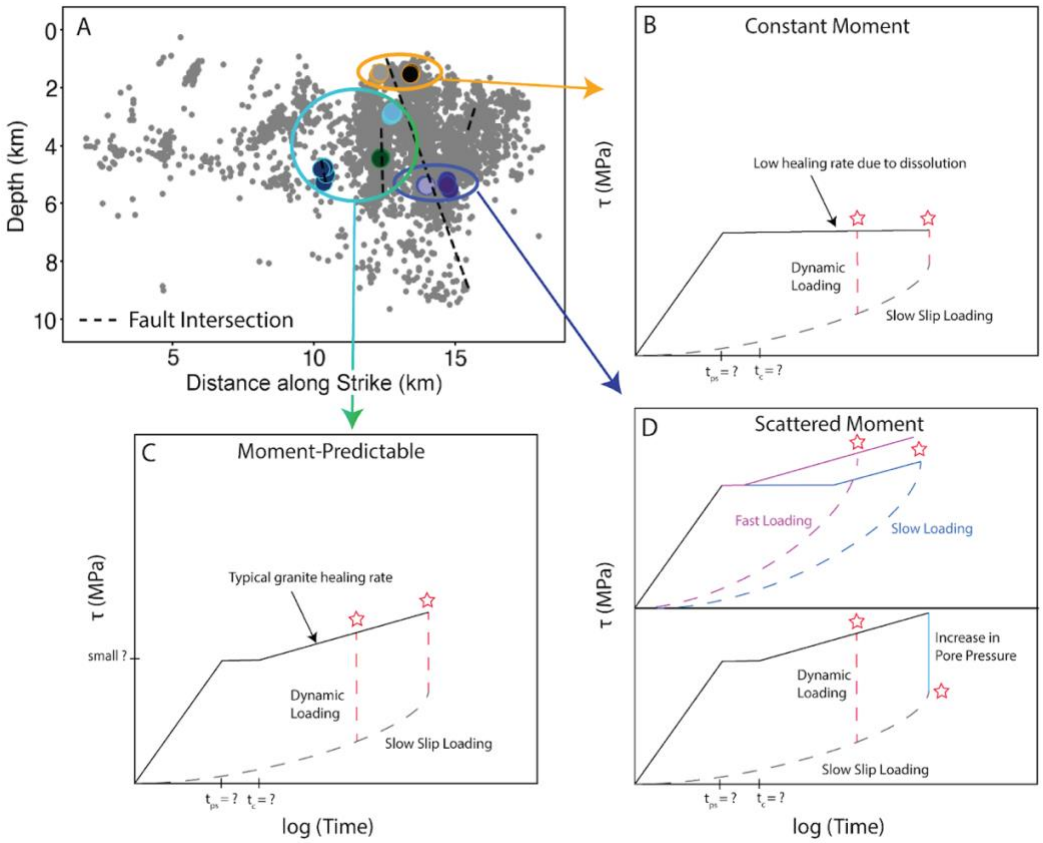

Figure 8: A) The locations of repeating earthquakes analyzed as shown in Figure 4. **B/C/D)** A cartoon explanation of the seismic cycle for each group. Red stars indicate earthquakes and the location of them indicate the amount of stress drop assuming a total stress drop. **B)** Constant moment indicates that a period of postseismic healing had to occur, which is followed by a period of stagnant healing possibly due to reduced weakening from dissolution. **C)** Moment-predictable is consistent with typical laboratory healing rates. **D)** Scattered moment could be caused by a chaotic aseismic slip loading rates or highly variable pore fluid pressure changing fault strength. In both cases, a low stress drop event can have a longer recurrence time than a high stress drop event, which is not true for the scenarios in B and C.

5.7 Implications for Induced and Tectonic seismicity

This study supports our companion paper's finding that enhanced dissolution could be occurring in the Arbuckle Group. Dissolution of contacts from injected

fluids that are out of equilibrium with carbonates might cause long-term weakening of faults that could lead to failure. This is discussed more fully in our companion paper. Although the Prague sequence was induced, it is likely that the variable healing patterns seen here also occur after tectonic earthquakes. As such, variable healing would lead to variations in fault strength over time. Such strength heterogeneity along the fault could lead to heterogeneity in stress distribution.

6. Conclusion

We analyzed the relationship between moment and recurrence time for repeating earthquakes during the 2011 Prague, Oklahoma aftershock sequence. We found three spatially separated groups of repeaters that suggest different healing styles: constant moment in the Arbuckle group, erratic moment in the granite at the intersection of the mainshock-foreshock faults, and moment-predictable behavior in the granite off of the mainshock-foreshock fault intersection. We interpret that the constant moment group of repeating earthquake families, which is located in the Arbuckle dolomite, is caused by a low healing rate associated with an influx of water that is unsaturated in carbonate. If our laboratory healing results can be directly translated to the Prague earthquakes, then pore fluid pressure during this aftershock sequence in the location of the repeating earthquakes within the Arbuckle dolomite ~7.5 MPa over hydrostatic. We find that erratic moment behavior could be caused by variable loading rates of surrounding aseismic slip or variable pore fluid pressure. We find that the moment-predictable group is consistent with laboratory healing rates for

Troy granite, however the exact healing rate is difficult to constrain because of uncertainties in source area and the effective normal stress. Overall, this study finds that differences in healing behavior can be mapped in an aftershock sequence from microseismicity and, it supports our companion paper that an increase in pore fluid pressure can frictionally weaken carbonate rocks during the hold time.

Appendices

Appendix A: Chapter 1 Supplementary Material

Text S1: Recurrence interval versus time as an indicator of afterslip

We interpret our results as indicative of afterslip. Qualitatively, afterslip is an aseismic slip motion following an earthquake and so, we expect that a large portion of the aseismic slip seen here should be afterslip. Quantitatively, we see that recurrence interval increases with time since the mainshock. This is expected based on the relationship between recurrence interval in slip rate:

$$V_L = Ct_r^n,$$

where V_L is the loading velocity, C is a constant, t_r is recurrence interval, and n is an exponent that depends on the time dependent strengthening rate (Beeler, et al., 2001a). The loading velocity here is the slip rate of the afterslip that is causing the repeating earthquakes. The slip rate decreases logarithmically with time during afterslip. Slip rate also decreases with increased recurrence interval via the power law form above. The exact form depends on healing rate. This ends up where the recurrence interval is approximately linearly dependent on time, which is shown in Figure S1. Repeating earthquakes that occur late in time with a short recurrence interval indicate that we may be missing some repeating earthquakes in their families.

Figure 24: A.1 Recurrence Interval versus Time since Mainshock

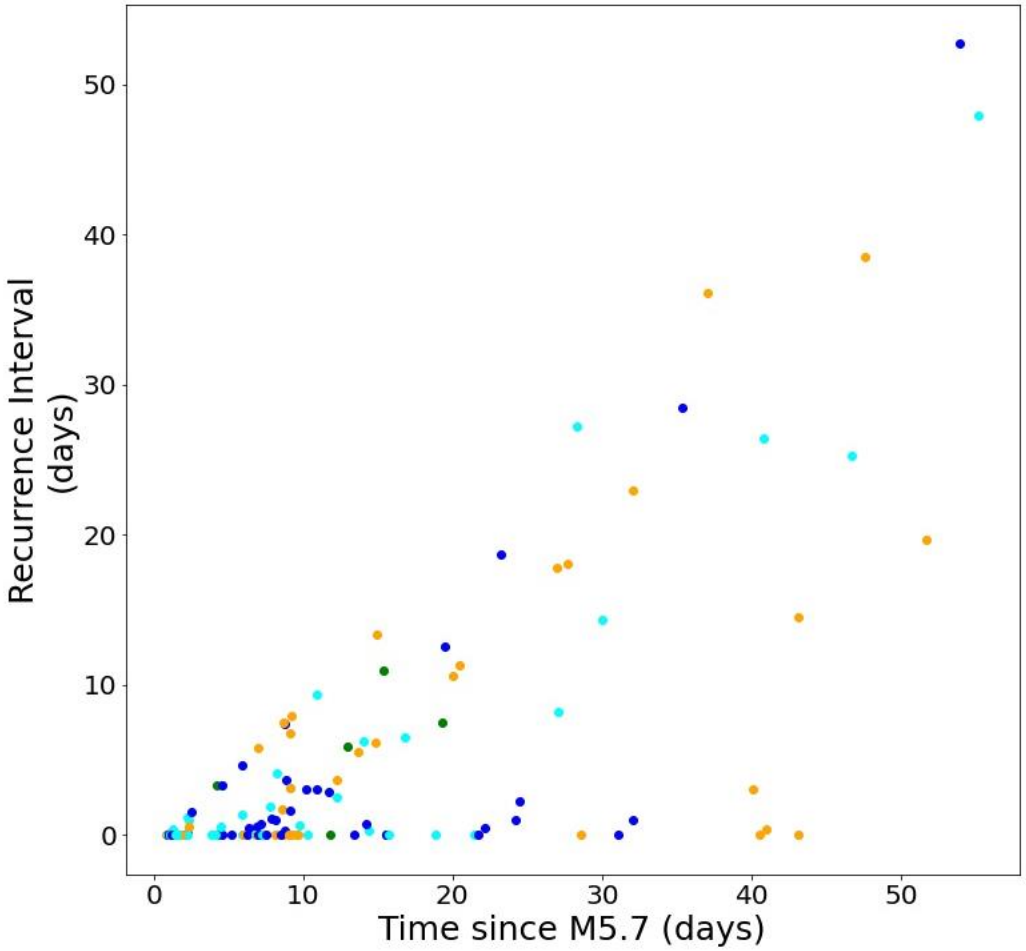

Figure S1: Recurrence interval vs. time for the repeating earthquakes. The repeating earthquakes are colored according to the group number.

Text S2: Methods for calculating rupture area and overlap

We determine whether the rupture areas of each family are overlapping in order to understand if our repeaters are well enough defined. To do this, we use the relationship

$$r = \left(\frac{7}{16\Delta\sigma} M_0\right)^{1/3},$$

where r is the rupture radius, M_0 is moment, and $\Delta\sigma$ is stress drop (Eshelby, 1957). We must assume a stress drop, so we use 10 MPa which is similar to the average of ~8 MPa calculated by estimates from (Pennington et al., 2021). We calculate moment, M_0, from magnitude, M_w, using the relation

$$M_0 = 10^{1.5*Mw + 9.05}$$

(Hanks & Kanamori, 1979). We plot the rupture area of the repeaters for each family assuming a circular rupture with the radius calculated from above. The uncertainty on the locations are 112 m and 113 m vertically (Cochran et al., 2020). Families 22 and 36 contain non-overlapping ruptures (Figure S2).

Figure 25: A.2 Repeating Earthquake Overlapping Ruptures

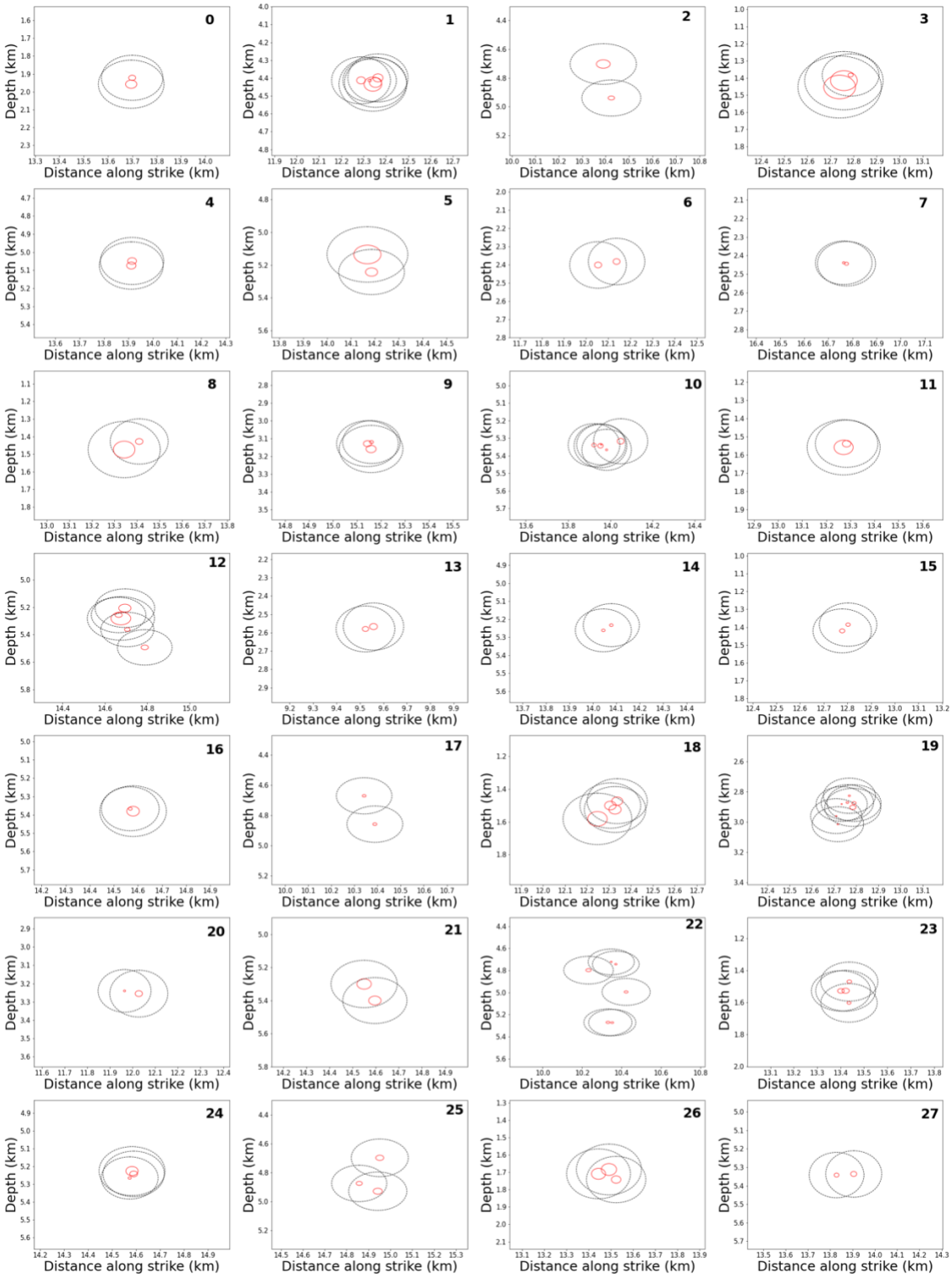

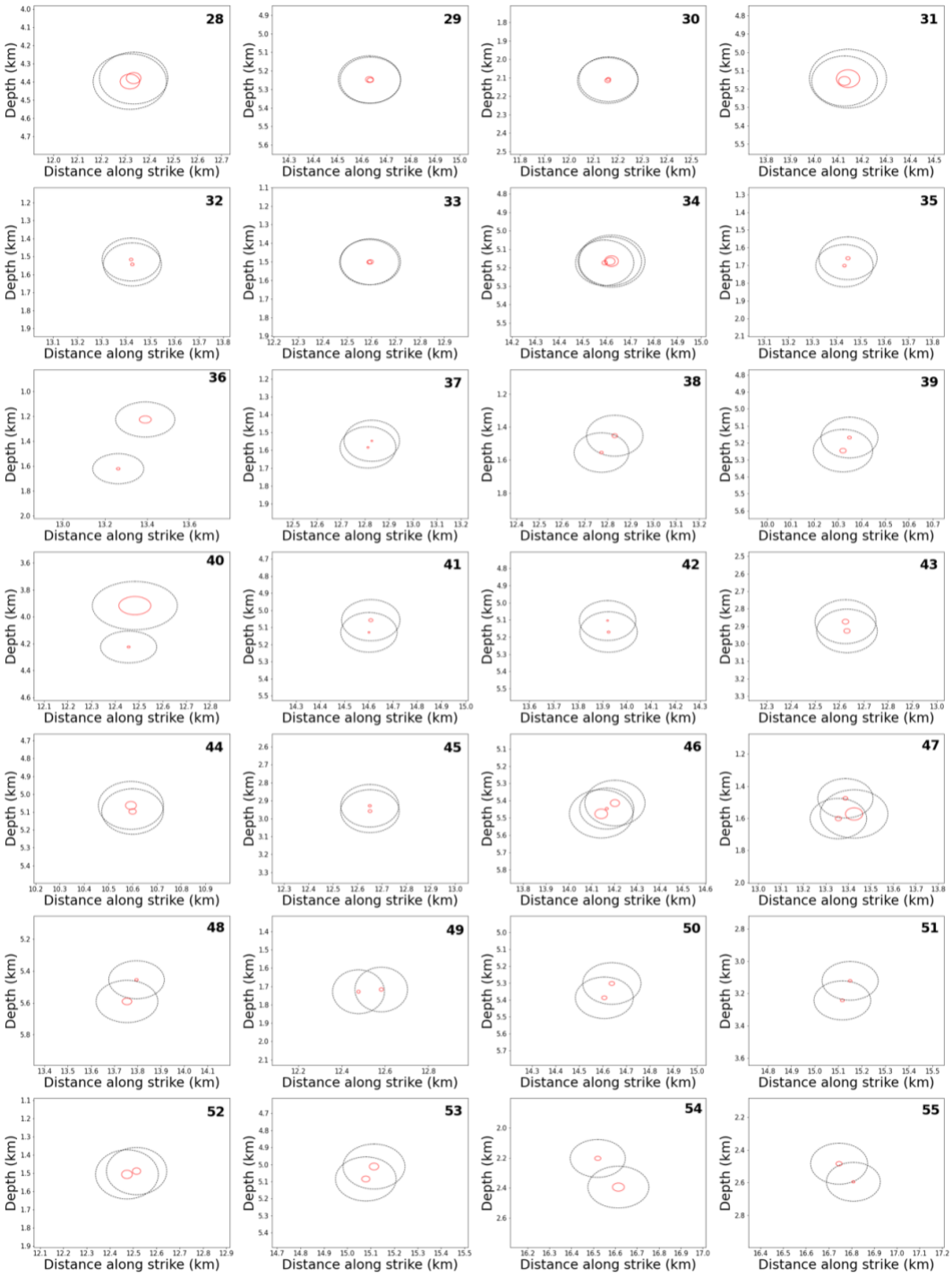

Figure S2: Overlapping rupture figures with distance along strike on the x-axis and depth on the y-axis. Red circle is the rupture patch and black dashed lines represent a 112m location uncertainty. Family number is located in the upper right corner.

Appendix B: Chapter 2 Supplementary Material

Text S1: Arbuckle Core Selection

We sampled the Arbuckle group from a core at the Oklahoma Petroleum Informative Center (OPIC). The core (#4554) was selected from the OPIC database based on its proximity to Prague (Figure 1). It was listed as an unmarked formation, but is located at the correct depth for the Arbuckle formation. When sampling, we ensured that core #4554 was made of carbonate. We analyzed the depth of cores in its immediate vicinity to ensure that the core was not in the largest group of overriding carbonate, the Hunton Limestone, and above the underlying basement. The Hunton limestone is considerably shallower in the area, at a depth of 1.3 km, whereas our sample is from a depth of 1.83km. We find that a depth of 1.83km should be located in the middle of the Arbuckle group based on nearby well data. In addition, the thickness of the Arbuckle group is typically ~1 km, whereas the Hunton limestone is only 10's of meters thick.

Figure 26: B.1 Arbuckle Core Location

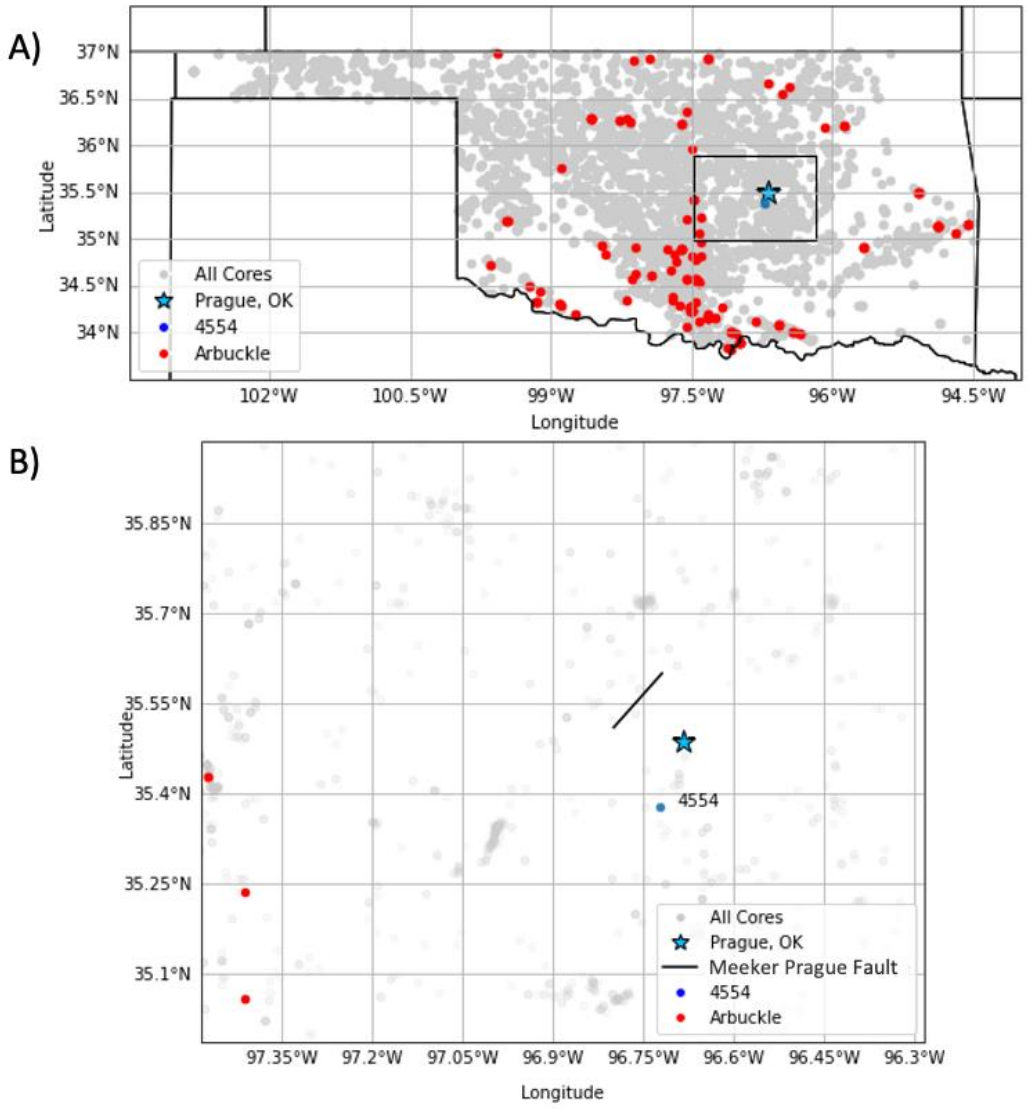

Figure S1: A) Map of Oklahoma with location of cores in the OPIC database. All of the cores are in grey, cores that contain Arbuckle are highlighted in red, and core #4554 is in Blue. Location of Prague is shown by the star. Box is the location of the inset figure. **B)** The inset shown in A) of the area around Prague indicating the location of core #4554 relative to the portion of the fault that hosted the M5.7 earthquake (the Meeker-Prague fault) and the town of Prague, Oklahoma.

Text S2: X-ray diffraction of sample material

We analyzed the starting material of core #4554 with x-ray diffraction (XRD) using a Rigaku SmartLab in the UC Santa Cruz Department of Chemistry and Biochemistry's X-ray facility. We used X'Pert Highscore Plus software to fit the data to an existing library of XRD patterns for minerals. The software models the sample's pattern with 90% dolomite and 10% quartz, with one missing peak that could be quartz or Ankerite, but only change the content by a few percent (Figure S2).

Figure 27: B.2 Arbuckle XRD Results

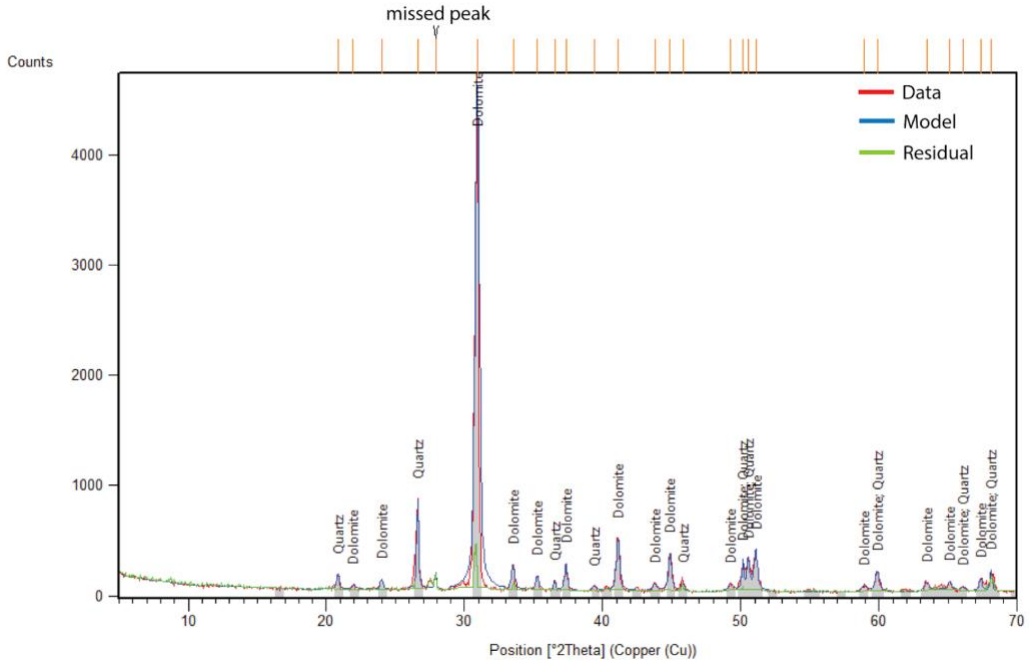

Figure S2: X-ray diffraction pattern for the sample used in the experiments on the Arbuckle formation. Analysis by the X'Pert Highscore Plus software modeled the sample with ~90% dolomite and ~10% quartz. One missing peak is indicated at the top and by the residual green line at the bottom. This peak can be fit by either quartz or Ankerite, but is too uncertain to choose and would only change the dolomite and quartz content by a few percent.

Text S3 Drainage Conditions

We recorded displacement of each pore fluid intensifier as well as pressure in each intensifier. Here, we analyze the pore fluid intensifier characteristics for a 1000s hold period (Figure S3). The downstream pore pressure intensifier (P_p1 displacement) was backed out at the start of each experiment and, so it should not move. However, it moved slightly in during the hold, possibly due to pore fluid pressure 2 backing out. This displacement was consistent across each experiment, measuring ~10μm, just above the ~10μm background noise (Figure S3A/E). The downstream pore fluid pressure intensifier recorded a slight increase in pore pressure that then recovered to the previous pressure on the re-slide. This increase in pressure was ~0.02 MPa for the Arbuckle experiments and up to ~0.08 MPa for the Troy granite experiments (Figure B/F). This shows the system is mostly drained, however exhibits some undrained effects that lead to small perturbations in the downstream intensifier.

The upstream pore fluid pressure displacement (pore fluid pressure 2 displacement) decreased during the hold, indicating that the intensifier had to fill in order to maintain constant pressure. This indicates that compaction was occurring during the hold, just as we measured on the radial LVDT measured. Compaction as measured from the upstream pore fluid intensifier is increased with increased pore fluid pressure, also consistent with the radial LVDT measurements (Figure 6). The upstream intensifier displacement then increased during the re-slide due to dilation (Figure S3C/G). Pore fluid pressure in the upstream intensifier was controlled and did

not change during the hold (Figure S3D/H). Note that not all experiments are analyzed here due to small leaks in the pore fluid intensifier system during experiments 49 and 55, and experiment 54 did not use the pore pressure system.

Figure 28: B.3 Pore Pressure System Response

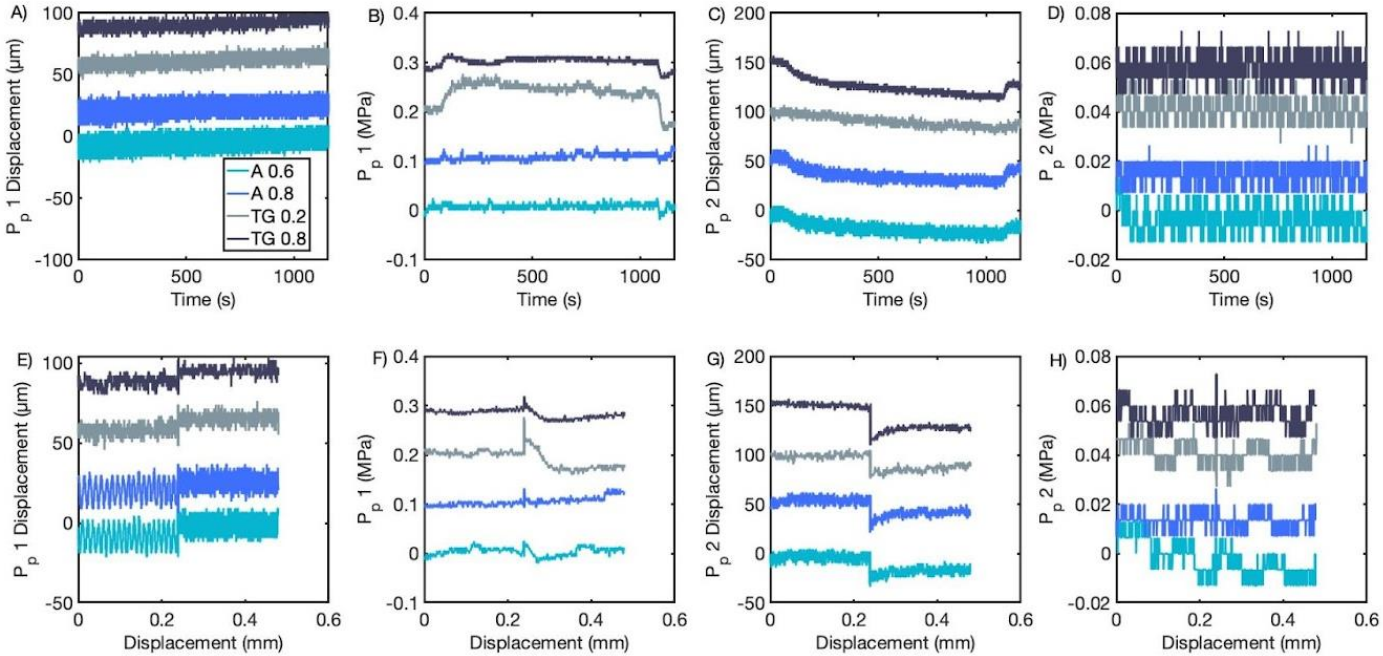

Figure S3: The change in pore fluid intensifier displacement and pressure as measured for a 1000 second hold for experiments 50, 52, 57, and 58. Each experiment is offset for clarity. Pore fluid intensifier 1 is the downstream intensifier and pore fluid intensifier 2 is the upstream intensifier.

Text S4 Repeat High Pore Pressure Arbuckle Experiment

Here, we report another experiment with high pore fluid pressure with P_p = 40 MPa and P_c = 50 MPa, which are the same conditions as UC57. It experienced normal stress greater than the effective normal stress of the experiment during pressurization. To attempt to counteract this overpressure, the sample was then given less effective normal stress than during the experiment. This was somewhat successful in getting to a typical state during pre-compaction, however dilation throughout the experiment occurred, suggesting that overcompaction influenced the behavior of the gouge. Nevertheless, the gouge behaves in a similar manner to UC57. This is shown by a similar steady-state friction coefficient, and similar weakening and relaxation during slide-hold slides (Figure S4), suggesting that this behavior is robust.

Figure 29: B.4 Repeat High Pore Pressure Arbuckle Experiment

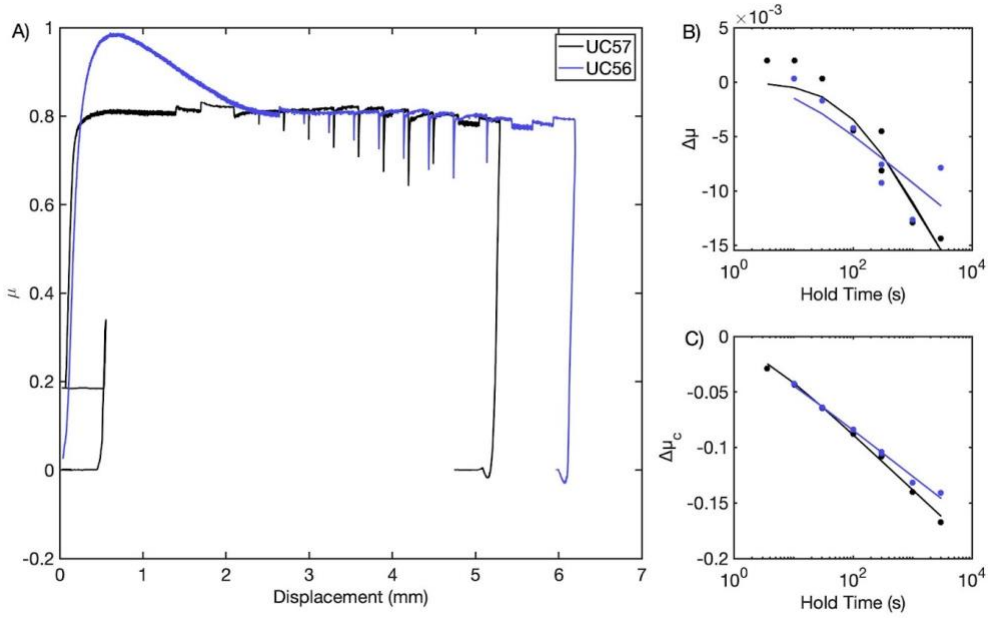

Figure S4: A comparison of repeat experiments 56 and 57 (both Arbuckle dolomite with pore pressure = 40 MPa). **A)** Displacement versus friction. **B)** Frictional weakening (Δμ) following the hold versus hold time. **C)** Stress relaxation during the hold.

Text S5:

We used the software RSFit3000 to fit velocity-stepping tests (Skarbek & Savage, 2019). We ran tests from 1 to 3 μm/s and from 3 to 10 μm/s. We fit the velocity-step tests to either the one-state or two-state rate-state equation. The rate-state equation with one state variable is presented as equation 1 in the main text. The two-state variable rate-state friction law is:

$$\mu = \mu_0 + a\ln(V/V_0) + b_1\ln(V\theta/D_{c1}) + b_2\ln(V\theta/D_{c2}).$$

This is commonly interpreted as two deformation mechanisms being required to fit a rate-step ( ). For both the Troy Granite and the Arbuckle Dolomite, the two-state rate-state friction law was required to fit some of the velocity steps (Figure S4/S5).

Figure 30: B.5 RSFit3000 Fits Arbuckle Dolomite

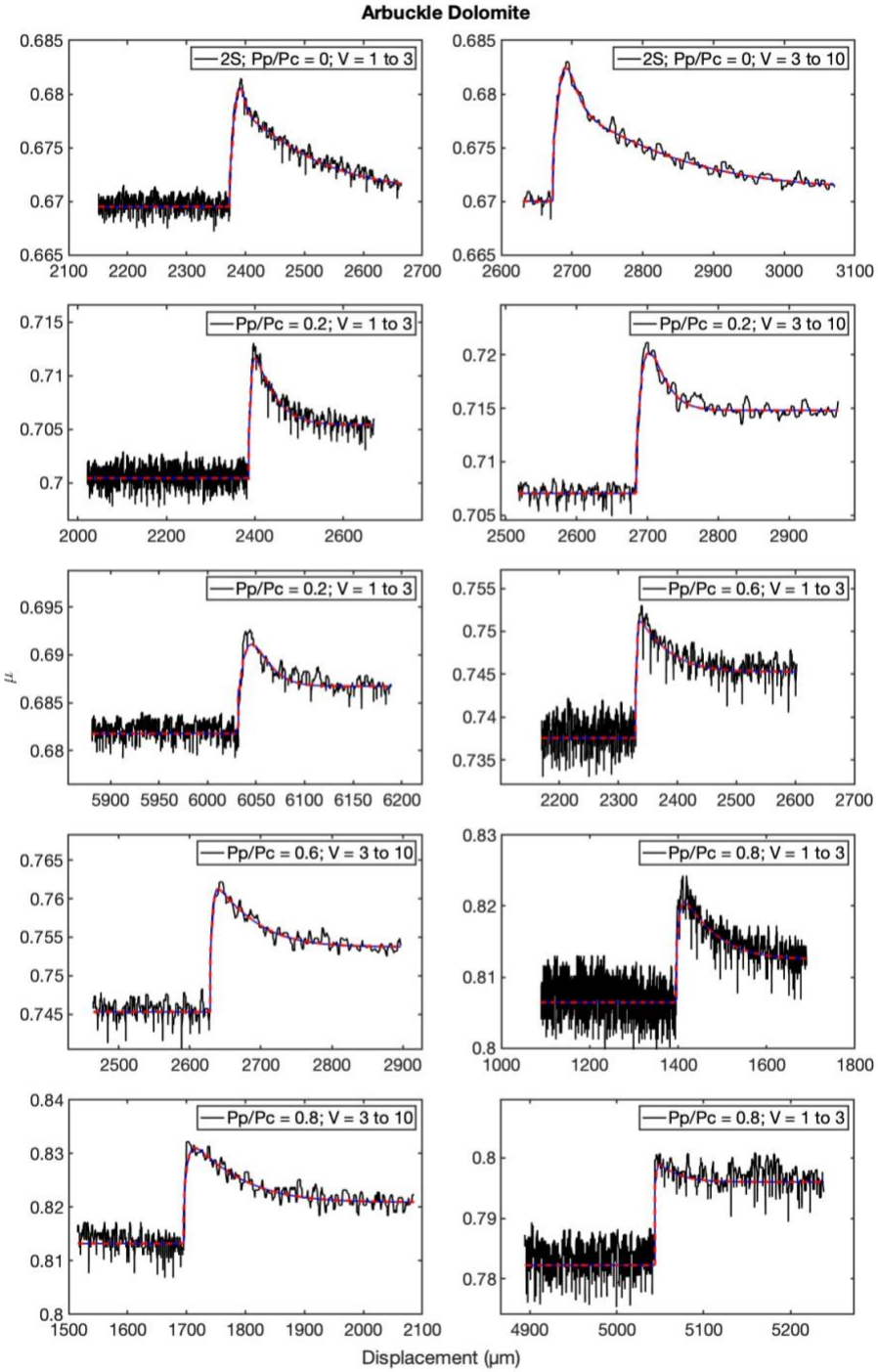

Figure S5: RSFit3000 results for rate-stepping tests for the Arbuckle Dolomite. All steps used to average each condition is listed. If two state variables were used then the legend includes 2S before the Pp/Pc condition.

Figure 31: B.6 RSFit3000 Fits Troy Granite

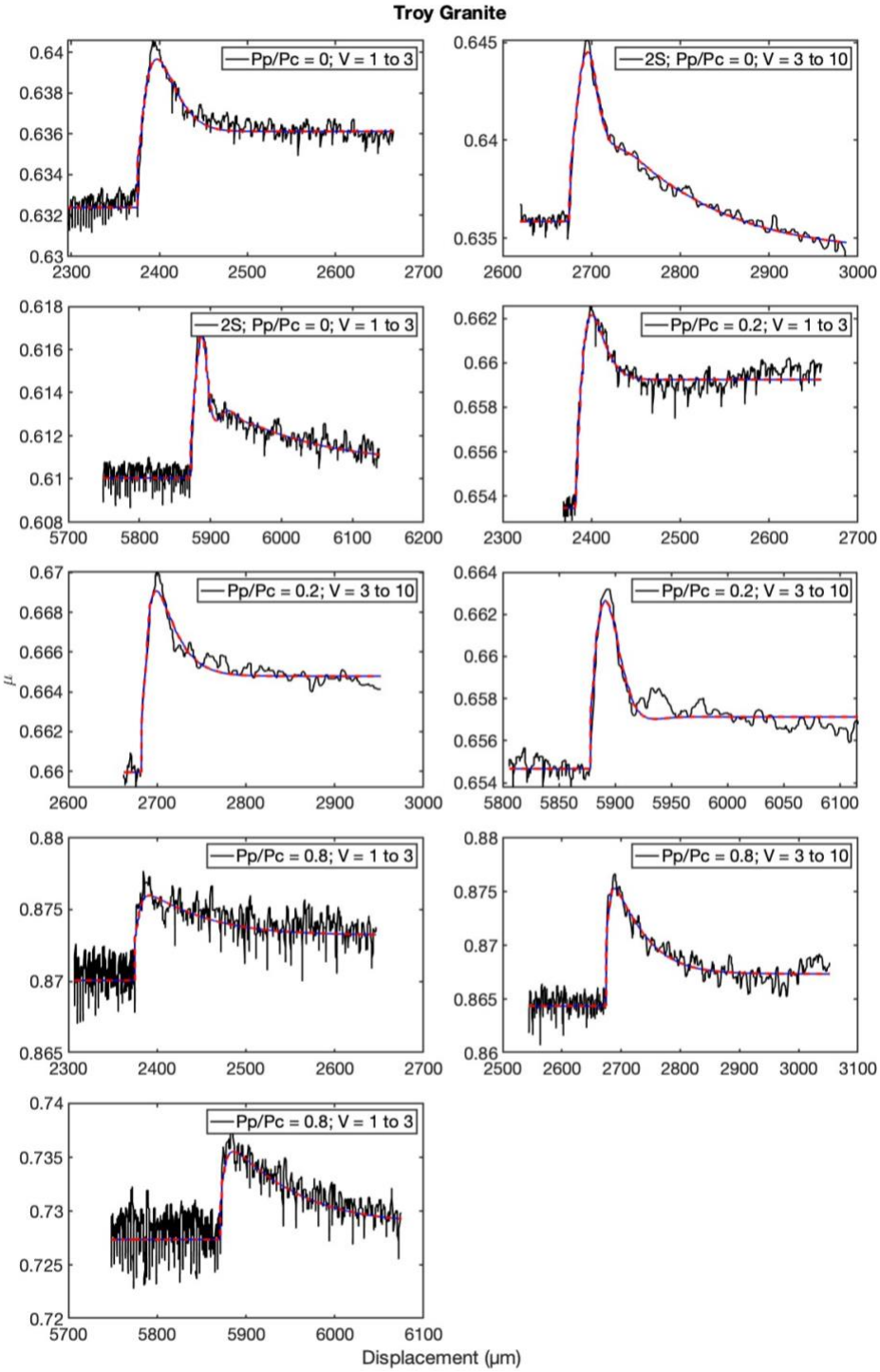

Figure S6: RSFit3000 results for rate-stepping tests for the Troy Granite. All steps used to average each condition is listed. If two state variables were used then the legend includes 2S before the Pp/Pc condition.

Appendix C: Chapter 3 Supplementary Material

Text S1. Time predictability

One possible model for repeating earthquake recurrence is moment-predictable behavior, which was discussed in the manuscript. Another model for earthquake recurrence is time-predictability, where the time until the next event can be predicted, while the moment of the next event is random (Rubinstein et al., 2012a; Shimazaki & Nakata, 1980). In other words, time-predictable systems have a known failure threshold and incomplete stress drops (Figure S1). Can the Prague repeating earthquakes be explained better by time-predictable behavior than moment-predictable behavior? To answer this, we explore whether moment depends on the time until the next event. In general for each family of events, the data are more scattered (lower r^2) values when plotted in this way. In addition, there is no clear spatial pattern to the data (Figure S2).

Figure 31: C.1 Time-Predictable versus Slip-Predictable

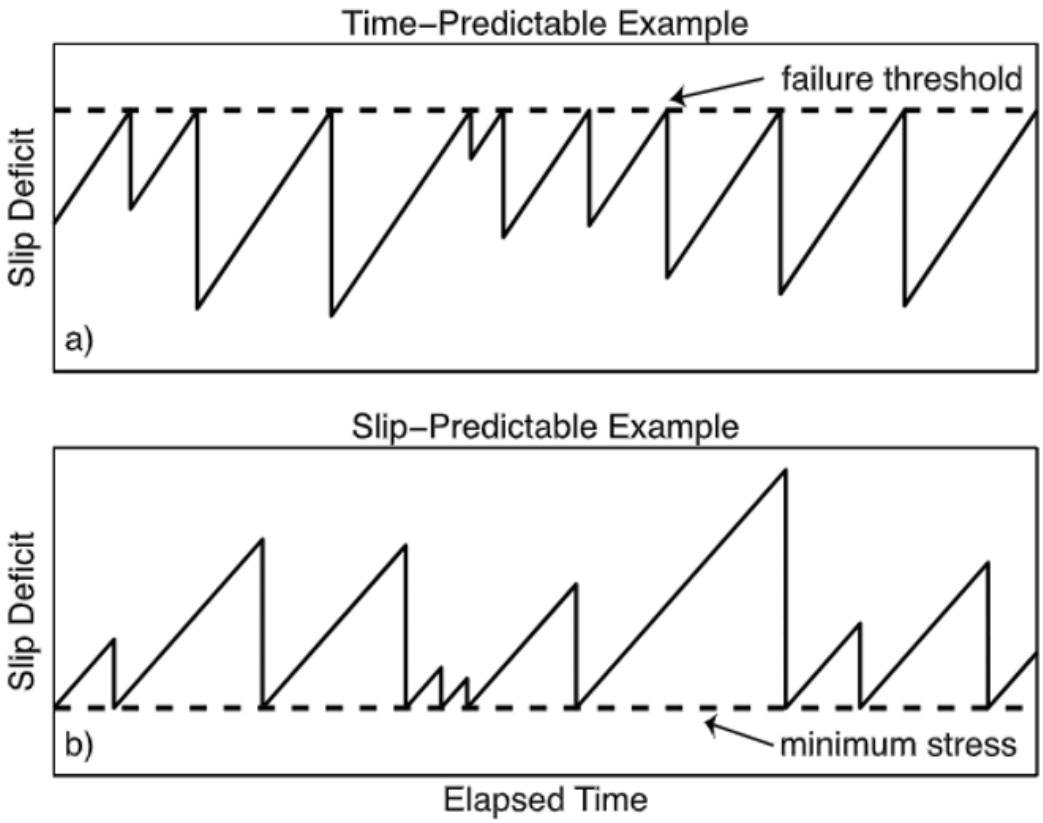

Figure S1: Time-predictable behavior versus slip predictable behavior (from (Rubinstein et al., 2012a).

Figure 32: C.2 Testing Time-Predictability

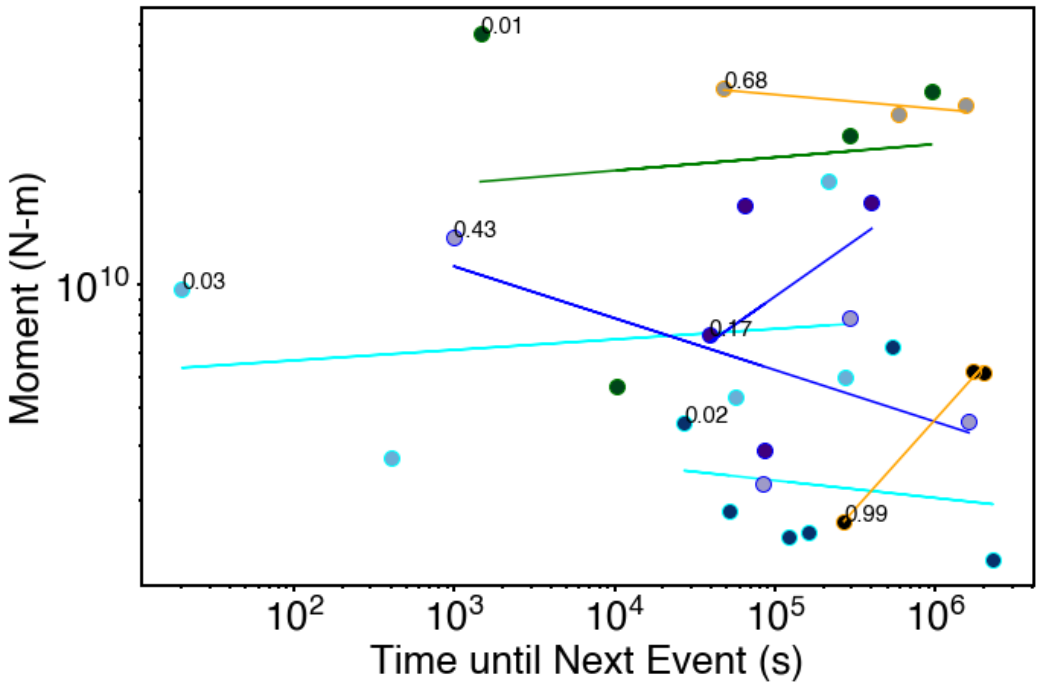

Figure S2: Moment versus time until next event shows no spatial grouping of different behaviors and typically have lower r^2 values than moment versus recurrence time. Color indicates family as in figure 4.

Text S2. Are these events just nearby events that are aftershocks of each other?

It is difficult to tell if repeating earthquakes actually rupture the same patch repeatedly or if they are just nearby events. Location errors of these events are bigger than the actual events and so whether a patch is truly the same cannot be answered conclusively. In order to test whether these are nearby events that are aftershocks of each other, we analyze whether the big event occurs first and then followed quickly by smaller events. Figure S3 shows that the larger magnitude events are not the first event in the family and that subsequent events are not falling off in a manner associated with aftershocks. Thus, these families do not represent a mainshock and

nearby events of aftershocks. This is another piece of evidence that they could be re-rupturing the same patch.

Figure 33: C.3 Time Since Mainshock versus Magnitude

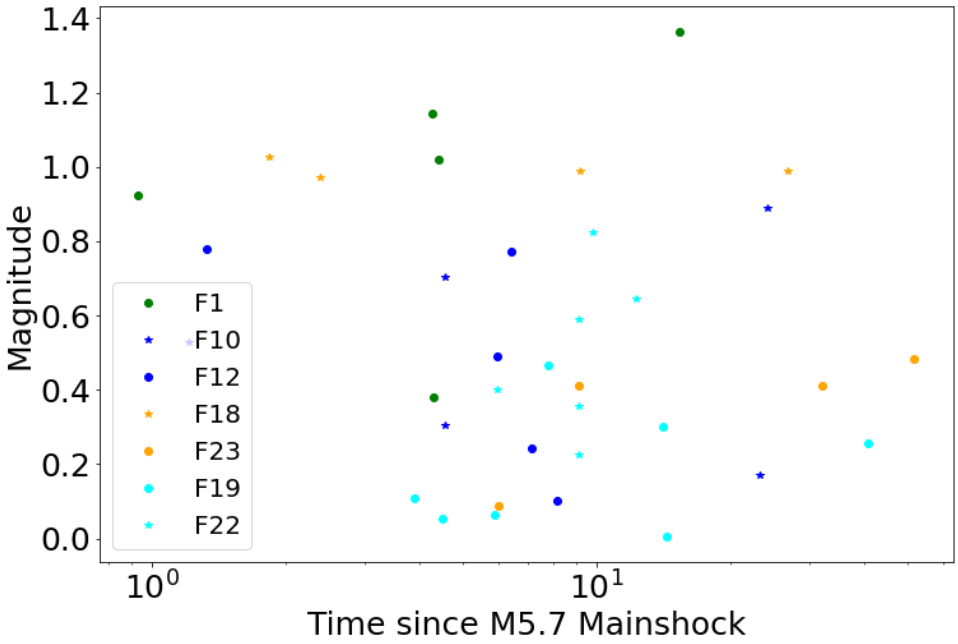

Figure S3: Time since the mainshock (days) versus magnitude for all families considered in this analysis. Magnitude is calculated from the moment as calculated from the p pulse.

Text S3. Spectral Estimate of Moment

Moment is measured from the p-pulse width in the manuscript. Moment is commonly measured from the long wavelength plateau of the spectra. We manually picked the p-pulse width, however some waveforms have poorly defined p-pulses (Figure 2-2), so we check these estimates against the spectral estimates. The p-wave spectra is calculated from a time window of 0.6*(s-p time) around the p-wave using

the python mtspec module, which calculates multitaper spectral estimates (Prieto et al., 2009; Krischer, 2016). The long wavelength plateau of the spectra (Ω_o) is the displacement spectral amplitude at 10 Hz (Figure S4). Moment calculated without a radiation term correction is averaged over all available stations and then a radiation term of 0.52 is applied, which is the same method as for moment measured from the p-pulse width.

The spectral estimates show the same moment-recurrence time behavior as the p-pulse widths (Figure S5). However, moment measured from the spectra extends from 10^8-10^{12} N-m, which is a larger range than the moment measured from the p-pulse (10^9-$2*10^{11}$ N-m). This is likely due to the larger window size of these measurements and from using a chosen spectral amplitude at 10 Hz instead of using a window to fit Ω_o. Nevertheless, the similarity in trends suggests that the manual picking of p-pulse widths is robust.

Figure 34: C.4 Displacement Spectra Example

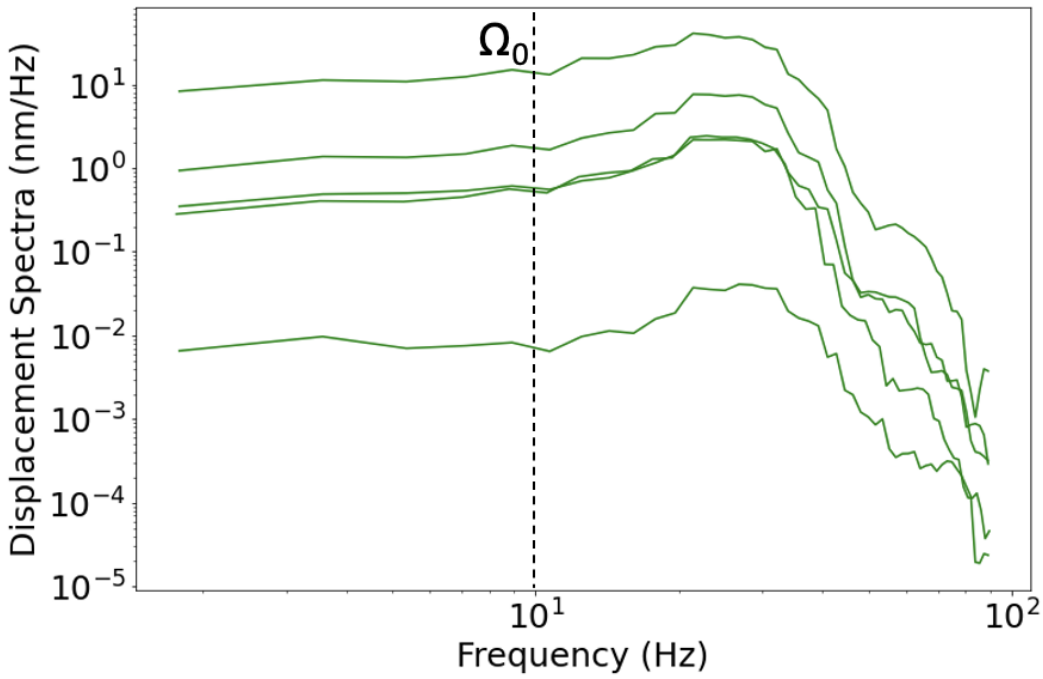

Figure S4. Displacement spectra of family 1 events at station LC01 showing how Ω_o is calculated.

Figure 35: C.5 Moment Calculated from Spectra vs Recurrence Time

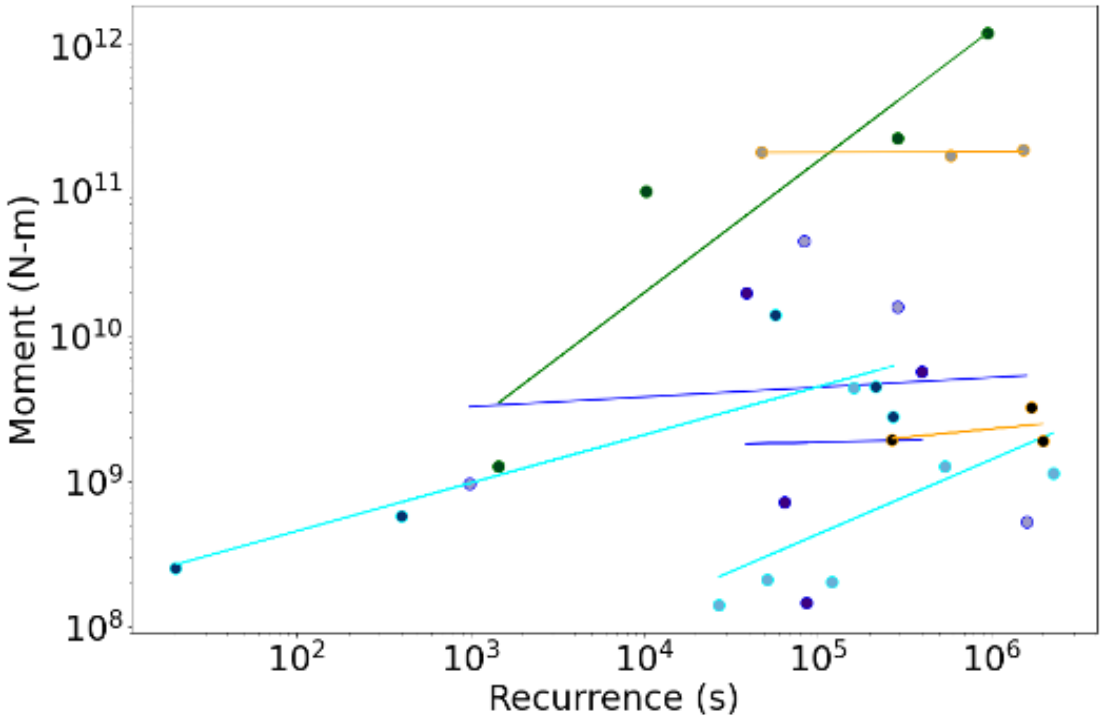

Figure S5. Spectral estimates of moment versus recurrence time.

References

Abercrombie, R. E. (2021). Resolution and uncertainties in estimates of earthquake stress drop and energy release. *Philosophical Transactions. Series A, Mathematical, Physical, and Engineering Sciences*, *379*(2196), 20200131. https://doi.org/10.1098/rsta.2020.0131

Abercrombie, R. E., Trugman, D. T., Shearer, P. M., Chen, X., Zhang, J., Pennington, C. N., et al. (2021). Does earthquake stress drop increase with depth in the crust? *Journal of Geophysical Research, [Solid Earth]*, *126*(10). https://doi.org/10.1029/2021jb022314

Adkins, J. F., Naviaux, J. D., Subhas, A. V., Dong, S., & Berelson, W. M. (2021). The Dissolution Rate of CaCO3 in the Ocean. *Annual Review of Marine Science*, *13*, 57–80. https://doi.org/10.1146/annurev-marine-041720-092514

Al-Shaieb, Z., & Lynch, M. (1993). Paleokarstic Features and Thermal Overprints Observed in Some of the Arbuckle Cores in Oklahoma. https://doi.org/10.2110/cor.93.18.0011

Baisch, S., & Harjes, H.-P. (2003). A model for fluid-injection-induced seismicity at the KTB, Germany. *Geophysical Journal International*, *152*(1), 160–170. https://doi.org/10.1046/j.1365-246X.2003.01837.x

Baisch, S., Ceranna, L., & Harjes, H.-P. (2008). Earthquake Cluster: What Can We Learn from Waveform Similarity?Earthquake Cluster: What Can We Learn from Waveform Similarity? *Bulletin of the Seismological Society of America*, *98*(6), 2806–2814. https://doi.org/10.1785/0120080018

Bedford, J. D., & Faulkner, D. R. (2021). The role of grain size and effective normal stress on localization and the frictional stability of simulated quartz gouge. *Geophysical Research Letters*, *48*(7). https://doi.org/10.1029/2020gl092023

Bedford, J. D., Faulkner, D. R., Allen, M. J., & Hirose, T. (2021). The stabilizing effect of high pore-fluid pressure along subduction megathrust faults: Evidence from friction experiments on accretionary sediments from the Nankai Trough. *Earth and Planetary Science Letters*, *574*, 117161. https://doi.org/10.1016/j.epsl.2021.117161

Bedford, J. D., Hirose, T., & Hamada, Y. (2023). Rapid fault healing after seismic slip. *Journal of Geophysical Research, [Solid Earth]*, *128*(6). https://doi.org/10.1029/2023jb026706

Beeler, N. M., Hickman, S. H., & Wong, T.-F. (2001a). Earthquake stress drop and laboratory-inferred interseismic strength recovery. *Journal of Geophysical Research*, *106*(B12), 30701–30713. https://doi.org/10.1029/2000jb900242

Beeler, N. M., Lockner, D. L., & Hickman, S. H. (2001b). A Simple Stick-Slip and Creep-Slip Model for Repeating Earthquakes and its Implication for Microearthquakes at Parkfield. *Bulletin of the Seismological Society of America*, *91*(6), 1797–1804. https://doi.org/10.1785/0120000096

Beeler, N. M., Tullis, T. E., & Weeks, J. D. (1994). The roles of time and displacement in the evolution effect in rock friction. *Geophysical Research Letters*, *21*(18), 1987–1990. https://doi.org/10.1029/94gl01599

Belzer, B. D., & French, M. E. (2022). Frictional constitutive behavior of chlorite at low shearing rates and hydrothermal conditions. *Tectonophysics*, *837*, 229435. https://doi.org/10.1016/j.tecto.2022.229435

Beyreuther, M., Barsch, R., Krischer, L., Megies, T., Behr, Y., & Wassermann, J. (2010). ObsPy: A Python Toolbox for Seismology. *Seismological Research Letters*, *81*(3), 530–533. https://doi.org/10.1785/gssrl.81.3.530

Bhattacharya, P., & Viesca, R. C. (2019). Fluid-induced aseismic fault slip outpaces pore-fluid migration. *Science*, *364*(6439), 464–468. https://doi.org/10.1126/science.aaw7354

Bhattacharya, P., Rubin, A. M., & Beeler, N. M. (2017). Does fault strengthening in laboratory rock friction experiments really depend primarily upon time and not slip? *Journal of Geophysical Research, [Solid Earth]*, *122*(8), 6389–6430. https://doi.org/10.1002/2017jb013936

Boatwright, J., & Cocco, M. (1996). Frictional constraints on crustal faulting. *Journal of Geophysical Research*, *101*(B6), 13895–13909. https://doi.org/10.1029/96jb00405

Booker, J. R. (1974). Time dependent strain following faulting of a porous medium. *Journal of Geophysical Research*, *79*(14), 2037–2044.

https://doi.org/10.1029/jb079i014p02037

Brune, J. N. (1970). Tectonic stress and the spectra of seismic shear waves from earthquakes. *Journal of Geophysical Research*, *75*(26), 4997–5009. https://doi.org/10.1029/jb075i026p04997

Byerlee, J. D. (1978). Friction of rocks. *Pure and Applied Geophysics*, *116*(4), 615–626. https://doi.org/10.1007/BF00876528

Cappa, F., Scuderi, M. M., Collettini, C., Guglielmi, Y., & Avouac, J.-P. (2019). Stabilization of fault slip by fluid injection in the laboratory and in situ. *Science Advances*, *5*(3), eaau4065. https://doi.org/10.1126/sciadv.aau4065

Cappa, F., Scuderi, M. M., Collettini, C., Guglielmi, Y., & Avouac, J.-P. (2019). Stabilization of fault slip by fluid injection in the laboratory and in situ. *Science Advances*, *5*(3), eaau4065. https://doi.org/10.1126/sciadv.aau4065

Carpenter, B. M., Collettini, C., Viti, C., & Cavallo, A. (2016a). The influence of normal stress and sliding velocity on the frictional behaviour of calcite at room temperature: insights from laboratory experiments and microstructural observations. *Geophysical Journal International*, *205*(1), 548–561. https://doi.org/10.1093/gji/ggw038

Carpenter, B. M., Ikari, M. J., & Marone, C. (2016b). Laboratory observations of time-dependent frictional strengthening and stress relaxation in natural and synthetic fault gouges. *Journal of Geophysical Research, [Solid Earth]*, *121*(2), 1183–1201. https://doi.org/10.1002/2015jb012136

Carpenter, B. M., Scuderi, M. M., Collettini, C., & Marone, C. (2014). Frictional heterogeneities on carbonate-bearing normal faults: Insights from the Monte Maggio Fault, Italy: Complex Friction on Carbonate Faults. *Journal of Geophysical Research, [Solid Earth]*, *119*(12), 9062–9076. https://doi.org/10.1002/2014jb011337

Cattania, C., & Segall, P. (2019). Crack models of repeating earthquakes predict observed moment-recurrence scaling. *Journal of Geophysical Research, [Solid Earth]*, *124*(1), 476–503. https://doi.org/10.1029/2018jb016056

Chaussard, E., R. Bürgmann, H. Fattahi, C. W. Johnson, R. Nadeau, T. Taira, and I. Johanson (2015), Interseismic coupling and refined earthquake potential on

the Hayward-Calaveras fault zone, J. Geophys. Res. Solid Earth, 120, 8570–8590, doi:10.1002/ 2015JB012230.

Chaves, E. J., Schwartz, S. Y., & Abercrombie, R. E. (2020). Repeating earthquakes record fault weakening and healing in areas of megathrust postseismic slip. *Science Advances*, *6*(32), eaaz9317. https://doi.org/10.1126/sciadv.aaz9317

Chen, J., Verberne, B. A., & Spiers, C. J. (2015). Effects of healing on the seismogenic potential of carbonate fault rocks: Experiments on samples from the Longmenshan Fault, Sichuan, China: FRICTIONAL HEALING OF CARBONATE. *Journal of Geophysical Research, [Solid Earth]*, *120*(8), 5479–5506. https://doi.org/10.1002/2015jb012051

Chen, K. H., Nadeau, R. M., & Rau, R.-J. (2007). Towards a universal rule on the recurrence interval scaling of repeating earthquakes? *Geophysical Research Letters*, *34*(16). https://doi.org/10.1029/2007gl030554

Chen, K. H., Nadeau, R. M., & Rau, R.-J. (2008). Characteristic repeating earthquakes in an arc-continent collision boundary zone: The Chihshang fault of eastern Taiwan. *Earth and Planetary Science Letters*, *276*(3), 262–272. https://doi.org/10.1016/j.epsl.2008.09.021

Cochran, E. S., Ross, Z. E., Harrington, R. M., Dougherty, S. L., & Rubinstein, J. L. (2018). Induced earthquake families reveal distinctive evolutionary patterns near disposal wells. *Journal of Geophysical Research, [Solid Earth]*, *123*(9), 8045–8055. https://doi.org/10.1029/2018jb016270

Cochran, E. S., Skoumal, R. J., McPhillips, D., Ross, Z. E., & Keranen, K. M. (2020). Activation of optimally and unfavourably oriented faults in a uniform local stress field during the 2011 Prague, Oklahoma, sequence. *Geophysical Journal International*, *222*(1), 153–168. https://doi.org/10.1093/gji/ggaa153

Collettini, C., & Holdsworth, R. E. (2004). Fault zone weakening and character of slip along low-angle normal faults: insights from the Zuccale fault, Elba, Italy. *Journal of the Geological Society*, *161*(6), 1039–1051. https://doi.org/10.1144/0016-764903-179

Crotwell, P. H., Owens, T. J., & Ritsema, J. (1999). The TauP Toolkit: Flexible Seismic Travel-time and Ray-path Utilities. *Seismological Research Letters*, *70*(2), 154–160. https://doi.org/10.1785/gssrl.70.2.154

den Ende, M. P. A., Niemeijer, A. R., & Spiers, C. J. (2019). Influence of grain boundary structural evolution on pressure solution creep rates. *Journal of Geophysical Research, [Solid Earth]*, *124*(10), 10210–10230. https://doi.org/10.1029/2019jb017500

Derby, J. R., Hinch, H. H., & Repetski, J. R. (1991). Lithology, stratigraphy, and age of the Arbuckle Group in the Amoco Shads No. 4, a continuous core from grassroots into basement, Rogers County, Oklahoma. In *Arbuckle Group Core Workshop and Field Trip: Oklahoma Geological Survey, Special Publication* (Vol. 91, pp. 69–82).

Di Toro, G., Han, R., Hirose, T., De Paola, N., Nielsen, S., Mizoguchi, K., et al. (2011). Fault lubrication during earthquakes. *Nature*, *471*(7339), 494–498. https://doi.org/10.1038/nature09838

Di Toro, G., Mittempergher, S., Ferri, F., Mitchell, T. M., & Pennacchioni, G. (2012). The contribution of structural geology, experimental rock deformation and numerical modelling to an improved understanding of the seismic cycle: Preface to the Special Volume "Physico-chemical processes in seismic faults." *Journal of Structural Geology*, *38*, 3–10. https://doi.org/10.1016/j.jsg.2012.01.025

Dieterich, J. H. (1972). Time-dependent friction in rocks. *Journal of Geophysical Research*, *77*(20), 3690–3697. https://doi.org/10.1029/jb077i020p03690

Dieterich, J. H. (1979). Modeling of rock friction: 1. Experimental results and constitutive equations. *Journal of Geophysical Research*, *84*(B5), 2161. https://doi.org/10.1029/jb084ib05p02161

Dieterich, J. H. (1992). Earthquake nucleation on faults with rate-and state-dependent strength. *Tectonophysics*, *211*(1), 115–134. https://doi.org/10.1016/0040-1951(92)90055-B

Dieterich, J. H. (1994). A constitutive law for rate of earthquake production and its application to earthquake clustering. *Journal of Geophysical Research*, *99*(B2), 2601–2618. https://doi.org/10.1029/93jb02581

Ekström, G., Nettles, M., & Dziewoński, A. M. (2012). The global CMT project 2004–2010: Centroid-moment tensors for 13,017 earthquakes. *Physics of the Earth and Planetary Interiors*, *200–201*, 1–9. https://doi.org/10.1016/j.pepi.2012.04.002

Ellsworth, W. L. (2013). Injection-induced earthquakes. *Science*, *341*(6142), 1225942. https://doi.org/10.1126/science.1225942

Eshelby, J. D. (1957). The determination of the elastic field of an ellipsoidal inclusion, and related problems. *Proceedings of the Royal Society of London. Series A, Mathematical and Physical Sciences*, *241*(1226), 376–396. https://doi.org/10.1098/rspa.1957.0133

Eyre, T. S., Eaton, D. W., Garagash, D. I., Zecevic, M., Venieri, M., Weir, R., & Lawton, D. C. (2019). The role of aseismic slip in hydraulic fracturing-induced seismicity. *Science Advances*, *5*(8), eaav7172. https://doi.org/10.1126/sciadv.aav7172

Faith, J. R., Blome, C. D., Pantea, M. P., Puckette, J. O., Halihan, T., Osborn, N., et al. (2010). Three-dimensional geologic model of the Arbuckle-Simpson aquifer, south-central Oklahoma. *Open-File Report*. https://doi.org/10.3133/ofr20101123

Faulkner, D. R., Sanchez-Roa, C., Boulton, C., & den Hartog, S. A. M. (2018). Pore fluid pressure development in compacting fault gouge in theory, experiments, and nature. *Journal of Geophysical Research, [Solid Earth]*, *123*(1), 226–241. https://doi.org/10.1002/2017jb015130

Felzer, K. R., & Brodsky, E. E. (2006). Decay of aftershock density with distance indicates triggering by dynamic stress. *Nature*, *441*(7094), 735–738. https://doi.org/10.1038/nature04799

Frankel, A., & Kanamori, H. (1983). Determination of rupture duration and stress drop for earthquakes in southern California. *Bulletin of the Seismological Society of America*, *73*(6A), 1527–1551. Retrieved from https://authors.library.caltech.edu/49193/1/1527.full.pdf

French, M. E., & Morgan, J. K. (2020). Pore fluid pressures and strength contrasts maintain frontal fault activity, northern hikurangi margin, New Zealand. *Geophysical Research Letters*, *47*(21). https://doi.org/10.1029/2020gl089209

French, M. E., Zhu, W., Xiao, X., Evans, B., & Prior, D. J. (2022). Thermally enhanced water weakening of the solnhofen limestone. *Journal of Geophysical Research, [Solid Earth]*, *127*(3). https://doi.org/10.1029/2021jb022742

Frohlich, C. (2012). Two-year survey comparing earthquake activity and injection-well locations in the Barnett Shale, Texas. *Proceedings of the National Academy of Sciences of the United States of America*, *109*(35), 13934–13938. https://doi.org/10.1073/pnas.1207728109

Fu, B., Diao, Y., & Espinosa-Marzal, R. M. (2021). Nanoscale insight into the relation between pressure solution of calcite and interfacial friction. *Journal of Colloid and Interface Science*, *601*, 254–264. https://doi.org/10.1016/j.jcis.2021.04.145

Geller, R. J., & Mueller, C. S. (1980). Four similar earthquakes in central California. *Geophysical Research Letters*, *7*(10), 821–824. https://doi.org/10.1029/gl007i010p00821

Goebel, T. H. W., & Brodsky, E. E. (2018). The spatial footprint of injection wells in a global compilation of induced earthquake sequences. *Science*, *361*(6405), 899–904. https://doi.org/10.1126/science.aat5449

Goebel, T. H. W., Weingarten, M., Chen, X., Haffener, J., & Brodsky, E. E. (2017). The 2016 Mw5.1 Fairview, Oklahoma earthquakes: Evidence for long-range poroelastic triggering at >40 km from fluid disposal wells. *Earth and Planetary Science Letters*, *472*, 50–61. https://doi.org/10.1016/j.epsl.2017.05.011

Gu, J.-C., Rice, J. R., Ruina, A. L., & Tse, S. T. (1984). Slip motion and stability of a single degree of freedom elastic system with rate and state dependent friction. *Journal of the Mechanics and Physics of Solids*, *32*(3), 167–196. https://doi.org/10.1016/0022-5096(84)90007-3

Guglielmi, Y., Cappa, F., Avouac, J.-P., Henry, P., & Elsworth, D. (2015). INDUCED SEISMICITY. Seismicity triggered by fluid injection-induced aseismic slip. *Science*, *348*(6240), 1224–1226. https://doi.org/10.1126/science.aab0476

Hagberg, A. A., Schult, D. A., & Swart, P. J. (2008). Exploring Network Structure, Dynamics, and Function using NetworkX. In G. Varoquaux, T. Vaught, & J. Millman (Eds.), *Proceedings of the 7th Python in Science Conference* (pp. 11–15). Pasadena, CA USA.

Hanks, T. C., & Kanamori, H. (1979). A moment magnitude scale. *Journal of Geophysical Research*, *84*(B5), 2348. https://doi.org/10.1029/jb084ib05p02348

Harrington, R. M., & Brodsky, E. E. (2009). Source duration scales with magnitude differently for earthquakes on the San Andreas fault and on secondary faults in Parkfield, California. *Bulletin of the Seismological Society of America*, *99*(4), 2323–2334. https://doi.org/10.1785/0120080216

He, L., Wu, Q., Chen, X., Sun, X., Guo, Z., & Chen, Y. J. (2021). Detailed 3D seismic velocity structure of the Prague, Oklahoma fault zone and the implications for induced seismicity. *Geophysical Research Letters*, *48*(24). https://doi.org/10.1029/2021gl096137

Healy, J. H., Rubey, W. W., Griggs, D. T., & Raleigh, C. B. (1968). The Denver EarthquakeS. *Science*, *161*(3848), 1301–1310. https://doi.org/10.1126/science.161.3848.1301

Heinicke, J., Fischer, T., Gaupp, R., Götze, J., Koch, U., Konietzky, H., & Stanek, K.-P. (2009). Hydrothermal alteration as a trigger mechanism for earthquake swarms: the Vogtland/NW Bohemia region as a case study. *Geophysical Journal International*, *178*(1), 1–13. https://doi.org/10.1111/j.1365-246X.2009.04138.x

Helmstetter, A., & Shaw, B. E. (2009). Afterslip and aftershocks in the rate-and-state friction law: AFTERSHOCKS AND RATE-AND-STATE FRICTION. *Journal of Geophysical Research*, *114*(B1). https://doi.org/10.1029/2007jb005077

Hirakawa, E., & Ma, S. (2016). Dynamic fault weakening and strengthening by gouge compaction and dilatancy in a fluid-saturated fault zone. *Journal of Geophysical Research, [Solid Earth]*, *121*(8), 5988–6008. https://doi.org/10.1002/2015jb012509

Hirao, B., Savage, H., & Brodsky, E. E. (2021). Communication between the northern and southern central San Andreas fault via dynamically triggered creep. *Geophysical Research Letters*, *48*(13). https://doi.org/10.1029/2021gl092530

Hornbach, M. J., Jones, M., Scales, M., DeShon, H. R., Magnani, M. B., Frohlich, C., Stump, B., Hayward, C., & Layton, M. (2016). Ellenburger wastewater injection

and seismicity in North Texas. *Physics of the Earth and Planetary Interiors*, *261*, 54–68. https://doi.org/10.1016/j.pepi.2016.06.012

Igarashi, T., Matsuzawa, T., & Hasegawa, A. (2003). Repeating earthquakes and interplate aseismic slip in the northeastern Japan subduction zone: REPEATING EARTHQUAKES AND ASEISMIC SLIP. *Journal of Geophysical Research*, *108*(B5). https://doi.org/10.1029/2002jb001920

Ikari, M. J., Carpenter, B. M., Scuderi, M. M., Collettini, C., & Kopf, A. J. (2020). Frictional strengthening explored during non-steady state shearing: Implications for fault stability and slip event recurrence time. *Journal of Geophysical Research, [Solid Earth]*, *125*(10). https://doi.org/10.1029/2020jb020015

Im, K., Elsworth, D., Marone, C., & Leeman, J. (2017). The impact of frictional healing on stick-slip recurrence interval and stress drop: Implications for earthquake scaling. *Journal of Geophysical Research, [Solid Earth]*, *122*(12), 10,102–110,117. https://doi.org/10.1002/2017jb014476

Jeppson, T., Lockner, D., Beeler, N., & Hickman, S. (2023). Strength recovery in Quartzite is controlled by changes in friction in experiments at hydrothermal conditions up to 200°C. *Journal of Geophysical Research, [Solid Earth]*, *128*(5). https://doi.org/10.1029/2022jb025663

Kanamori, H., & Allen, C. R. (1986). Earthquake repeat time and average stress drop. In *Earthquake Source Mechanics* (pp. 227–235). Washington, D. C.: American Geophysical Union. https://doi.org/10.1029/gm037p0227

Kanamori, H., & Brodsky, E. E. (2004). The physics of earthquakes. *Reports on Progress in Physics*, *67*(8), 1429. https://doi.org/10.1088/0034-4885/67/8/R03

Kato, A., Fukuda, J., Nakagawa, S., & Obara, K. (2016). Foreshock migration preceding the 2016 Mw 7.0 Kumamoto earthquake, Japan: FORESHOCK MIGRATION. *Geophysical Research Letters*, *43*(17), 8945–8953. https://doi.org/10.1002/2016gl070079

Kato, A., Obara, K., Igarashi, T., Tsuruoka, H., Nakagawa, S., & Hirata, N. (2012). Propagation of slow slip leading up to the 2011 M(w) 9.0 Tohoku-Oki earthquake. *Science*, *335*(6069), 705–708. https://doi.org/10.1126/science.1215141

Kato, N. (2007). Expansion of aftershock areas caused by propagating post-seismic sliding. *Geophysical Journal International*, *168*(2), 797–808. https://doi.org/10.1111/j.1365-246X.2006.03255.x

Kemna, K. B., Peña Castro, A. F., Harrington, R. M., & Cochran, E. S. (2020). Using a large-*n*seismic array to explore the robustness of spectral estimations. *Geophysical Research Letters*, *47*(21). https://doi.org/10.1029/2020gl089342

Keranen, K. M., & Weingarten, M. (2018). Induced Seismicity. *Annual Review of Earth and Planetary Sciences*, *46*(1), 149–174. https://doi.org/10.1146/annurev-earth-082517-010054

Keranen, K. M., Savage, H. M., Abers, G. A., & Cochran, E. S. (2013). Potentially induced earthquakes in Oklahoma, USA: Links between wastewater injection and the 2011 Mw 5.7 earthquake sequence. *Geology*, *41*(6), 699–702. https://doi.org/10.1130/G34045.1

Keranen, K. M., Weingarten, M., Abers, G. A., Bekins, B. A., & Ge, S. (2014). Induced earthquakes. Sharp increase in central Oklahoma seismicity since 2008 induced by massive wastewater injection. *Science*, *345*(6195), 448–451. https://doi.org/10.1126/science.1255802

Kolawole, F., Johnston, C. S., Morgan, C. B., Chang, J. C., Marfurt, K. J., Lockner, D. A., Reches, Z., & Carpenter, B. M. (2019). The susceptibility of Oklahoma's basement to seismic reactivation. *Nature Geoscience*, *12*(10), 839–844. https://doi.org/10.1038/s41561-019-0440-5

Lay, T., & Kanamori, H. (Eds.). (1981). An asperity model of large earthquake sequences. In *Earthquake Prediction* (pp. 579–592). American Geophysical Union. https://doi.org/10.1029/ME004p0579

Lengliné, O., Lamourette, L., Vivin, L., Cuenot, N., & Schmittbuhl, J. (2014). Fluid-induced earthquakes with variable stress drop. *Journal of Geophysical Research, [Solid Earth]*, *119*(12), 8900–8913. https://doi.org/10.1002/2014jb011282

Lin, Y. Y., & Lapusta, N. (2018). Microseismicity simulated on asperity-like fault patches: On scaling of seismic moment with duration and seismological estimates of stress drops. *Geophysical Research Letters*. https://doi.org/10.1029/2018GL078650

Lisabeth, H. P., & Zhu, W. (2015). Effect of temperature and pore fluid on the strength of porous limestone. *Journal of Geophysical Research, [Solid Earth]*. https://doi.org/10.1002/2015JB012152

Magnani, M. B., Blanpied, M. L., DeShon, H. R., & Hornbach, M. J. (2017). Discriminating between natural versus induced seismicity from long-term deformation history of intraplate faults. *Science Advances*, *3*(11), e1701593. https://doi.org/10.1126/sciadv.1701593

Marone, C. (1998). The effect of loading rate on static friction and the rate of fault healing during the earthquake cycle. *Nature*, *391*(6662), 69–72. https://doi.org/10.1038/34157

Marone, C., & Kilgore, B. (1993). Scaling of the critical slip distance for seismic faulting with shear strain in fault zones. *Nature*, *362*(6421), 618–621. https://doi.org/10.1038/362618a0

Marone, C., & Saffer, D. M. (2015). 4.05 - The Mechanics of Frictional Healing and Slip Instability During the Seismic Cycle. In G. Schubert (Ed.), *Treatise on Geophysics (Second Edition)* (pp. 111–138). Oxford: Elsevier. https://doi.org/10.1016/B978-0-444-53802-4.00092-0

Marone, C., & Scholz, C. H. (1988). The depth of seismic faulting and the upper transition from stable to unstable slip regimes. *Geophysical Research Letters*, *15*(6), 621–624. https://doi.org/10.1029/gl015i006p00621

Marone, C., Scholtz, C. H., & Bilham, R. (1991). On the mechanics of earthquake afterslip. *Journal of Geophysical Research*. https://doi.org/10.1029/91jb00275

Marsan, D. (2006). Can coseismic stress variability suppress seismicity shadows? Insights from a rate-and-state friction model. *Journal of Geophysical Research*, *111*(B6). https://doi.org/10.1029/2005jb004060

Marty, S., Passelègue, F. X., Aubry, J., Bhat, H. S., Schubnel, A., & Madariaga, R. (2019). Origin of high-frequency radiation during laboratory earthquakes. *Geophysical Research Letters*, *46*(7), 3755–3763. https://doi.org/10.1029/2018gl080519

Nadeau, R. M., & Johnson, L. R. (1998). Seismological Studies at Parkfield VI: Moment Release Rates and Estimates of Source Parameters for Small

Repeating Earthquakes. *Bulletin of the Seismological Society of America*, *88*(3), 790–814.

Nagata, K., Nakatani, M., & Yoshida, S. (2012). A revised rate- and state-dependent friction law obtained by constraining constitutive and evolution laws separately with laboratory data. *Journal of Geophysical Research, 117*(B2). https://doi.org/10.1029/2011jb008818

Nakatani, M., & Scholz, C. H. (2006). Intrinsic and apparent short-time limits for fault healing: Theory, observations, and implications for velocity-dependent friction. *Journal of Geophysical Research, 111*(B12). https://doi.org/10.1029/2005jb004096

Norbeck, J. H., & Horne, R. N. (2016). Evidence for a transient hydromechanical and frictional faulting response during the 2011Mw 5.6 Prague, Oklahoma earthquake sequence: FAULTING RESPONSE AT PRAGUE. *Journal of Geophysical Research, [Solid Earth]*, *121*(12), 8688–8705. https://doi.org/10.1002/2016jb013148

Nur, A., & Booker, J. R. (1972). Aftershocks Caused by Pore Fluid Flow? *Science*, *175*(4042), 885–887. Retrieved from https://www.jstor.org/stable/pdf/1733666.pdf

Okamoto, K. K., Savage, H. M., Cochran, E. S., & Keranen, K. M. (2022). Stress heterogeneity as a driver of aseismic slip during the 2011 Prague, Oklahoma aftershock sequence. *Journal of Geophysical Research, [Solid Earth], 127*(8). https://doi.org/10.1029/2022jb024431

Pennington, C. N., Chen, X., Abercrombie, R. E., & Wu, Q. (2021). Cross validation of stress drop estimates and interpretations for the 2011 Prague, OK, earthquake sequence using multiple methods. *Journal of Geophysical Research, [Solid Earth], 126*(3). https://doi.org/10.1029/2020jb020888

Perfettini, H., & Avouac, J.-P. (2004). Postseismic relaxation driven by brittle creep: A possible mechanism to reconcile geodetic measurements and the decay rate of aftershocks, application to the Chi-Chi earthquake, Taiwan. *Journal of Geophysical Research*, *109*(B2). https://doi.org/10.1029/2003jb002488

Perfettini, H., & Avouac, J.-P. (2007). Modeling afterslip and aftershocks following the 1992 Landers earthquake. *Journal of Geophysical Research*, *112*(B7).

https://doi.org/10.1029/2006jb004399

Rabinowicz, E. (1956). Stick and Slip. *Scientific American*, *194*(5), 109–119. http://www.jstor.org/stable/26122743

Raj, R. (1982). Creep in Polycrystalline Aggregates by Matter Transport Through a Liquid Phase. *Journal of Geophysical Research*, *87*(B6), 4731–4739. https://doi.org/10.1029/JB087iB06p04731

Raleigh, C. B., Healy, J. H., & Bredehoeft, J. D. (1976). An experiment in earthquake control at rangely, colorado. *Science*, *191*(4233), 1230–1237. https://doi.org/10.1126/science.191.4233.1230

Ranjith, K., & Rice, J. R. (1999). Stability of quasi-static slip in a single degree of freedom elastic system with rate and state dependent friction. *Journal of the Mechanics and Physics of Solids*, *47*(6), 1207–1218. https://doi.org/10.1016/S0022-5096(98)00113-6

Rathbun, A. P., & Marone, C. (2013). Symmetry and the critical slip distance in rate and state friction laws. *Journal of Geophysical Research, [Solid Earth]*, *118*(7), 3728–3741. https://doi.org/10.1002/jgrb.50224

Renard, F., Beauprêtre, S., Voisin, C., Zigone, D., Candela, T., Dysthe, D. K., & Gratier, J.-P. (2012). Strength evolution of a reactive frictional interface is controlled by the dynamics of contacts and chemical effects. *Earth and Planetary Science Letters*, *341-344*, 20–34. https://doi.org/10.1016/j.epsl.2012.04.048

Reynolds, O. (1885). LVII. On the dilatancy of media composed of rigid particles in contact. With experimental illustrations. *The London, Edinburgh, and Dublin Philosophical Magazine and Journal of Science*, *20*(127), 469–481. https://doi.org/10.1080/14786448508627791

Ross, Z. E., Cochran, E. S., Trugman, D. T., & Smith, J. D. (2020). 3D fault architecture controls the dynamism of earthquake swarms. *Science*, *368*(6497), 1357–1361. https://doi.org/10.1126/science.abb0779

Rubinstein, J. L., Ellsworth, W. L., Beeler, N. M., Kilgore, B. D., Lockner, D. A., & Savage, H. M. (2012b). Fixed recurrence and slip models better predict earthquake behavior than the time- and slip-predictable models: 2. Laboratory

earthquakes. *Journal of Geophysical Research, [Solid Earth]*, *117*(B2). https://doi.org/10.1029/2011JB008723

Rubinstein, J. L., Ellsworth, W. L., Chen, K. H., & Uchida, N. (2012a). Fixed recurrence and slip models better predict earthquake behavior than the time- and slip-predictable models: 1. Repeating earthquakes. *Journal of Geophysical Research*, *117*(B2). https://doi.org/10.1029/2011jb008724

Ruina, A. (1983). Slip instability and state variable friction laws. *Journal of Geophysical Research*, *88*(B12), 10359–10370. https://doi.org/10.1029/jb088ib12p10359

Ryan, K. L., Rivière, J., & Marone, C. (2018). The role of shear stress in fault healing and frictional aging. *Journal of Geophysical Research, [Solid Earth]*, *123*(12), 10,479–10,495. https://doi.org/10.1029/2018jb016296

Samuelson, J., & Spiers, C. J. (2012). Fault friction and slip stability not affected by Co2 storage: Evidence from short-term laboratory experiments on North Sea reservoir sandstones and caprocks. *International Journal of Greenhouse Gas Control*, *11*, S78–S90. https://doi.org/10.1016/j.ijggc.2012.09.018

Savage, H. M., & Brodsky, E. E. (2011). Collateral damage: Evolution with displacement of fracture distribution and secondary fault strands in fault damage zones. *Journal of Geophysical Research*, *116*(B3). https://doi.org/10.1029/2010jb007665

Savage, H. M., & Marone, C. (2008). Potential for earthquake triggering from transient deformations. *Journal of Geophysical Research*, *113*(B5). https://doi.org/10.1029/2007jb005277

Savage, H. M., Keranen, K. M., P. Schaff, D., & Dieck, C. (2017). Possible precursory signals in damage zone foreshocks: Damage Zone Earthquakes. *Geophysical Research Letters*, *44*(11), 5411–5417. https://doi.org/10.1002/2017gl073226

Savage, H. M., Skarbek, R. M., Polissar, P. J., Mccarthy, C., & Rowe, C. D. (2019). How Coseismic Temperature Rise Affects Postseismic Healing (Vol. 2019, p. T22B–08). Retrieved from https://ui.adsabs.harvard.edu/abs/2019AGUFM.T22B..08S

Scholz, C. H. (1988). The critical slip distance for seismic faulting. *Nature*, *336*(6201), 761–763. https://doi.org/10.1038/336761a0

Scholz, C. H. (1998). Earthquakes and friction laws. *Nature*, *391*(6662), 37–42. https://doi.org/10.1038/34097

Schultz, R., Corlett, H., Haug, K., Kocon, K., MacCormack, K., Stern, V., & Shipman, T. (2016). Linking fossil reefs with earthquakes: Geologic insight to where induced seismicity occurs in Alberta. *Geophysical Research Letters, 43*(6), 2534–2542. https://doi.org/10.1002/2015GL067514

Schwartz, S. Y., & Rokosky, J. M. (2007). Slow slip events and seismic tremor at circum-Pacific subduction zones: SLOW SLIP AND SEISMIC TREMOR. *Reviews of Geophysics* , *45*(3). https://doi.org/10.1029/2006rg000208

Scuderi, M. M., & Collettini, C. (2016). The role of fluid pressure in induced vs. triggered seismicity: insights from rock deformation experiments on carbonates. *Scientific Reports, 6,* 24852. https://doi.org/10.1038/srep24852

Shaddox, H. R., & Schwartz, S. Y. (2019). Subducted seamount diverts shallow slow slip to the forearc of the northern Hikurangi subduction zone, New Zealand. *Geology*, *47*(5), 415–418. https://doi.org/10.1130/g45810.1

Shaddox, H. R., Schwartz, S. Y., & Bartlow, N. M. (2021). Afterslip and spontaneous aseismic slip on the Anza segment of the San Jacinto fault zone, southern California. *Journal of Geophysical Research, [Solid Earth]*, *126*(6). https://doi.org/10.1029/2020jb020460

Shearer, P. M. (2009). *Introduction to Seismology*. Cambridge University Press. https://doi.org/10.1017/CBO9780511841552

Shearer, P. M., Prieto, G. A., & Hauksson, E. (2006). Comprehensive analysis of earthquake source spectra in southern California. *Journal of Geophysical Research, 111*(B6). https://doi.org/10.1029/2005jb003979

Shimazaki, K., & Nakata, T. (1980). Time-predictable recurrence model for large earthquakes. *Geophysical Research Letters, 7*(4), 279–282. https://doi.org/10.1029/gl007i004p00279

Shreedharan, S., Ikari, M., Wood, C., Saffer, D., Wallace, L., & Marone, C. (2022). Frictional and lithological controls on shallow slow slip at the northern hikurangi

margin. *Geochemistry, Geophysics, Geosystems*, *23*(2). https://doi.org/10.1029/2021gc010107

Skarbek, R. M., & Savage, H. M. (2019). RSFit3000: A MATLAB GUI-based program for determining rate and state frictional parameters from experimental data. *Geosphere*, *15*(5), 1665–1676. https://doi.org/10.1130/GES02122.1

Skoumal, R. J., Ole Kaven, J., & Walter, J. I. (2019). Characterizing Seismogenic Fault Structures in Oklahoma Using a Relocated Template-Matched Catalog. *Seismological Research Letters*, *90*(4), 1535–1543. https://doi.org/10.1785/0220190045

Sleep, N. H., & Blanpied, M. L. (1992). Creep, compaction and the weak rheology of major faults. *Nature*, *359*(6397), 687–692. https://doi.org/10.1038/359687a0

Sumy, D. F., Cochran, E. S., Keranen, K. M., Wei, M., & Abers, G. A. (2014). Observations of static Coulomb stress triggering of the November 2011 M 5.7 Oklahoma earthquake sequence. *Journal of Geophysical Research, [Solid Earth]*, *119*(3), 1904–1923. https://doi.org/10.1002/2013jb010612

Sumy, D. F., Neighbors, C. J., Cochran, E. S., & Keranen, K. M. (2017). Low stress drops observed for aftershocks of the 2011Mw5.7 Prague, Oklahoma, earthquake: Low Stress Drops for Prague Aftershocks. *Journal of Geophysical Research, [Solid Earth]*, *122*(5), 3813–3834. https://doi.org/10.1002/2016jb013153

Taira, T., R. Bürgmann, R. M. Nadeau, andD. S. Dreger (2014), Variability of faultslip behavior along the San AndreasFault in the San Juan Bautista Region,J. Geophys. Res. Solid Earth,119,8827–8844, doi:10.1002/2014JB011427

Takashimizu, Y., & Iiyoshi, M. (2016). New parameter of roundness R: circularity corrected by aspect ratio. *Progress in Earth and Planetary Science*, *3*(1), 1–16. https://doi.org/10.1186/s40645-015-0078-x

Terzaghi, K. (1936). The shearing resistance of saturated soils and the angle between the planes of shear. *First International Conference on Soil Mechanics*, *1936*, *1*, 54–59. Retrieved from https://cir.nii.ac.jp/crid/1571698601182271232

Tesei, T., Collettini, C., Barchi, M. R., Carpenter, B. M., & Di Stefano, G. (2014). Heterogeneous strength and fault zone complexity of carbonate-bearing thrusts with possible implications for seismicity. *Earth and Planetary Science Letters*, *408*, 307–318. https://doi.org/10.1016/j.epsl.2014.10.021

Trugman, D. T. (2020). Stress-Drop and Source Scaling of the 2019 Ridgecrest, California, Earthquake Sequence. *Bulletin of the Seismological Society of America*, *110*(4), 1859–1871. https://doi.org/10.1785/0120200009

Trugman, D. T., & Shearer, P. M. (2017). GrowClust: A Hierarchical Clustering Algorithm for Relative Earthquake Relocation, with Application to the Spanish Springs and Sheldon, Nevada, Earthquake Sequences. *Seismological Research Letters*, *88*(2A), 379–391. https://doi.org/10.1785/0220160188

Turcotte, D. L., Moores, E. M., & Rundle, J. B. (2014). Super fracking. *Physics Today*, *67*(8), 34–39. https://doi.org/10.1063/pt.3.2480

Uchida, N. (2019). Detection of repeating earthquakes and their application in characterizing slow fault slip. *Progress in Earth and Planetary Science*, *6*(1), 40.

Uchida, N., & Bürgmann, R. (2019). Repeating Earthquakes. *Annual Review of Earth and Planetary Sciences*, *47*(1). https://doi.org/10.1146/annurev-earth-053018-060119

van der Elst, N. J., Savage, H. M., Keranen, K. M., & Abers, G. A. (2013). Enhanced remote earthquake triggering at fluid-injection sites in the midwestern United States. *Science*, *341*(6142), 164–167. https://doi.org/10.1126/science.1238948

van Noort, R., & Spiers, C. J. (2008). Kinetic effects of microscale plasticity at grain boundaries during pressure solution. *JOURNAL OF GEOPHYSICAL RESEARCH*, *114*(B03206). https://doi.org/10.1029/2008JB005634

Vavryčuk, V., & Hrubcová, P. (2017). Seismological evidence of fault weakening due to erosion by fluids from observations of intraplate earthquake swarms. *Journal of Geophysical Research, [Solid Earth]*, *122*(5), 3701–3718. https://doi.org/10.1002/2017jb013958

Walsh, R. F., & Zoback, M. D. (2016). Probabilistic assessment of potential fault slip related to injection-induced earthquakes: Application to north-central

Oklahoma, USA. *Geology*, *44*(12), 991–994. https://doi.org/10.1130/G38275.1

Way, H. S. K. (1983, July). *Structural Study of the Hunton Lime of the Wilzetta Field, T12-13N, R5E, Lincoln County, Oklahoma, Pertaining to the Exploration for Hydrocarbons*. (J. D. Naff, Ed.). Retrieved from https://shareok.org/bitstream/handle/11244/16448/Thesis-1983-W357s.pdf?sequence=1&isAllowed=y

Wei, S., Avouac, J.-P., Hudnut, K. W., Donnellan, A., Parker, J. W., Graves, R. W., et al. (2015). The 2012 Brawley swarm triggered by injection-induced aseismic slip. *Earth and Planetary Science Letters*, *422*, 115–125. https://doi.org/10.1016/j.epsl.2015.03.054

Weingarten, M., Ge, S., Godt, J. W., Bekins, B. A., & Rubinstein, J. L. (2015). High-rate injection is associated with the increase in U.S. mid-continent seismicity. *Science*, *348*(6241), 1336–1340. https://doi.org/10.1126/science.aab1345

Wynants-Morel, N., Cappa, F., De Barros, L., & Ampuero, J.-P. (2020). Stress perturbation from aseismic slip drives the seismic front during fluid injection in a permeable fault. *Journal of Geophysical Research, [Solid Earth]*, *125*(7). https://doi.org/10.1029/2019jb019179

Xing, T., Zhu, W., French, M., & Belzer, B. (2019). Stabilizing effect of high pore fluid pressure on slip behaviors of gouge-bearing faults. *Journal of Geophysical Research, [Solid Earth]*, *124*(9), 9526–9545. https://doi.org/10.1029/2019jb018002

Yokoyama, T., & Nishiyama, N. (2020). Dissolution of Minerals Driven by the Wetting Film in Rock Pores: Comparison of Silicates and Carbonates. *ACS Earth and Space Chemistry*, *4*(11), 1920–1930. https://doi.org/10.1021/acsearthspacechem.0c00100

Zahradník, J., & Gallovič, F. (2010). Toward understanding slip inversion uncertainty and artifacts. *Journal of Geophysical Research*, *115*(B9). https://doi.org/10.1029/2010jb007414

Zhang, X., & Spiers, C. J. (2005). Compaction of granular calcite by pressure solution at room temperature and effects of pore fluid chemistry. *International Journal of*

Rock Mechanics and Mining Sciences, *42*(7), 950–960. https://doi.org/10.1016/j.ijrmms.2005.05.017